STUDIES ON THE STRESS FLUCTUATIONS IN SHEARED STOKESIAN SUSPENSIONS USING CHAOS THEORY AND NONLINEAR DYNAMICS

Thesis submitted to
THE COCHIN UNIVERSITY OF SCIENCE AND TECHNOLOGY
in partial fulfillment of the requirements
for the degree of
DOCTOR OF PHILOSOPHY

J. DASAN

under the guidance of
DR. T. R. RAMAMOHAN

REGIONAL RESEARCH LABORATORY (CSIR)
THIRUVANANTHAPURAM
KERALA INDIA

November 2005

Council of Scientific & Industrial Research
क्षेत्रीय अनुसंधान प्रयोगशाला
REGIONAL RESEARCH LABORATORY
इन्डस्ट्रीयल इस्टेट - डाक घर, तिरुवनन्तपुरम - 695 019, भारत
Industrial Estate.P.O., Thiruvananthapuram - 695 019, INDIA

Dr.T.R. Ramamohan
Scientist F, CSIR

CERTIFICATE

This is to certify that the work outlined in this thesis entitled " **Studies on the stress Fluctuations in sheared Stokesian suspensions using chaos theory and nonlinear dynamics** " is an authentic record of the research work carried out by **Mr. J. Dasan** under my guidance in partial fulfillment of the requirements for the degree of **Doctor of Philosophy** of the **Cochin University of Science and Technology** and Further that no part thereof has been submitted elsewhere for any other degree.

T.R. Ramamohan
Dr. T. R. Ramamohan
Supervising guide
1-11-2005

तार/Telegram : कोनसर्च /'CONSEARCH', फैक्स Fax : (0091) (0471)2491712, 2491895, 24910186, 2491842, 2490389
फोन / Phone [Epabx] (0471) : 2490674, 2490224, 2490811, 2490851, 2490852
इमेल / Email <root@csrflrrd.ren.nic.in><rrltvm@md2.vsnl.net.in>. वेबसाइट/Website:http://w3rrlt.csir.res.in

Abstract

We report results obtained from a detailed analysis of the fluctuations of the rheological parameters viz. shear and normal stresses, simulated by means of the Stokesian Dynamics method, of a macroscopically homogeneous sheared suspension of neutrally buoyant non-Brownian suspension of identical spheres in the Couette gap between two parallel walls in the limit of vanishingly small Reynolds numbers using the tools of nonlinear dynamics and chaos theory for a range of particle concentration and Couette gaps. We make extensive use of the tools of nonlinear dynamics and chaos theory viz. average mutual information [sec.4.3.2], space-time separation plots [sec.4.3.3], visual recurrence analysis [sec.4.5.2], principal component analysis [sec.4.4.3], false nearest-neighbor technique [sec.4.4.2], correlation integrals [sec.2.8.3], computation of Lyapunov exponents [sec.4.5.3] for a range of area fraction of particles and for different Couette gaps.

We present numerical evidence for the existence of a low-dimensional chaotic attractor in the rheological properties for a range of particle concentrations. This indicates that the fluctuations of the rheological parameters arise from low dimensional deterministic dynamics. The chaotic nature of the underlying attractor governing the dynamics of the system in the stress fluctuations implies that, though the system is unpredictable in the long-term, accurate and meaningful short-term predictions can be performed depending on the accuracy of the initial conditions and the value of Lyapunov exponent, which characterizes the sensitive dependence of the dynamics on the initial conditions (the chaotic nature of the system). Using this information we performed predictions of successive fluctuations of the stresses from preceding fluctuations by using the one-step prediction method.

We found that the correlation dimension, the number of significant eigen values and the embedding dimension at which the percentage of false nearest-neighbors reduced to nearly zero are the same for both the normal and shear stress components for a fixed area fraction of particles. We computed the mutual false nearest-neighbor parameter

[sec.4.7] and observed the presence of a functional cross-correlation between shear and normal stress components. This is in agreement with the finding that the different stress components have the same correlation dimension and number of principal components etc. This characterization helped us to perform a cross-prediction of the time series of one stress component from the time series of another; thus indicating the potential of this approach.

One important implication of our analysis is that only a finite (atmost eight) number of independent variables are sufficient to describe the complete dynamics of the rheological parameters over the range of particle concentrations $\phi = 0.05$ to $\phi = 0.6$. This observation has potential applications to some industrial problems. Many industrial suspensions can be approximated by the bounded system of suspension of spheres in simple shear flow. Hence if we are able to identify the principal factors, at most eight in number, that govern the dynamics and rheological properties of such suspensions, we will be able to improve processes for the manufacture of products involving suspensions by controlling these factors appropriately.

Our analysis of the stress fluctuations for a range of particle concentrations revealed that the invariant measures such as the correlation dimension, number of principal components, the embedding dimension of the attractor (these are geometrical characteristics) and Lyapunov exponent (dynamical characteristic) that characterize the fluctuations change with rise in concentration, suggesting changes in the microstructure with increasing concentration. This in fact mimics the increasing complexity of the suspension due to the existence of particle-particle and many-body interactions. This may yield guidelines for the control of parameters governing the processing of such suspensions. From our results, we draw interesting conclusions on the relation between microstructure and rheology of the suspension.

Using the insight gained from the analysis of the simulated stress components, we model the system dynamics by means of an evolutionary algorithm called 'Darwin' [Alvarez *et al.*, 2001] [7]. We modeled the stress components and our models agree qualitatively and to a great extent quantitatively with the characteristics of the stress components simulated using the Stokesian Dynamic Simulation. The form of the different model equations for different area fractions of particles hints at the possible existence of a general model equation for the stress component with area fraction as a parameter. To make a conclusive assertion of this possibility further analysis is required, which we leave for future work.

Contents

List of Figures

List of Tables

CHAPTER 1

Introduction

1.1 Preface

> God plays dice with the universe. But they are loaded dice. And the main objective of science now is to find out by what rules were they loaded and how can we use them for our own ends.

is the answer of Joseph Ford to one of Einstein's famous questions "Does god play dice with the universe?".

Chaos brings to mind images of complete randomness, of disorder and anarchy. In 1986, at a conference on mathematical chaos held by the Royal Society in London, mathematicians were asked to define the "chaos" that had become the buzzword for their hot research area. After much deliberation, they offered the following: *Stochastic behavior occuring in a deterministic system.* As definitions go, this one is particularly constipated quite far from fostering any intution about the subject. In Stewart's *Does God Play Dice?*, he claims knowledge of the etymology of *stochastic* in the statement, "The Greek word *stochastikos* means 'skillful in aiming' and thus conveys the idea of using the laws of chance for personal benefit." According to Stewart, *Stochastic behavior* is *probabilistic behavior.* By placing both *stochastic* and *deterministic* in the same definition, the mathematicians have formed a bridge between the two sciences - two sciences that were regarded as mutually exclusive until then. *Chaos is the study of deterministic and bounded systems that give rise to aperiodic solutions that are so sensitive to measurement that their output appears random.* The term chaos was first introduced in its present connotation by James Yorke and T. Y. Li in 1976.

Edward Lorenz's first experience with chaos is dramatic. In 1961, Edward Lorenz had managed to create a skeleton of a weather system from a handful of differential equations. The statistical weather forecasting community at the time was developing sophisticated linear methods for prediction. Lorenz had come to the conclusion that there had to be a fundamental factor, as yet missing, limiting the success of linear models in weather prediction. He was trying to demonstrate this point by finding solutions to his miniature atmospheric model that were not periodic nor asymptotically periodic. He kept a continuous simulation running on an extremely primitive computer that would output a day's progress in the simulation every minute as a line of text on a roll of paper. Evidently, the whole system was very successful at producing "weather-like" output - nothing ever happend the same way twice, but there was an underlying order that delighted Lorenz and his associates.

"... Line by line, the winds and temperature in Lorenz's printouts seemed to behave in a recognizable earthly way. They matched his cherished intuition about the weather, he sensed that it repeated itself, displaying familiar patterns over time, pressure rising and falling, the airstream swinging north and south..."

Even though a computer had control of the simulation, and certainly possessed the capability to generate random numbers at will, there was nothing random about any portion of the way the simulation was supposed to work. It merely followed the laws of calculus as set down by Sir Isaac Newton himself and outputted a day's worth of virtual weather at the end of each minute. Lorenz's initial brush with chaos is described best by

James Gleick's words, from *Chaos*:

"One day in the winter of 1961, wanting to examine one sequence at greater length, Lorenz took a shortcut. Instead of starting the whole run over, he started midway through. To give the machine its initial conditions, he typed the numbers straight from the earlier printout. Then he walked down the hall to get away from the noise and drink a cup of coffee. When he returned an hour later, he saw something unexpected, something that planted a seed for a new science. This new run should have exactly duplicated the old. Lorenz had copied the numbers into the machine himself. The program had not changed. Yet as he stared at the new printout, Lorenz saw his weather diverging so rapidly from the pattern of the last run that, within just a few months, all resemblance had disappeared. He looked at one set of numbers, then back at the other. He might as well have chosen two random weathers out of a hat. His first thought was that another vacuum tube had gone bad. Suddenly he realized the truth. There had been no malfunction. The problem lay in the numbers he had typed. In the computer's memory, six decimal places were stored: 0.506127. On the printout, to save space, just three appeared: 0.506. Lorenz had entered the shorter, rounded-off numbers, assuming that the difference - one part in a thousand - was inconsequential. It was a reasonable assumption. If a weather satellite can read ocean-surface temperature to within one part in a thousand, its operators consider themselves lucky. Lorenz's Royal McBee was implementing the classical program. It used a purely deterministic system of equations. Given a particular starting point, the weather would unfold exactly the same way each time. Given a slightly different starting point, the weather should unfold in a slightly different way. A small numerical error was like a small puff of wind - surely the small puffs faded or cancelled each other out before they could change important, large-scale features of the weather. Yet in Lorenz's particular system of equations, *small errors proved catastrophic.*"

Lorenz entitled a 1979 paper, "Predictability: Does the Flap of a Butterfly's Wings in Brazil Set Off a Tornado in Texas?" and the title stuck. Today, *sensitive dependence on initial conditions* is referred to as "The Butterfly Effect." For the purposes of experimentation, Lorenz created a new system with three nonlinear differential equations (1.1). It is a reduced model of convection, similar to the swirls of cream in a hot cup of coffee, only much simpler.

$$\begin{aligned}\frac{dx}{dt} &= -\sigma x + \sigma y\\ \frac{dy}{dt} &= rx - xz - y\\ \frac{dz}{dt} &= xy - bz\end{aligned} \tag{1.1}$$

In this highly idealized model of a fluid, the Prandtl number σ, the Rayleigh number r, and b are parameters of the system. The variable x is proportional to the circulatory fluid flow velocity, the width of the flow is proportional to the parameter b, the variable y is proportional to the temperature difference between ascending and descending fluid elements and z is proportional to the distortion of the vertical temperature profile from its equilibrium. Lorenz's system, although simple in the eyes of a physicist or mathematician, is actually an unsolvable problem except by numerical methods. For the choice of parameters $\sigma = 10, b = \frac{8}{3}$, Lorenz numerically found that the system behaves erratically

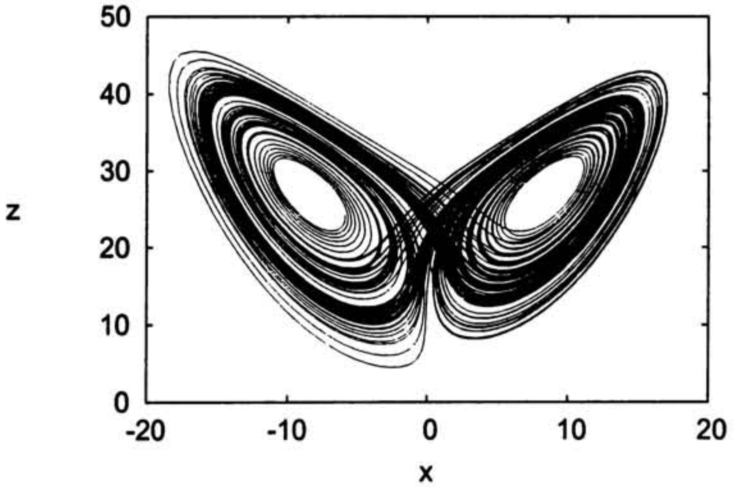

Figure 1.1: A typical figure showing the Lorenz attractor

whenever the Rayleigh number r exceeds a critical value $r \approx 24.74$. That is, all solutions appear to be sensitive to initial conditions, and almost all of them are apparently neither periodic solutions nor convergent to periodic (asymptotically periodic) solutions or equilibria. At first glance, the figures produced by the numerical data of the equations appeared to be random fluctuations coming from what should be a completely deterministic set of equations. Figure (1.1) shows a typical attractor of Lorenz's system and this figure shows the sensitivity of the dynamical system. The type of behavior is often discarded as simply an error in calculation. Lorenz was the first to recognize this erratic behavior as something other than error, and that everyone had been trying to view the world through a microscope. When he put the microscope aside and looked with his eyes, what he saw was an undeniable order, born of the randomness. That's the beauty and underlying order in chaos.

1.2 Review of literature

The mathematics of dynamical systems theory, which encompasses the concepts of multiplicity of a solution set and chaoticity of a dynamical trajectory, has an illustrious history of over one century. The theory of multiplicity of solutions of nonlinear evolution equations became a branch of mathematics called Bifurcation Theory, which include the three distinct components: critical solutions, stability, and structural stability. Progress in this field has enhanced clear understanding of how multiple solutions can exist in nonlinear systems and how the number of solutions and stability of solutions change as an experimental control, or stress parameter is changed. The crucial question of stability of solutions, whether or not a solution persits under an infinitesimal perturbation and how it changes as the number of solutions change, has occupied the time of many great mathematicians like Lagrange, Laplace and Dirichlet etc. of the eighteenth and nineteenth centuries. Their ultimate aim was to shed light on the age-old n-body problem and in doing so to determine the stability of the solar system.

In the year 1776, Pierre Simmon de Laplace wrote,

> The present state of nature is evidently a consequence of what it was in the preceding moment, and if we conceive of an intelligence which at a given instant comprehends of all the relations of the entities of this universe, it could state the expected positions, motions, and general effects of all these entities at any time in the past or future.

Laplace claimed that he had indeed proved, using a series expansion technique, that the solar system is stable. The significance of Laplace's claim reinforced the opinion held by many scientists: that once an intial condition (or configuration) is specified the future is completely determined. But, Henri Poincaré proved [105] that the series expansion of Laplace diverged and hence stability can not be assured. His contribution provided fresh insight into the problem of stability and in doing so it also ended the quantitative era. One of the Poincaré's most important inceptions was the introduction of qualitative dynamics and it gave birth to a host of important papers [Poincaré , 1880, 1890, 1899] [107], [106], [105]. In his seminal paper [107] he gave a mathematically precise criterion for a system to undergo fundamental qualitative change in nature as parameters of the system are changed. One of those conditions requires a change in the number of critical solutions.

In 1903, Poincaré stated that:

> A very small cause which escapes our notice determines a considerable effect that we can not fail to see ··· even in the case that the natural laws had no longer any secret for us, we could only know the initial situation approximately ··· It may happen that small differences in initial conditions produce very great ones in the final phenomena.

This is the sensitivity to initial conditions which is the distinguishing characteristic of deterministic chaotic systems.

Deterministic chaos with its inherent sensitivity to initial conditions (instability), provides a fresh insight into problems encountered in dynamics. Towards the end of nineteenth century, the theory of bifurcations, due to Poincaré, was formulated. However, the conceptual basis of bifurcation theory was begun by Leonhard Euler, predating Poincaré's effort with work published in 1774 on the buckling of loaded struts. The Russian academician A. M. Lyapunov [Lyapunov, 1947] [83] continued the spirit of Poincaré's work and made significant advances in the formulation of the notion of stability [83] and it is his definition of stability we often use today. Poincaré is one of the earliest contributors to bifurcation theory and hence initiated the development of dynamical system theory. Birkhoff's work[Birkhoff, 1960] [17] has greatly influenced our understanding of resonances. Julia in 1917 contributed greatly to the inception and understanding of complex analytical maps and this was substantially enhanced by Mandelbrot[Mandelbrot, 1975] [85]. Kolmogorov and Arnold opened up a new chapter in dynamical systems theory with the proving of the so-called KAM theory, which is important in the understanding of *elliptic points* in dynamical systems.

A significant development in chaos occurred in 1963 with Lorenz's seminal paper [82] on deterministic nonperiodic flow, an article concerned with turbulence. He discovered aperiodic solutions of a set of three ordinary differential equations by numerical integrations. These equations are a crude caricature of the Navier-Stokes equations. Lorenz's contribution marked a perceptual change which altered the face of nonlinear dynamics. The discrete analogue of Lorenz's initiative, pursued altogether independently, focussed on difference equations. Difference equations or maps were advocated originally as models for ecological systems. A difference equation or map is an example of a dynamical system in which time is discrete. Extensive study of these maps by biologists gave much impetus to the understanding of chaotic dynamics of maps and in particular 'period doubling' in which a fixed point of the map becomes unstable to a new solution whose period is double that of the previous solution. One dimensional maps are better platforms to study this behavior than three-dimensional sets of differential equations, which is the lowest-dimension of dynamical system described by differential equations capable of exhibiting chaotic dynamics.

The modern theory of dynamical system was conceived by S. Smale [Smale, 1967] [127] of USA and he invented a bizarre mathematical entity known as a 'Smale horseshoe'. Ruelle in France, and Takens in Holland developed a new theory of turbulence [Ruelle and Taken, 1971] [115] based on the theory of 'strange attractors', which challenged the Landau [Landau, 1959] [78] view of turbulence. Landau viewed turbulence as a confluence of quasiperiodic mayhem. He viewed a physical system becoming more and more turbulent as a result of the number of independent quasiperiodic motions progressively increasing. However, when there are nonlinear interactions between the excited oscillators, the net result is that there can be a complex finite-dimensional motion that need not be quasi-periodic. The important result suggested by [Ruelle and Takens, 1971] [115] is due to the nonlinear coupling between oscillators corresponding to different frequencies; this tends to destroy quasi-periodicity and replace it by motion which is *chaotic.*

Lorenz's contribution and the work on mapping in the early 1970's by Yorke, May, Oster and others provided two strands in a narrative which has exploded into a growing realization that the simplest deterministic rules can generate dynamical trajectories which not only look like the result of some random process but further more have the important property of sensitivity to initial conditions. This means that even if the rule defining evolution of a chaotic dynamical system were known exactly, long-term prediction would still be impossible, not simply because the motion was 'random', but because two nearly equivalent starting conditions could give distinctly diffferent solutions, which diverge at an exponential rate. The development of dynamical system theory in general, and Lorenz's contribution and May's [87] review in Nature in particular, triggered a change in perception: that a large number of complicated equations were not necessary for solutions to be chaotic or turbulent like.

Before the advent of sophisticated analytical tools and fast computing, nonlinear systems were studied under linear approximations. The famous Fermi-Pasta-Ulam numerical experiments in the year 1955 on energy sharing between modes in anharmonic lattices gave birth to the golden era of modern nonlinear dynamics. As described above, in the year 1963, E. N. Lorenz numerically integrated the simplified system of the three coupled first-order nonlinear equations of the fluid convection model describing atmospheric weather conditions. In 1965, Zabusky and Kruskal numerically analysed the initial value problem of the Korteweg-de Vries equation, which represents a nonlinear dispersive system. They observed a phenomenon completely opposite to that of chaos. In experiments they found that solitary waves interacted among themselves and re-emerged unchanged in form and speed. This phenomenon they named as a *soliton* and further Kruskal and coworkers developed a completely analytic procedure called the ***inverse scattering transform*** to solve the initial value problem of the Korteweg-de Vries equation. This marked the advent of the modern era of integrable nonlinear systems. Independent of these developments, various important studies on nonlinear diffusive and dissipative systems and the underlying patterns were pursued during the above period. Over the last few decades, chaotic behavior of nonlinear dynamical processes has been reported in many scientific fields such as hydrodynamics [66], [Radhkrishnan *et al.*, 1999] [110], [Asokan *et al.*, 2005] [10] astrophysics, chemistry [Kiss *et al.*, 1997] [74], biology [Bianchi *et al.*, 1992] [16], electronics, optics [Sivaprakasam and Shore, 1999] [126]. Chaotic dynamics appears to provide a relatively simple and possibly more satisfactory explanation of complex phenomena. Chaos in a bounded dynamical system is essentially characterized by the exponential divergence of initially adjacent trajectories as the system evolves in time. Scientists and engineers have begun to appreciate the advantages of designing devices to exploit, rather than disregard, nonlinearity and chaos. When observations from a dynamical system shows rather irregular fluctuations, we try to check whether the flutuations are due to chaos. The existence of chaos shows that the underlying dynamics is deterministc and short term prediction of the future states is possible using the tools of nonlinear dynamics.

In recent times increasing attention has been focussed on exploring real technological applications of nonlinear dynamics: Controlling chaos [121], [Anil Kumar *et al.*, 2000] [8], [Meucci *et al.*, 2004] [88],[Heitor *et al.*, 2004] [61], [Mahmoud and Farhaly, 2004] [84], synchronization of chaos [Ricardo Femat and José Alvarez-Ramí , 1997] [111], [Moukam Kakmeni *et al.*, 2004] [91] and secure communication [Sivaprakasam and Shore, 1999] [126], magnetoelectronics, spatio-temporal patterns etc. There are systems in which the chaotic behavior can be controlled by simple map based algorithms [Kiss *et al.*, 1997] [74]. Applications of nonlinear dynamics have been found throughout the fields of physics, engineering, chemistry and biology [Viktor Muller *et al.*, 2001] [137]. Numerous mathematical ideas and techniques hve been used to study nonlinear systems and these, in turn, have enriched the field of mathematics itself.

Prior to the development of methods of analysis for nonlinear systems, any irregularly varying data was assumed to either be not amenable to analysis in terms of deterministic models or to require a very complicated model. The demonstration that simple deterministic models can lead to complicated and irregular, or chaotic, behavior opened up the possibility of analysing such data using deterministic models. Chaos is a phenomenon that has been found in many physical systems and has been confirmed both theoretically and experimentally [Gaspard *et al.*, 1998] [50], [Kiss *et al.*, 1997] [74]. Understanding chaos offers the possibility of control over some complex and elusive processes [Christini *et al.*, 1996] [29], [Ciofini *et al.*, 1995] [30]. One important application where chaos theory has been shown to be beneficial is in the understanding and exploitation of fluid mixing [Zumbrunnen *et al.* 1996] [142]. In this case, a combination of chaos theory, fluid mechanics and transport phenomena has produced a general framework that now can be used in a variety of practical situations [Ottino, 1989] [97]. Thus, the presence of deterministic chaos shows that one need not discard the given data due to the apparent randomness, but one can analyse the data from another perspective using advanced mathematical tools and we can gain much information about the system behavior and predict the future behavior upto a finitely large number of iterations to the future depending on certain characteristics of the system.

1.3 Rheological parameters

Rheological properties of suspensions are examples of spatial averages over a large number of elements, which are individually chaotically varying (here the suspended particles exhibit chaotic motion), showing a variety of interesting behavior. The bulk stress in a suspension of small particles in a fluid depends on many factors, of which particle concentration, the Stokes number (which characterizes the importance of particle inertia in comparison with viscous forces), colloidal and Brownian forces, and flow type are important. The dynamic interaction of these factors determines the suspension microstructure, from which the macroscopic rheological properties follow. Particulate suspensions are, of course, encountered frequently in a variety of industrial processes, and understanding their rheology can provide significant commercial benefit. Moreover, suspensions are useful models of spatially extended chaotic systems, which can be analyzed both theoretically and experimentally, and their rheological properties represent easily measurable spatial averages over the positions of all the particles.

There is a host of literature which studies the shear viscosity of suspensions either by experimentation or numerical simulations, with the implicit assumption that their behavior is Newtonian. Recent experimental evidence strongly suggests that suspensions behave macroscopically as non-Newtonian fluids whose rheological properties are influenced by a large number of factors. The presence of normal stresses in viscometric flows that vary linearly with the shear rate shows non-Newtonian characteristics [Brady and Morris, 1997] [18] [Phung *et al.*, 1996] [104]. The presence of rate dependent normal stresses is a non-Newtonian character, because the pressure in a Newtonian fluid in a viscometric flow is determined solely from the boundary conditions and the hydrodynamic balance of forces; there is no rate dependence of the pressure in Newtonian fluid. There are also normal stress differences in a supension which is evidently a non-Newtonian effect. The normal stresses and particle pressure in a non-colloidal suspension are worthy of investigation from a fundamental standpoint as they are the only non-Newtonian characters it exhibits; shear thinning or thickening and viscoelastic effects are generally not observed unless there are significant non-hydrodynamic interactions between the suspended particles. From the practical view point, normal stress differences are an important consideration in the processing of concentrated suspensions. Such study is of even greater significance because normal stresses determine segregation of particles in suspension subjected to an inhomogeneous shear field [Jenkins and Mctigue, 1990] [67], [Morris and Boulay, 1999] [89], [Nott and Brady, 1994] [94]. The particle pressure which is related to the fluctuational motion of the particles can be an important parameter in designing the flow of suspensions in slurry pumps, pipes, fluidised beds etc. While the particle pressure shows no apparent effect in a homogeneous suspension undergoing uniform deformation, Nott and Brady [1994] [94] argued that its role in inhomogeneous shear is important. Brady and Morris [1997][18] argued that the presence of a non-hydrodynamic interaction force, however small, results in non-Newtonian effects such as normal stress differences. Though it is not clear that non-hydrodynamic forces are necessary, normal stress differences have been measured experimentally in non-Brownian suspensions by [Gadala-Maria, 1979] [48], [Zarraga *et al.*, 2000] [140] and [Singh and Nott, 2003] [124], and in numerical simulations by [Singh and Nott, 2000] [122].

For Stokesian suspensions, the stress is simply a product of the fluid viscosity, the shear rate and a function of the microstructure - the distribution of particles in the suspension as the system evolves in time. Hence, fluctuations in the stress reflect directly on fluctuations on the microstructure. For dilute suspensions, hydrodynamic interactions may be assumed to be pairwise, and the stress is therefore determined by the pair distribution function. Batchelor and Green [1972] [15] determined analytically the steady state pair distribution function for pure straining flow assuming only hydrodynamic interactions between particles, and thereby computed the $O(\phi^2)$ correction to the suspension viscosity. Recently, Brady and Morris [1997] [18] determined the pair distribution function for shear flow for a weakly Brownian suspension with a repulsive inter-particle force in addition to the hydrodynamic force. They found that the repulsive interaction breaks the fore-aft symmetry of the pair distribution function, and therefore leads to finite normal stress differences in the suspension. Both these studies considered unbounded flows for which there is a time-independent steady state in the microstructure for dilute suspensions.

1.4 Our work

The studies cited above attempt to determine the time and space averaged bulk stress in the suspension for a prescribed flow field. From a microstructural viewpoint, fluctuations in the stress are caused by temporal changes in the microstructure, which in turn arise from two sources: (1) The chaotic motion of individual particles in the suspension, and (2) fluctuations in the spatially averaged microstructure due to a coupling between its evolution and the flow. The former exists even in molecular systems, but its characteristic time-scale is so small that it is unimportant in the hydrodynamic sense. In suspension flows, the only time-scale is that imposed by the shear rate, and therefore the effects of the two mechanisms listed above are indistinguishable. These fluctuations in the averaged bulk stresses, to our knowledge, have not been studied using methods of nonlinear time series analysis and chaos theory, and it is our belief that examining them through the conceptual lens of nonlinear dynamics and chaos theory would lead to a better understanding of the system behaviour and it will be of significant industrial benefit.

A large number of studies in the literature shows that the stress in a particulate suspension exhibits strong fluctuations about a well defined average [Singh and Nott, 2000] [122]. The fluctuations increase in magnitude with the particle concentration and are easily measurable in experiments; but only the temporal average is usually reported. Stress fluctuations in suspension flows have been observed in the simulations of pressure driven flows and simple shear flow [Nott and Brady, 1994] [94]; [Singh and Nott, 2000] [122]. It is now widely recognized that the fluctuations in the properties of non-linear systems convey useful information on their dynamics. The utilization of the tools of nonlinear dynamics and chaos theory has led to the possibility of uncovering information about the underlying dynamics of a system whose output is in the form of a fluctuating time series [Pavlos *et al.* 1999a, 1999b,1999c] [98], [99], [100]. Our broad objectives in this work are to see whether these tools [Kantz and Schreiber, 1997] [69], [Hegger *et al.*, 1999] [60], when applied to fluctuations in the bulk stress of Stokesian suspensions, can capture information about their underlying dynamics, and hence lead to a way of characterizing their behavior by proper estimates of the dynamical and topological (geometrical) invariants of the fluctuating time series, such as dimension estimates, Lyapunov exponents and principal eigenvalues etc. Some of the possible advantages of studying fluctuations in rheological properties using the tools of nonlinear dynamics and chaos theory are:

- The identification of the existence of a low-dimensional attractor leading to the possibility of intelligent chaos control.
- Accurate short range predictions of fluctuations.
- Predicting fluctuations in properties that are difficult to measure from those that are easy to measure.
- Developing phenomenological global models to describe the system behavior using possible simple equations.
- Analysis of the system dynamics by controlling the temporal fluctuations of the stress components through appropriate variation of the parameters in the model equation.
- Synchronization of one stress component with another stress component.
- Analysis of the system by expanding the parameter space to search for new phenomena or already existing phenomena of similar (or related) systems.
- Using the invariant measures of the dynamics in design and scale-up of equipment and so on.

From a fundamental viewpoint, we expect that an analysis of the stress fluctuations using the tools of nonlinear dynamics and chaos theory such as the estimation of geometrical (topological) characteristics viz. the number of principal components [4.4.3], correlation dimension [2.8.3], embedding dimension [4.4.2] of the underlying attractor and dynamical characteristics such as Lyapunov expoenents [4.5.3] will provide useful information on the microstructure, or arrangement of particles during shear.

In this work, we report results obtained from a detailed analysis [Dasan *et al.*, 2002] [32] of the fluctuations of the rheological parameters viz. shear and normal stresses, simulated by means of the Stokesian Dynamics (see chap. 3 and the references therein), of a macroscopically homogeneous sheared suspension of neutrally buoyant non-Brownian suspension of identical spheres in the Couette gap H between two parallel walls in the limit of vanishingly small Reynolds numbers using the tools of nonlinear dynamics and chaos theory [Kantz and Schreiber, 1997][69], [Hegger *et al.*, 1999] [60] for a range of particle concentration (area fraction of particles ϕ , for we consider only two dimensional flows. See chap. 3 for more details) and Couette gaps H. This system is currently an active research field in the literature [Singh and Nott, 2000, 2003] [122], [124]; [Drazer *et al.*, 2002, 2004] [35], [36], [Acrivos *et al.*, 2004] [4]; [Strybulevych *et al.*, 2004] [128]. Singh and Nott [2000][122] modified the Stokesian Dynamics simulation technique originally developed by Brady and Bossis [1988] [19] and used by many others for studying a large number of different types of suspensions viz. non-colloidal sheared suspensions [Brady & Bossis, 1985] [21], [Durlofsky and Brady, 1989] [38], flow through porous media [Durlofsky and Brady, 1987] [37] and pressure driven flows [Nott and Brady, 1994] [94] (see chap.3). To simulate plane walls more accurately Singh and Nott[2000] [122] modified the procedure of Nott and Brady [1994] [94] and simulated the velocity fluctuations, bulk stresses viz. normal and shear stresses both numerically and experimentally [Singh and Nott, 2003] [124] for different area fraction of particles. Singh and Nott performed a comparative study of both theoretical stress components and experimentally measured stresses. However, they [Singh and Nott, 2000, 2003] [122], [124] did not analyse these fluctuations using the methods of nonlinear dynamics and chaos theory. Contemporary to our work [Dasan *et al.*, 2002] [32], Drazer *et al.*, [2002, 2004][35], [36] and Acrivos *et al.*[2004][4] investigated the velocity fluctuations present in this system and their dependence on the microstructure developed by the suspensions using Stokesian Dynamics simulations. Drazer *et al.*[2002] [35] did not analyse the fluctuations of stress components. Strybulevych *et al.* [2004] [128] analyse the measurements of the steady-state shear viscosity and shear-induced microstructure of a system of glass beads (diameter d = 127±22 μm, density ρ = 2,220 kg/m^3) immersed in a density-matched liquid. We analyse the normal stress and shear stress of the system simulated by means of the Stokesian Dynamics method modified by Singh and Nott [2000] [122] using topological and dynamical methods. We make extensive use of the tools of nonlinear dynamics and chaos theory viz. average mutual information [4.3.2], space-time separation plots [4.3.3], visual recurrence analysis [4.5.2], principal component analysis [4.4.3], false nearest-neighbor technique [4.4.2], correlation integrals [2.8.3], computation of the maximum Lyapunov exponents [4.5.3], mutual false nearest-neighbor parameter [4.7] for a range of area fraction $0.05 \leq \phi \leq 0.6$ of particles and for different Couette gaps H. The only parameters in the problem are the Couette gap H (rendered non-dimensional by the particle radius), the area fraction of particles ϕ, the parameters F_0 that determine the magnitude of repulsive interaction (3.24) and μ, the range of repulsive interaction.

Most of our results were obtained with Couette gap H = 18 particles width, and $F_0 = 10^{-4}$, $\mu = 100$, and particle area fraction in the range $0.05 \leq \phi \leq 0.6$. We have studied the effect of H by performing simulations for H=14, 18, 30 particle width for ϕ =0.2 and F_0 and μ remaining as above. To study the sensitivity of our results to the repulsive interaction (3.24), we have performed simulations for μ =10, 100, and 1000, keeping $F_0\,\mu = 0.01$ for ϕ =0.4 and H = 18 particles width.

We present numerical evidence for the existence of a low-dimensional chaotic attractor in the rheological properties for a range of particle concentrations. This indicates that the fluctuations of the rheological parameters arise from low-dimensional deterministic dynamics. The chaotic nature of the underlying attractor governing the dynamics of the system in the stress fluctuations implies that, though the system is unpredictable in the long-term, accurate and meaningful short-term predictions can be performed depending on the accuracy of the initial conditions and the value of the Lyapunov exponent, which characterizes the sensitive dependence of the dynamics on the initial conditions (the chaotic nature of the system). Using this information we performed predictions of successive fluctuations of the stresses from preceding fluctuations by using the one-step prediction method [sec.4.6]. We found that the correlation dimension, the number of significant eigen values and the embedding dimension at which the percentage of false nearest-neighbors reduced to nearly zero are the same for both the normal and shear stress components for a fixed area fraction of particles. We computed the mutual false nearest-neighbor parameter [sec.4.7] and observed the presence of a functional cross-correlation between shear and normal stress components. This is in agreement with the finding that the different stress components have the same correlation dimension and number of principal components etc. This characterization helped us to perform a cross-prediction of the time series of one stress component from the time series of another; thus indicating the potential of this approach. One important implication of our analysis is that only a finite (atmost eight) number of independent variables are sufficient to describe the complete dynamics of the rheological parameters over the range of particle concentrations $\phi = 0.05$ to $\phi = 0.6$. This observation has potential applications to some industrial problems. Many industrial suspensions can be approximated by the bounded system of suspension of spheres in simple shear flow. So if we are able to identify the principal factors, at most eight in number, that govern the dynamics and rheological properties of such suspensions, we will be able to improve processes for the manufacture of products involving suspensions by controlling these factors appropriately. Our analysis of the stress fluctuations for a range of particle concentrations revealed that the invariant measures such as the correlation dimension, number of principal components, the embedding dimension of the attractor (these are geometrical characteristics) and Lyapunov exponent (dynamical characteristic) that characterize the fluctuations change with increase in concentration, suggesting changes in the microstructure with increasing concentration.

This in fact mimics the increasing complexity of the suspension due to the existence of particle-particle and many-body interactions. This may yield guidelines for the control of parameters governing the processing of such suspensions. From our results, we draw interesting conclusions on the relation between microstructure and rheology of the suspension.

Using the insight gained from the analysis of the simulated stress components, we model the system dynamics by means of an evolutionary algorithm called 'Darwin'[Alvarez *et al.*, 2001] [7]. We modeled the stress components and our models agree qualitatively and to a great extent quantitatively with the characteristics of the stress components simulated using the Stokesian Dynamic simulation.

1.5 Organization of the thesis

This thesis consists of five chapters. The first chapter has five sections. The first two sections review the major milestones of chaotic dynamics and nonlinear dynamics. The third section describes the importance of rheological parameters and the fourth section gives a brief description of our work and its connection with works in the leterature. The last section of this chapter describes the organization of the thesis.

The second chapter introduces some basic terms of chaos theory and nonlinear dynamics. This chapter has eight sections. The first three sections introduce the basic terms of dynamical system and chaos theory and the fourth section describes methods to estimate the Lyapunov exponent from a map. The fifth and sixth sections describe basic ideas of differential equations and the corresponding notions of maps. The last two sections of this chapter describe different types of dimension estimates. (Other required terms and methods of nonlinear time series analysis using chaos theory and nonlinear dynamics will be described at the appropriate places.) The third chapter deals with the Stokesian dynamics simulation method for an unbounded and bounded flow.

The fourth chapter has eight sections. Section one is an introduction to nonlinear time series analysis and section two describes the phase space reconstruction method. Section three deals with different methods viz. autocorrelation function, average mutual information etc., of computing the proper time delay for embedding. Section four describes the different geometrical (topological) methods such as principal component analysis, false nearest neighbor method and correlation integral method to estimate the embedding dimension of the attractor. The fifth section describes the results of analysis using the above tools and discusses the implications of low-dimensionality, deterministic nature and the chaotic nature of the attractor. Section six of this chapter deals with successive prediction using local one-step and multi-step prediction methods. Cross-prediction of one time series from another time series is described in section seven. In the final section of this chapter a discussion of the results and its implications to the microstructure of the suspension is described.

The last chapter has seven sections. Section one gives an introduction to modeling and section two deals with the different stages of the evolutionary algorithm called 'Darwin', using which we develop global models of our system. In section three, we construct the model equations of the stress components for different particle concentrations. In section four, we compare and contrast qualitative and quantitative properties of model generated stress components with simulated stress components of the Stokesian suspensions. In section five, we discuss the implications of our analysis and model equations. In section six, we discuss possible future works. In the final section of this thesis, we give list of publications resulted during the research work.

CHAPTER 2

Dynamical Systems and Chaos

2.1 Dynamical System

A physical system which evolves with time is called a **dynamical system**. A dynamical system can be suitably modeled by differential equations, difference equations or integral equations. Dynamical systems are broadly classified into two: (1) Discrete dynamical systems and (2) Continuous dynamical systems. When the time is considered as a sequence of separate intervals each following the next one, the system is called a **Discrete dynamical system** and this type of system is represented by maps as follows

$$\boldsymbol{x}_{n+1} = f(\boldsymbol{x}_n) \tag{2.1}$$

where $\boldsymbol{x}_n$ is a vector representing the state space which gives a numerical description of the current configuration of the system dynamics and f is the rule which governs the system dynamic. Frequently cited examples of discrete dynamical systems are the Henon map, the logistic map (quadratic map), the Baker's map etc. When time varies continuously, the dynamical system is called continuous. **Continuous dynamical systems** are symbolically represented by differential equations as follows:

$$\frac{\mathrm{d}}{\mathrm{dt}}\boldsymbol{x}(t) = \mathrm{f}(\boldsymbol{x}(\mathrm{t})) \tag{2.2}$$

where $x(\mathrm{t})$ is the state space of the system at the instant t. *The collection of all states of a system is called the* **phase space** *of the dynamical system.* Note that a map describes the time evolution of a system by expressing its state as a function of its previous state and iterating the map corresponds to the system moving through time in discrete intervals. Instead of expressing the current state as a function of the previous state, a differential equation expresses the rate of change of the current state as a function of the current state. Frequently encountered examples of continuous dynamical systems in the literature are the Lorenz equations, Chua circuit etc. *If the evolution of the system explicitly depends on time, it is called a* **non-autonomous** *dynamical system.* In this case the right hand side of equation (2.2) contains time as a variable. *If the evolution of the system does not depend on time, it is called an* **autonomous** *dynamical system.* Every non-autonomous equation (dynamical system) can be converted into autonomous equations at the expense of one more state variable which is equivalent to the time variable.

2.2 Dynamical characteristics of maps

One of the most important uses of maps in scientific applications is to assist in the study of differential equation models. In any study of dynamical systems, we mainly focus our analysis on the eventual state of the system behavior in time for a proper understanding of the system itself. The **trajectory (or orbit)** of a dynamical system is defined as the sequence

$$\boldsymbol{x}_0,\ f(\boldsymbol{x}_0),\ f^2(\boldsymbol{x}_0),\ \ldots,\ f^n(\boldsymbol{x}_0),\ \ldots$$

where $\boldsymbol{x}_0$ is a vector, called initial condition, describing the initial configuration of the system dynamics and the meaning of $f^n(\boldsymbol{x}_0)$ is n successive application of f on the initial condition $\boldsymbol{x}_0$. A trajectory of a dynamical system is said to be **periodic** with period k if it repeats after k iterates (k successive application of f), k being the smallest number having this property, and in this situation we have

$$f^k(\boldsymbol{x}_0) = \boldsymbol{x}_0 \tag{2.3}$$

and the point $\boldsymbol{x}_0$ is called a **periodic point** of period k. A periodic point of period one is called a **fixed point**. That is, $f(\boldsymbol{x}_0) = \boldsymbol{x}_0$. This shows that a periodic point of period k will be a fixed point of f^k.

A fixed point $\boldsymbol{x}_0 \in \mathrm{R}^m$ of a map f on R^m is called an **attractor** (or **sink**) if there exists an $\epsilon > 0$ such that for all $\boldsymbol{x}$ in the ϵ- neighborhood $N_\epsilon(\boldsymbol{x}_0)$, $\lim_{k\to\infty} f^k(\boldsymbol{x}) = \boldsymbol{x}_0$. The fixed point $\boldsymbol{x}_0$ is called a **repeller** (or **source**) of f if there is an ϵ- neighborhood $N_\epsilon(\boldsymbol{x}_0)$ such that for all $\boldsymbol{x} \in N_\epsilon(\boldsymbol{x}_0)$ we can find a poistive integer k with the property that for all $n > k$, $f^n(\boldsymbol{x}_0) \notin N_\epsilon(\boldsymbol{x}_0)$. That is, any point that is very close to an attractor will move towards it as time progresses, but, for a repeller, the neighboring points eventually move away from it. In this sense, an attractor is a **stable fixed point**, but a repeller is an **unstable fixed point**. To describe the above characteristics of a map rigorously, we introduce the concept of Jacobian matrix for a map as follows:

Let $f = (f_1, f_2, f_3, \ldots, f_m)$ be a map on R^m and let $\boldsymbol{p} \in \mathrm{R}^m$. Then **Jacobian matrix** of f at $\boldsymbol{p}$, denoted by $Df(\boldsymbol{p})$ is defined by the matrix

$$Df(\boldsymbol{p}) = \begin{pmatrix} \frac{\partial f_1}{\partial x_1}(\boldsymbol{p}) & \frac{\partial f_1}{\partial x_2}(\boldsymbol{p}) & \cdots & \frac{\partial f_1}{\partial x_m}(\boldsymbol{p}) \\ \frac{\partial f_2}{\partial x_1}(\boldsymbol{p}) & \frac{\partial f_2}{\partial x_2}(\boldsymbol{p}) & \cdots & \frac{\partial f_2}{\partial x_m}(\boldsymbol{p}) \\ \cdots & \cdots & \cdots & \cdots \\ \frac{\partial f_m}{\partial x_1}(\boldsymbol{p}) & \frac{\partial f_m}{\partial x_2}(\boldsymbol{p}) & \cdots & \frac{\partial f_m}{\partial x_m}(\boldsymbol{p}) \end{pmatrix} \tag{2.4}$$

of partial derivatives evaluated at $\boldsymbol{p}$. Given a vector $\boldsymbol{p}$ and a small vector $\boldsymbol{h}$, the increment in f due to $\boldsymbol{h}$ is approximated by the Jacobian matrix times the vector $\boldsymbol{h}$ given by

$$f(\boldsymbol{p}+\boldsymbol{h}) - f(\boldsymbol{p}) \approx Df(\boldsymbol{p})\boldsymbol{h} \tag{2.5}$$

This shows that as long as the deviation is small, the action of the map near a fixed point $\boldsymbol{p}$ is essentially the same as the linear map $\boldsymbol{h} \to Df(\boldsymbol{p})\boldsymbol{h}$, with fixed point $\boldsymbol{h} = 0$. The equation (2.5) shows that at each iteration two arbitrarily close points move away (or closer) at a multiplicative rate of approximately $Df(\boldsymbol{p})$ until the orbits move significantly far away. The fixed point $\boldsymbol{p}$ of the map f will be an attractor (or sink) if the magnitude of each eigen value of $Df(\boldsymbol{p})$ is less than one and the fixed point $\boldsymbol{p}$ will be a repeller (or source) if the magnitude of each eigenvalue is greater than one. If none of the eigen values of $Df(\boldsymbol{p})$ has magnitude one, then the fixed point $\boldsymbol{p}$ is called **hyperbolic**. A hyperbolic fixed point $\boldsymbol{p}$ of f is said to be a **saddle point** if the Jacobian matrix $Df(\boldsymbol{p})$ has atleast one eigen value of magnitude less than one and at least one eigen value of magnitude greater than one. This, in fact, implies that saddle points can not occur for one-dimensional maps. The main difference between a saddle point and an attractor (or repeller) is that in one direction (that corresponds to the eigen value with magnitude less than one) neighboring points will move towards it and in another direction (that corresponds to the eigen value with magnitude greater than one) the neighboring points will move away from it eventually and may or may not be attracted to some stable fixed point. So a saddle point has both stable and unstable directions. A saddle fixed point is unstable as most initial values near it will move away under iteration of the map. However, not all nearby initial values move away from a saddle fixed point. The set of initial values that converge to the saddle point is called the **stable manifold** and the set of initial values that move away from the saddle point is called the **unstable manifold**.

As we observed, in the above discussion, one type of behavior for an initial condition that begins near an unstable steady state is for it to move away and be attracted by a stable steady state or by a stable periodic state. In this case the unstable behavior is transient and gives way eventually to stable behavior in the long run.

Lef f be a map on R^m and let $\boldsymbol{p}$ be an attracting fixed point or periodic point for f. Then the **basin of attraction** of $\boldsymbol{p}$ is defined as the set of points $\boldsymbol{x} \in \mathrm{R}^m$ such that $\lim_{n\to\infty} |f^n(\boldsymbol{x}) - f^n(\boldsymbol{p})| = 0$.

2.3 Lyapunov numbers and exponents of a map

In general, there is no reason that an initial condition starting near a repeller (or source) is forced to be attracted to a sink (or a periodic sink). A **chaotic trajectory** is one that forever continues to experience the unstable behavior that an orbit exhibits near a repeller, but that is not itself fixed or periodic. It never finds a sink to be attracted to. At any point of such an orbit, there are points arbitrarily near that will move away from the point at an exponential rate during further iteration (refer 2.5). This sustained irregularity is quantified using dynamical characteristics called **Lyapunov numbers** and **Lyapunov exponents**. The **Lyapunov number** is defined as the average per-step divergence rate of nearby points along the orbit, and the **Lyapunov exponent** is the natural logarithm of the Lyapunov number.

For an one-dimensional map f the orbit of the point x near the point x_1 will diverge from x_1 at a multiplicative rate of approximately $f'(x_1)$ per iteration (2.5), until the orbit of x moves significantly far away from the orbit of x_1. For a periodic point x_1 of period k, the orbit of each neighbor x separates from x_1 at a rate approximately the product of derivatives A of f at the k points of the orbit after each k iterates. And so the average multiplicative rate of separation of two neighboring orbits is $A^{\frac{1}{k}}$ per iteration. The Lyapunov number is introduced to quantify this average multiplicative rate of separation of neighboring points. The significance of the concept of Lyapunov number is that it can be applied to nonperiodic orbits. We, now, define Lyapunov number and exponent for a one-dimensional map.

Let f be a smooth map of the real line R. The Lyapunov number $L(x_1)$ of the orbit $(x_1, x_2, \ldots,)$ is defined as

$$L(x_1) = \lim_{n\to\infty} (|f'(x_1)||f'(x_2)|\cdots|f'(x_n)|)^{\frac{1}{n}} \tag{2.6}$$

if this limit exits. The Lyapunov exponent $h(x_1)$ is defined as

$$h(x_1) = \lim_{n\to\infty} \frac{1}{n}[\ln|f'(x_1)| + \ln|f'(x_2)| + \cdots + \ln|f'(x_n)|] \tag{2.7}$$

if this limit exists. Now it follows that if x_1 is a fixed point of f, its Lyapunov number is $|f'(x_1)|$ and so its Lyapunov exponent is $\ln|f'(x_1)|$. If x_1 is a periodic point of period k, then the Lyapunov exponent is

$$h(x_1) = \frac{\ln|f'(x_1)| + \ln|f'(x_2)| + \cdots + \ln|f'(x_n)|}{k} \tag{2.8}$$

For the periodic orbit the Lyapunov number $e^{h(x_1)}$ describes the average local stretching near a point on the orbit on a per-iterate basis.

A trajectory $(x_1, x_2, \ldots, x_n, \ldots)$ of a smooth map f is called **asymptotically periodic** if it converges to a periodic orbit as $n \to \infty$. That is, there exists a periodic orbit $(y_1, y_2, \ldots, y_k, y_1, y_2, y_3, \ldots)$ of period k such that

$$\lim_{n\to\infty} |x_n - y_n| = 0 \tag{2.9}$$

We have the following result in the case of asymptotically periodic orbit.

If the orbit $(x_1, x_2, \ldots)$ of f satisfies $f'(x_i) \neq 0$ for all i and is asymptotically periodic to the periodic orbit $(y_1, y_2, \ldots, y_k, y_1, y_2, y_3, \ldots)$, then the two orbits have identical Lyapunov exponents, if they exist[Kathleen [6].

We formally define a chaotic orbit as follows:

A bounded orbit of a map of the real line is said to be **chaotic** if it is not asymtotically periodic and has positive Lyapunov exponent.

The concept of Lyapunov numbers and Lyapunov exponents can be extended to higher dimensional maps defined on R^m, $m > 1$. In one dimensional maps, the idea is to measure separation rates of nearby points along the real line. In higher dimensions, nearby points may be moving apart along one direction, and moving together along another direction. For a map on R^m, each orbit has m Lyapunov numbers, which measure the rates of separation from the current orbit point along m orthogonal directions. These directions are determined by the dynamics of the map. The first will be along which the separation between nearby points is the greatest (or which is least contracting, if the map is contracting in all direction). The second will be the direction of greatest separation, chosen from all directions perpendicular to the first and the third will have the greatest stretching of all directions perpendicular to the first two directions, and so on. The stretching factors in each of these chosen directions are the Lyapunov numbers of the orbit.

Consider a unit m-dimensional sphere like object S about the first point $\boldsymbol{x}_0$ of the orbit under the map f defined on R^m, $m > 1$. If we examine the image $f(S)$ of the sphere like object under one iteration of the map, we observe an approximately "ellipsoidal" shape, with long axes along expanding directions for f and short axes along contracting directions. After n iterations of the map f, the sphere like object will evolve into a longer and thinner "ellipsoid" like object. The changes of the axes of the ellipsoid like object per iterate are the Lyapunov numbers and they quantify the amount of stretching and shrinking due to the dynamics near the orbit beginning at $\boldsymbol{x}_0$. So the Lyapunov numbers and exponents can be defined formally as follows:

Let f be a smooth map on R^m, S be the unit m-dimensional sphere about the first point $\boldsymbol{x}_0$ of the orbit and $J_n = Df^n(\boldsymbol{x}_0)$ be the Jacobian matrix of f^n at $\boldsymbol{x}_0$. Let r_k^n be the kth longest orthogonal axis of the ellipsoid J_nS. Then the kth Lyapunov number of $\boldsymbol{x}_0$ is defined by

$$L_k = \lim_{n\to\infty} (r_k^n)^{\frac{1}{n}} \tag{2.10}$$

if the limit exists. The kth Lyapunov exponent of $\boldsymbol{x}_0$ is given by $h_k = \ln L_k$.

Using the concept of Lyapunov exponent, we can extend the definition of chaotic orbit to orbits of higher dimensional maps analogously.

A bounded orbit $(\boldsymbol{x}_0, \boldsymbol{x}_1, \boldsymbol{x}_2, \dots)$ of map f defined on R^m, $m \geq 1$ is said to be chaotic if the orbit is not asymptotically periodic, no Lypunov exponent is exactly one and the largest Lyapunov exponent is greater than zero.

2.4 Estimation of the largest Lyapunov exponent

In general, there is no direct way to determine Lyapunov exponent from the knowledge of the map and its Jacobian matrices. In practice, it is very difficult to determine the Jacobian matrix $J_n = Df^n(\boldsymbol{x}_0)$ for large values n. We have to resort to the approximation of the image ellipsoid J_nS of the unit sphere S by computational algorithms. If the ellipsoid J_nS has semi-major axes of length s_i in the direction $\boldsymbol{u}_i$, the direct apporach to calculating the Lyapunov exponents would be to explicitly form $J_n\, J_n^T$ and find its eigenvalues s_i^2. In case the ellipsoid has stretching and strinking directions, it will be very long and very thin for large values of n. So, the eigenvalues of $J_n\, J_n^T$ will include both very large and very small numbers. Beacause of the limited number of digits allowed for each stored number, computer calculations become difficult when numbers of vastly different sizes are involved in the same calculation. The problem of computing the s_i gets worse as n increases. Because of this reason, direct calculation of the ellipsoid J_nS is usually avoided.

A better approach to numerical calculations involves following the ellipsoid as it grows. Since

$$J_nS = Df(\boldsymbol{x}_{n-1})Df(\boldsymbol{x}_{n-2})\cdots Df(\boldsymbol{x}_0)S, \tag{2.11}$$

we can compute one iterate at a time. We start with an orthonormal basis $\{\boldsymbol{y}_1^0, \boldsymbol{y}_2^0,$-$\boldsymbol{y}_3^0, \dots, \boldsymbol{y}_m^0\}$ for R^m, and compute the vectors $\boldsymbol{z}_1^0, \boldsymbol{z}_2^0, \dots, \boldsymbol{z}_m^0$:

$$\boldsymbol{z}_1^0 = Df(\boldsymbol{x}_0)\boldsymbol{y}_1^0,\ \boldsymbol{z}_2^0 = Df(\boldsymbol{x}_0)\boldsymbol{y}_2^0,\ \cdots,\ \boldsymbol{z}_m^0 = Df(\boldsymbol{x}_0)\boldsymbol{y}_m^0 \tag{2.12}$$

These vectors lie on the new ellipse $Df(\boldsymbol{x}_0)S$, but they not necessarily orthogonal. Using the Gram-Schmidt orthogonalization procedure, we can construct an orthogonal basis $\{\boldsymbol{y}_1^1, \boldsymbol{y}_2^1, \boldsymbol{y}_3^1, \ldots, \boldsymbol{y}_m^1\}$ from the vectors $\{\boldsymbol{z}_1^0, \boldsymbol{z}_2^0, \boldsymbol{z}_3^0, \ldots, \boldsymbol{z}_m^0\}$ and they will span an ellipsoid of the same volume as $Df(\boldsymbol{x}_0)S$. Next apply the Jacobian $Df(\boldsymbol{x}_1)$ at the next orbit point, and reorthogonalize the vectors

$$\boldsymbol{z}_1^1 = Df(\boldsymbol{x}_1)\boldsymbol{y}_1^1,\ \boldsymbol{z}_2^1 = Df(\boldsymbol{x}_1)\boldsymbol{y}_2^1,\ \cdots,\ \boldsymbol{z}_m^1 = Df(\boldsymbol{x}_1)\boldsymbol{y}_m^1 \tag{2.13}$$

to produce a new orthogonal set $\{\boldsymbol{y}_1^2, \boldsymbol{y}_2^2, \boldsymbol{y}_3^2, \ldots, \boldsymbol{y}_m^2\}$. Repeat this process n times to produce a final set $\{\boldsymbol{y}_1^n, \boldsymbol{y}_2^n, \boldsymbol{y}_3^n, \ldots, \boldsymbol{y}_m^n\}$ of vectors which approximate the semi-major axes of the elliposid J_nS.

The total expansion r_i^n in the ith direction after n iterations is approximated by the length of the vector $\boldsymbol{y}_i^n$. Thus $||\boldsymbol{y}_i^n||^{\frac{1}{n}}$ is the approximation to the i$^{\text{th}}$ largest Lyapunov number after n iterations. To eliminate the problem of extremely large and small numbers, this algorithm should be amended to normalize the orthogonal basis at each step. Since $r_i^n \approx ||\boldsymbol{y}_i^n||||\boldsymbol{y}_i^{n-1}|| \cdots ||\boldsymbol{y}_i^1||$, the expression

$$\frac{\ln ||\boldsymbol{y}_i^n|| + \cdots + \ln ||\boldsymbol{y}_i^1||}{n}$$

can be considered as a convenient estimate of the ith largest Lyapunov exponent after n steps.

In the previous discussion we introduced the notion of chaotic orbit of maps and described procedures used to calculate certain characteristics of chaotic orbits. Now we introduce the concept of a "chaotic attractor". For this we define the following:

Let f be a map on R^m and let $\boldsymbol{x}_0$ be an initial condition. Then the **forward limit(or ω-limit) set** of the orbit $\{f^n(\boldsymbol{x}_0)\}_{n\in N}$ is the set

$$\omega(\boldsymbol{x}_0) = \{\boldsymbol{x} : \text{for all } p \text{ and } \epsilon \text{ there exists } n > p \text{ such that } |f^n(\boldsymbol{x}_0) - \boldsymbol{x}| < \epsilon\}$$

The definition of forward limit set of an orbit is the set of points to which the orbit returns arbitrarily close, infinitely often. Fixed ponts and periodic points are typical examples of forward limit sets.

Let f be a map and $\boldsymbol{x}_0$, $\boldsymbol{x}_1$ be initial conditons. Then orbit $\{f^n(\boldsymbol{x}_1)\}_{n\in N}$ of $\boldsymbol{x}_1$ under a map f is said to be **attracted** to the ω-limit set $\omega(\boldsymbol{x}_0)$ if $\omega(\boldsymbol{x}_1)$ is contained in $\omega(\boldsymbol{x}_0)$. The forward limit set $\omega(\boldsymbol{x}_0)$ of a chaotic orbit $\{f^n(\boldsymbol{x}_0)\}_{n\in N}$ is said to be a **chaotic set** if $\boldsymbol{x}_0 \in \omega(\boldsymbol{x}_0)$. An **attractor** is a forward limit set which attracts a set of initial values that has nonzero measure. A **chaotic attractor** is defined as a chaotic set that is also an attractor. That is, if the forward limit set of an attracting chaotic orbit contains the orbit itself, then the attractor is a chaotic attractor. The two important aspects of a chaotic attractor are that it contains a chaotic orbit and it attracts a set of initial values that has nonzero measure. The requirement that the defining orbit be in its own forward limit set ensures that a chaotic set has a dense orbit.

2.5 Differential equations

A differential equation expresses the rate of change of the current state as a function of the current state itself. Most physical laws that have been successful in the study of dynamically changing quantities are expressed in the form of differential equations. Ordinary differential equations are differential equations whose solutions are functions of one independent variable. As already mentioned in the beginning [sec.(2.1)], there are two types of differential equations, viz. autonomous and non-autonomous differential equations. Autonomous differential equations directly capture the spirit of a deterministic dynamical system, in which the law for the future is written only in terms of the present state. However, the distinction is artificial as any non-autonomous differential equations can be transformed into an autonomous differential equation at the expense of one more variable, equivalent to time. We shall now define what we mean by the so-called **flow** of a differential equation.

The **flow** of an autonomous differential equation is the set of all functions in time with initial values which are solutions of the differential equation. We use the notation $F_t(\boldsymbol{x}_0)$ or $F(t, \boldsymbol{x}_0)$ to denote the value at time t of the solution with initial value $\boldsymbol{x}_0$.

When a map is well defined, it will reveal unequivocally what would happen for all future times. With differential equations there are a few technicalities to be considered. First, solutions to an initial value problem may blow up (diverge) in finite time and so it may not exist for all time. It is possible, both for differential equations and maps, for solutions to tend to infinity, but exist for all time in the process. However, blow up in finite time is different and there is no analogous behavior for continuous maps. Second, without any restrictions on the differential equation, an initial value problem may have more than one solution. This is against the concept of determinism. A good model should specify the future unambiquously, given the rule and the present state and this in fact require us to put some restriction on the differential equations. Third, the utility of a model to give information about the dynamical process depends on the fact that the solution of the initial value problem does not depend too sensitively on the initial condition, at least at short time scales. In particular, for a fixed differential equation and two different initial values, we would like to know that the closer the two initial values are, the closer the solutions are for small t. This is what we mean by continuous dependence on the initial conditions. For large t they may diverge toward opposite corners of the phase space. Sensitivity at large t is called **sensitive dependence on initial conditions.**

Except for blow up in finite time, all other problems can be eliminated under mild restrictions on the differential equation. We now present theorems on the existence, uniqueness and continuous dependence on initial conditions and their proof can be found in standard texts on differential equations. The following theorem gives sufficient conditions for differential equations to possess unique solutions.

If in the m-dimensional system of first-order ordinary differential equations $\frac{d\boldsymbol{x}}{dt} = f(\boldsymbol{x})$ *both* f *and its first partial derivatives are continuous on an open set* U*, then for any real number* t_0 *and real vector* $\boldsymbol{x}_0$*, there is an open interval containing* t_0 *on which there exists a unique solution safisfying the initial condition* $\boldsymbol{x}(t_0) = \boldsymbol{x}_0$*.*

A function f on R^m is said to be **Lipschitz** on an open set U in R^m if there exists a constant L, called Lipschitz constant for f, such that

$$|f(\boldsymbol{x}) - f(\boldsymbol{y})| \leq L\,|\boldsymbol{x} - \boldsymbol{y}|$$

for all $\boldsymbol{x}$, $\boldsymbol{y}$ in U. If f has bounded first order partial derivatives in U, then f is Lipschitz. If a function f is Lipschitz with Lipschitz constant L, then two neighboring solutions to the same differential equation $\frac{d\boldsymbol{x}}{dt} = f(\boldsymbol{x})$ can separate from each other at a rate no greater than e^{Lt}. This is the basis for continuity of the flow as a function of the initial condition.

If f *is a function defined on the open set* U *in* R^m *with Lipschitz constant* L *in the variables* $\boldsymbol{x}$ *on* U*, and* $\boldsymbol{x}(t)$ *and* $\boldsymbol{y}(t)$ *are solutions of the differential equation* $\frac{d\boldsymbol{x}}{dt} = f(\boldsymbol{x})$ *with* $[t_0, t_1]$*, subset of domains of both solutions, then*

$$|\boldsymbol{x}(t) - \boldsymbol{y}(t)| \leq |\boldsymbol{x}(t_0) - \boldsymbol{y}(t_0)|e^{L(t-t_0)}$$

for $t \in [t_0, t_1]$*.*

A constant solution of the autonomous differential equation $\frac{d\boldsymbol{x}}{dt} = f(\boldsymbol{x})$ is called an **equilibrium** of the equation. An equilibrium solution is called **attracting** if the trajectories of nearby initial conditions coverge to it and it is said to be **repelling** if the solutions through nearby initial conditions diverge from it. For differential equations the solution can be an equilibrium or other more complex entities. A solution $F(t, \boldsymbol{x}_0)$ of the differential equation $\frac{d\boldsymbol{x}}{dt} = f(\boldsymbol{x})$ which is not an equilibrium is said to be a **periodic** orbit or **cycle** if there exits $T > 0$ such that $F(t + T, \boldsymbol{x}_0) = F(t, \boldsymbol{x}_0)$ and the smallest such number is called period of the orbit.

An equilibrium point $\boldsymbol{x}$ is said to be **stable** or **Lyapunov stable** if every initial point $\boldsymbol{x}_0$ very close to $\boldsymbol{x}$ has the property that the solution $F(t, \boldsymbol{x}_0)$ stays close to $\boldsymbol{x}$ for $t \geq 0$. That is, for any neighborhood N of $\boldsymbol{x}$ there exists a neighborhood M of $\boldsymbol{x}$, contained in N, such that for each initial point $\boldsymbol{x}_0$ in M, the solution $F(t, \boldsymbol{x}_0)$ is in N for all $t \geq 0$. An equilibrium is said to be unstable if it is not stable. Also, a stable and attracting equilibrium is said to be **asymptotically stable**. And it is said to be **globally asymptotically stable** if it is asymptotically stable and all initial values converge to the equilibrium. It is easy to describe the asymptotic behavior (ω-limit set) of any bounded orbit of an autonomous differential equation on the real line.

All solutions of the scalar differential equation $\frac{dx}{dt} = f(x)$ *for linear* $f(x)$ *are either monotonic increasing or monotonic decreasing as a function of time t. If the orbit* $F(t, x_0), t \geq 0, x_0 \in \mathrm{R}$ *is bounded then* $\omega(x_0)$ *consists solely of an equilibrium.*

Unlike linear systems, most nonlinear systems of ordinary differential equations can not be solved explicitly, meaning that the solutions can not be found through an analytic calculation in closed form. But much of the stability analysis for linear systems carries over to the study of equilibria of nonlinear systems. While a linear system either has only one equilibrium or has an entire line (or higher-dimensional subspace) of equilibrium, a nonlinear system can have many isolated equilibria. In order to determine the stability of an equilibrium $\boldsymbol{x}$ of

$$\frac{d\boldsymbol{x}}{dt} = f(\boldsymbol{x}), \tag{2.14}$$

we use the linear map that best approximates f at $\boldsymbol{x}$ and it is given by $f(\boldsymbol{x}+\boldsymbol{\eta}) \approx Df(\boldsymbol{x})\boldsymbol{\eta}$ for very small vector $\boldsymbol{\eta}$ where $Df(\boldsymbol{x})$ is the Jacobian matrix of partial derivatives evaluated at $\boldsymbol{x}$. If $y(t) = F(t, \boldsymbol{x} + \boldsymbol{\eta})$ from an initial value $\boldsymbol{x} + \boldsymbol{\eta}$ close to the equilibrium $\boldsymbol{x}$, then $z(t) = \boldsymbol{y}(t) - \boldsymbol{x}(t)$ satisfies

$$\frac{d\boldsymbol{x}(t)}{dt} = \frac{d\boldsymbol{y}(t)}{dt} = f(\boldsymbol{z}(t) + \boldsymbol{x}) \approx Df(\boldsymbol{x})\boldsymbol{z}(t) \tag{2.15}$$

at least for short times. The solutions of (2.14) near $\boldsymbol{x}_0$ move toward or away from equilibrium like the solutions of (2.15) and the behavior of the latter depends on the eigen values of $Df(\boldsymbol{x}_0)$. If the real parts of eigen values of $Df(\boldsymbol{x}_0)$ are all different from zero, the linear part $Df(\boldsymbol{x}_0)$ completely determines the stability of the equilibrium $\boldsymbol{x}_0$.

An equilibrium $\boldsymbol{x}_0$ of (2.14) is called **hyperbolic** if all the eigen values of $Df(\boldsymbol{x}_0)$ have real part different from zero.

When all eigen values of $Df(\boldsymbol{x}_0)$ have non-positive real parts and there is at least one eigen value with zero real part, then higher-order terms must be taken into account to determine the stability; that is, just the $Df(\boldsymbol{x}_0)$ value is not sufficient. If the real part of each eigen value is strictly negative, then the equilibrium is asymptotically stable and if at least one of the eigen values has strictly positive real part, then the equilibrium point will be unstable.

For autonomous differential equations on the real line, solutions that are bounded will converge to an equilibrium and for autonomous differential equations in the plane, a new limiting behavior is possible: solutions that are bounded may instead converge to periodic orbits (or cycles). An ω-limit set of a two-dimensional autonomous equation must be one of the following: (a) a set of equilibria; (b) a periodic point; (c) a set containing only equilibria and connecting arcs. However, nothing more radical can happen for solutions of autonomous differential equations in the plane. The topological rule about plane geometry that enforces this fact is the Jordan Curve Theorem. This matter is best described in the following Poincaré-Bendixson Theorem.

If f is a smooth vector function of the plane for which the equilibria of (2.14) are isolated and if the forward orbit $F(t, \boldsymbol{x}_0), t \geq 0$ is bounded, then either

1. $\omega(\boldsymbol{x}_0)$ is an equilibrium, or

2. $\omega(\boldsymbol{x}_0)$ is a periodic orbit, or

3. for each $\boldsymbol{x} \in \omega(\boldsymbol{x}_0)$, the limit sets $\alpha(\boldsymbol{x})$ and $\omega(\boldsymbol{x})$ are equilibria, where $\alpha(\boldsymbol{x})$ is the backward limit set of the orbit.

Steady states (equilibria) and periodic orbits are the two simplest forms of behavior for discrete and continuous dynamical systems. None of the above three types of ω-limit sets can be a chaotic set. Thus, we can conclude that for autonomous differential equations, chaos can occur only in dimensions higher than two. However, there can be chaos in one-dimensional maps, and for invertible maps it can occur in dimensions two and larger.

2.6 Lyapunov numbers and exponents of flows

Now we extend the idea of Lyapunov exponents (and numbers) of maps to flows (differential equations). In the case of maps, given a point, we imagine a sphere of initial conditions of infinitesimal radius evolving into an ellipse as the map is iterated. The average rate per iteration of the longest orthogonal axis of the ellipse is taken as the first Lyapunov number of the orbit, and its natural logarithm is called as the Lyapunov exponent. A positive Lyapunov exponent signifies growth along that direction, and so exponential divergence of nearby trajectories. The existence of a local expanding direction along an orbit is the hallmark of a chaotic orbit. In flows of differential equations, the concept is the same, once we replace the discrete iteration of the map with the continuous flow of a differenital equation. The flow $F_T(\boldsymbol{x}_0)$ is defined to be the point at which the orbit with initial condition $\boldsymbol{x}_0$ arrives after T time units. We define the Lyapunov numbers (and exponents) for flows of differential equation as the Lyapunov numbers (and exponents) of the associated time-T map $F_T(\boldsymbol{x}_0)$ when $T = 1$.

For computing the Lyapunov exponents, we begin with a tiny sphere $S_r(\boldsymbol{x}_0)$ of initial conditions around some point $\boldsymbol{x}_0$, and imagine the evolution of the sphere as the initial conditions follow the flow of the differential equation. We then compute the Jacobian matrix $DF_1(\boldsymbol{x})$ of derivatives of the $T = 1$ map of $F_T(\boldsymbol{x})$ with respect to the initial value $\boldsymbol{x}$. Then using the procedure explained in sec.2.4, we can compute the largest Lyapunov exponent. For computing the Lyapunov exponent from a time series a number of important considerations have to be taken care of. We will explain these in detail at the appropriate places in the coming chapters. With a brief description about dissipative dynamical systems, we shall conclude this chapter.

Since $\{F_t(\boldsymbol{x}) : t \in \mathrm{R}\}$ is the solution of $\frac{d\boldsymbol{x}}{dt} = f(\boldsymbol{x})$ with initial value $\boldsymbol{x}$, we have

$$\frac{d}{dt}F_t(\boldsymbol{x}) = f(F_t(\boldsymbol{x})) \tag{2.16}$$

This equation has two variables, time t and the initial value $\boldsymbol{x} \in \mathrm{R}^m$. Differentiating with respect to $\boldsymbol{x}$, we get

$$\frac{d}{dt}DF_t(\boldsymbol{x}) = Df(F_t(\boldsymbol{x}))\,DF_t(\boldsymbol{x}) \tag{2.17}$$

This equation is called the **variational equation** of the differential equation, for on solution it gives the derivative matrix of F_t and so it reveals how F_t acts under small variations in the initial value $\boldsymbol{x}$. Let $J_t = DF_t(\boldsymbol{x})$ be the Jacobian of the time t map evaluated at initial value $\boldsymbol{x}$ and $A(t) = Df(F_t(\boldsymbol{x}))$ be the matrix of partial derivatives of f evaluated along the solution. Then the variational equation (2.17) becomes

$$\frac{dJ_t}{dt} = A(t)J_t \tag{2.18}$$

To get the above equation we fixed the initial condition $\boldsymbol{x}$ and hence to obtain a unique solution we need to consider an initial condition $J_0 = I$, where I is the identity matrix. The variational equation (2.17) is a linear equation, even when the original equation is nonlinear. An important fact about the Jacobian matrix $J_T = DF_T(\boldsymbol{x})$ of the time T map evaluated at $\boldsymbol{x}$ is that it maps small variations tangent to the orbit at time 0 to small variations tangent to the orbit at time T. That is,

$$DF_T(\boldsymbol{x})\,f(\boldsymbol{x}) = f(F_T(\boldsymbol{x})) \tag{2.19}$$

This defines the direction of the orbit at each instant as time progresses. This can be seen as follows: applying the variational equation (2.17) to the vector $f(\boldsymbol{x})$, we get

$$\frac{d}{dt}DF_t(\boldsymbol{x})f(\boldsymbol{x}) = Df(F_t(\boldsymbol{x}))\,DF_t(\boldsymbol{x})f(\boldsymbol{x}) \tag{2.20}$$

Taking $\boldsymbol{y} = DF_t(\boldsymbol{x})f(\boldsymbol{x})$, we observe that $\boldsymbol{y}(t)$ satisfies the initial value problem,

$$\begin{aligned} \frac{d\boldsymbol{y}}{dt} &= Df(F_t(\boldsymbol{x}))\boldsymbol{y} \\ \boldsymbol{y}(0) &= f(\boldsymbol{x}) \end{aligned} \tag{2.21}$$

Note that on differentiating (2.16) with respect to t, we get

$$\begin{aligned} \frac{d^2}{dt^2}F_t(\boldsymbol{x}) &= Df(F_t(\boldsymbol{x}))\frac{d}{dt}F_t(\boldsymbol{x}) \\ \frac{d}{dt}f(F_t(\boldsymbol{x})) &= Df(F_t(\boldsymbol{x}))f(F_t(\boldsymbol{x})) \end{aligned} \tag{2.22}$$

and $f(F_t(\boldsymbol{x}) = f(\boldsymbol{x})$ at time 0. Since $\boldsymbol{y}$ and $f(F_t(\boldsymbol{x})$ satisfy the same initial value problem, they are equal. The important consequence of (2.19) is that a bounded orbit of an autonomous flow either has one Lyapunov exponent equal to zero, or else it has an equilibrium in its ω-limit set. When the second possibility is excluded, we can conclude that the Lyapunov exponent in the direction tangent to the orbit is zero in the case of autonomous differential equations.

The change in volume due to the flow can be found with the help of a formula due to Liouville. Let $\Delta(t) = \det J_t$ where J_t is as in (2.18). Liouville's formula [Hartman, 1964] [59] says that $\Delta(t)$ satisfies the differential equation with the initial conditon

$$\begin{aligned} \Delta_t' &= \mathrm{Tr}(A(t))\Delta_t \\ \Delta_0 &= \det J_0 = 1 \end{aligned} \tag{2.23}$$

where $\mathrm{Tr}(A(t))$ denotes the trace of the matrix $A(t)$. From (2.23) it follows that

$$\det J_t = \exp\left(\int_0^t \mathrm{Tr}(A(t))dt\right) \tag{2.24}$$

We now define the class of dissipative systems using the above relation.

A system of differential equations is said to be **dissipative** if its time-T map decreases volume for all $T > 0$. If $\mathrm{Tr}(A(t)) < 0$ for all t, then system will be dissipative.

Using the definition of Lyapunov exponent for flows, we can define chaotic orbits of flows of differential equation as follows:

An aperiodic and bounded orbit $F_t(\boldsymbol{x}_0)$ with initial point $\boldsymbol{x}_0 \in \mathrm{R}^m$ whcih does not consists solely of equilibrium points of the differential equation $\frac{d}{dt}\boldsymbol{x}(t) = f(\boldsymbol{x}(t))$ is said to be a **chaotic orbit of the flow** if the orbit has at least one positive Lyapunov exponent.

In the following section, we introduce another very important tool to characterize the attractor of a dynamical system.One of the important aspects in analysing a time series using the tools of nonlinear dynamic methods and chaos theory is the characterization of the attractor on which the system finally resides. We introduce the required notion from a historical perspective.

2.7 Dimensions

The minimum number of quantities required to specify a point in space is of great importance in almost all fields of science. For a regular object (in Euclidean space) there is no ambiguity in specifying a point in space. However, when "fractal", objects like the Cantor dust or the Peano curves appeared, many mathematicians described these objects as "monsters" or "pathological objects". After the work of [Mandelbrot, 1977] [86] (who also introduced the word "fractal"), fractals became important in science mostly in studies of nonlinear dynamical systems. The notion of dimension specifies the number of quantities required to uniquely describe a point in space. We can have different types of dimensions and using the concept of dimension of an object we can determine the topological and dynamical properties of phase space orbits.

2.7.1 Topological dimension

Of all the various dimensions the Topological dimension D_T is the most obvious. Roughly speaking, D_T is the "number of different perpendicular directions" in space. In a formal way, we define D_T as the number of coordinates needed to specify a position uniquely in space. The modern definition of D_T is based on a recursive method and is formulated by D. Urysohn and K. Menger [Gosztonyi, 1976] [51].

A set M is said to have a topological dimension $D_T = n$ at a point p$\in$ M if every neighborhood U_p of p contains a neighborhood V_p of p, whose border $B(V_p)$ is of maximal $n-1$ dimension. The topological dimension of the empty set is taken as -1.

It is clear that the topological dimension is always an integer and in normal case its value lies in the range $0 \leq D_T \leq 3$ in the Euclidean space.

2.7.2 Phase space dimension

This dimension is mostly used in physics and is a basic property of a dynamical system. Loosely speaking it is the number of degrees of freedom of a physical system (dynamical system). Formally we define it as

The phase space dimension D_{PH} is the number of free coordinates in a dynamical system.

We can see that D_{PH} is always an integer in the range $0 \leq D_{PH} \leq \infty$. We now introduce a very abstract but important concept of dimension.

2.7.3 Hausdorff dimension

There are different ways of defining the Hausdorff dimension for a set. Here we follow [Zeitler, 1993] [141] for the definition of the Hausdorff dimension:

Let M be a metric space with metric e and U $\subset$ M, then diameter of U denoted by

$|U|$ is defined as

$$|U| = sup\{e(x, y)|x, y \in U\}. \tag{2.25}$$

A collection $\{U_i\}$ is called a cover for a subset E of M if $E \subset \cup U_i$. Then the Hausdorff measure of the set E is denoted by

$$H^d(E) = \lim_{r \to 0} H^d_{2r}(E) \tag{2.26}$$

where

$$H^d_{2r}(E) = inf \left\{ \sum_i |U^d_i| \right\} \tag{2.27}$$

and $0 < |U_i| \leq 2r$ and d is a parameter. *The Hausdorff-Besicovitch theorem says that for a given bounded set* $E \subset M$ *if there exists a value* $d = D$ *such that* $0 < H^D(E) < +\infty$ *then* $H^d(E) = +\infty$ *for all* $d < D$ *and* $H^d(E) = 0$ *for all* $d > D$. The estimate of D so obtained from the Hausdorff- Besicovitch theorem is called the Hausdorff - Besicovitch Dimension of E or simply Haudorff Dimension D_H of the set E. It is easy to observe that D_H can take any non-negative real number including infinity. As an example of the calculation of Hausdorff dimension, we consider the computation of dimension of Cantor set (or Cantor's dust) in the following:

The Cantor's dust is constructed from the unit interval $\boldsymbol{I} = [0,1]$. Divide $\boldsymbol{I}$ into three equal sub-intervals and remove the middle sub-interval. Let C_1 be the union of the remaining sub-intervals. Again divide each sub-interval into three equal sub-intervals and remove their respective middle sub-intervals. Let C_2 be the union of the remaining 4 sub-intervals. In the rth step we get $C_r = \cup_{i=1}^{2^r} \boldsymbol{I_i}$ where each $\boldsymbol{I_i}$ is a sub-interval of the unit interval $\boldsymbol{I}$ of length 3^{-r}. Contiune this process indefinitely and then the Cantor's dust is defined as

$$C = \cap_{i=1}^{\infty} C_i = \lim_{i \to \infty} C_i \tag{2.28}$$

Since the length of each interval I_i is 3^{-r} we get the following relation:

$$\sum_{i=1}^{2^r} |I_i|^d = 2^r (3^{-r})^d = (\frac{2}{3^d})^r \tag{2.29}$$

Now as the radius $\epsilon \rightarrow 0$, r tends to ∞ and so the above limit tends to a finite non-zero number only if $2 = 3^d$. This gives the value $d = \frac{\ln 2}{\ln 3} = 0.6309\cdots$. We observe that the dimension of Cantor's dust is a fraction; such objects are called *fractals*.

2.8 Fractal dimension

The estimates of topological dimension and phase space dimension always give integer values, but the Hausdorff dimension can also be a fraction. In this respect, the Hausdorff dimension is more general in nature than the other dimensions. If the estimate of the very dimension of an object is a fraction, the estimate is called the fractal dimension and the object is called a fractal. One limitation of Hausdorff dimension is that it is not very useful in practical applications as computation of this quantity is very time consuming and this motivates us to find other easily measurable dimension estimates.

2.8.1 Capacity dimension

In the computation of Hausdorff dimension, the sets U_i for covering of E are arbitrary. Assume that the sets U_i are spheres with a fixed radius ϵ, then the expression (2.26) takes the form

$$H^d_\epsilon(E) = N(\epsilon)\,\epsilon^d, \tag{2.30}$$

where $N(\epsilon)$ is the number of spheres needed to cover the set. From the above equation we get

$$N(\epsilon) = H^d_\epsilon(E)\epsilon^{-d} \tag{2.31}$$

In the limit as $\epsilon \rightarrow 0$ we get the following relation

$$N(\epsilon) \approx K\epsilon^{-d}, \tag{2.32}$$

where $K = H^d$. Using this relation we define the capacity dimension(or box counting dimension) as follows

Let $N(\epsilon)$ *be the number of n-dimensional boxes with length* ϵ *needed to cover the set E, then the capacity dimension* D_o *or box counting dimension* D_B *of E is defined as*

$$D_o(E) = \lim_{\epsilon \to 0} \frac{\ln N(\epsilon)}{\ln \frac{1}{\epsilon}}. \tag{2.33}$$

In general, the box counting dimension is larger than the Hausdorff dimension, but in most cases both estimates are same. While calculating the box counting dimension, cover the structure with a grid of n-dimensional ($n = D_P$) boxes of sidelength ϵ. Count the number of boxes that contain at least one point of the structure which gives the value of $N(\epsilon)$. This has to be done for several values of ϵ, then the slope of the function $\log N(\epsilon)$ vs. $\log(\epsilon)$ gives the value of D_o. This estimate of a structure reveals only the geometrical feature of the structure and no dynamical characteristics and it does not take into account the number of points contained in each box, since only the number of visited is counted. That is, all boxes, whether they contains only one point or more points, are given equal importance. This is a limitation of capacity dimension.

2.8.2 Information dimension

Here cover the set E with n-dimensional boxes (with $n = D_P$) of side length ϵ then compute the probability p_i that a point falls in the ith box given by $p_i = \frac{N_i}{N}$ where N is the total number of points in E and N_i is the number of points in the ith box. The information dimension can now be defined analogously as follows:

Let $N(\epsilon)$ *be the number of n-dimensional boxes of sidelength* ϵ *needed to cover a set E and* p_i *be the probability that a point of the set E falls in the ith box, then the information dimension denoted by* D_1 *of E is defined as*

$$D_1(E) = \lim_{\epsilon \to 0} \frac{-\sum_{i=1}^{N(\epsilon)} p_i \log p_i}{\log \frac{1}{\epsilon}} \tag{2.34}$$

The information dimension can be interpreted as " information required to specify an initial condition or a point of the set" [Farmer, 1982][45]. Information dimension is very costly in computaion and is rarely used in practice mainly beacause there is another dimension estimate which can be estimated comparatively with less cost.

2.8.3 Correlation dimension

The correlation dimension was first introduced by [Grassberger and Procaccia, 1983] [56] and is based on the correlation between points of a given set. Let N be the number of points $\{\boldsymbol{X}_i\}_{i=1}^{N}$, then the *correlation integral* is defined as

$$C(\epsilon) = \lim_{N\to\infty} \frac{1}{N^2} \sum_{i,j=1}^{N} \theta(\epsilon - |\boldsymbol{X}_i - \boldsymbol{X}_j) \tag{2.35}$$

where θ(x) is the Heaviside function defined by $\theta(x) = 0 \leftrightarrow x \leq 0$ and $\theta(x) = 1 \leftrightarrow x > 0$. The correlation integral counts all pairs of points which are at a separation smaller than ϵ. For small values of ϵ, C(ϵ) behaves as a powerlaw as

$$C(\epsilon) \approx R^{D_2} \tag{2.36}$$

Using this relation we can define the correlation dimension as

Let C(r) be the correlation integral of the points $\{\boldsymbol{X}_i\}_{i=1}^{N}$ of a set E for a distance ϵ, the correlation dimension D_2 is given by

$$D_2(E) = \lim_{\epsilon\to 0} \frac{log\, C(\epsilon)}{log\, \epsilon} \tag{2.37}$$

By definition, C(ϵ) is the probability that two points lie in the same box. In practice, C(ϵ) is calculated for a range of values of ϵ and plot of logC(ϵ) vs. logϵ is drawn; the slope yields the value of correlation dimension of the set. In most cases, a direct application of this formula will not give an optimal value of correlation dimension. Depending on the given data, certain parameters have to be calculated to find an optimal value of correlation dimension. We will describe these parameters at the appropriate places when we apply this formula. The different dimensions viz. capacity dimension, information dimension and correlation dimension can be obtained from a single formula.

2.8.4 Generalized fractal dimensions

The concept of fractal dimension can be generalized by means of the definition of probability p_i that a point is in the ith box introduced in (2.8.2). We give the generalized dimension as it is given by [Hentschel and Procaccia, 1983] [62].

Let $N(\epsilon)$ be the number of n-dimensional boxes of side length ϵ needed to cover a set E and p_i be the probability that a point of the set E falls in the ith box, then the q-th generalized fractal dimension denoted by D_q of E is defined as

$$D_q(E) = \frac{1}{1-q} \lim_{\epsilon \to 0} \frac{\log \sum_{i=1}^{N(\epsilon)} p_i{}^q}{\log \epsilon} \tag{2.38}$$

It can be shown that if $s < t$ then $D_t < D_s$. When q=0, then the sum in (2.38) becomes $N(\epsilon)$ and so we get the capacity dimension D_o. If q=1, taking the limit as $q \to 1$ gives the information dimension D_1. If q=2, the expression $\sum_{i=1}^{N(\epsilon)} p_i^2$ gives the probability that two points of a randomly chosen pair lie in the same box of side length ϵ. When $\epsilon \to 0$, it gives the probability that these points are at most ϵ apart and hence is the same as the correlation integral in (2.37). Thus, when q=2, we get the correlation dimension. The generalized dimension can be calculated for all integer values from $-\infty$ to $+\infty$. But for application purposes most of these dimensions are not useful. If the points are weighted such that, boxes that are visited more often than others contribute more, all dimensions for q<0 have to be ignored. The same reason excludes high values of q, if sparsely filled boxes are not to be ignored completely. In general, values for q between 0 and 4 are taken. When q=0, we get the capacity dimension, which can not be applied to fractals having non-zero measure (called *fat fractals*) refer (Eykholt *et al.*, 1986)[43]; counting boxes is very costly for computations which disqualifies q=1 and q>2. Finally, we are left with the correlation dimension D_2 for which suitable algorithms are available and which is the most popular dimension. This does not mean that computation of correlation dimension is easy. The point is that, compared to the computation of other dimension estimates, its computation is easy. For a suitable and reliable estimation of correlation dimension, we have to consider a number of other factors like choosing a proper time delay and Theiler's window which we explain at the proper places.

CHAPTER 3

Stokesian Dynamics

3.1 Rheology of suspensions

Suspensions are generally classified into three categories: solid particles in a fluid medium, liquid droplets in a liquid medium (emulsion) and gas in a liquid medium (foam). In this analysis, we refer to solid particles dispersed in a liquid medium. Examples of such suspension are industrial slurries, paints, cements, ceramics, printing inks, different types of processed foods etc. The flow behavior of these suspensions is often complex and their rheological properties are very different from those of the suspending fluid. The complexity arises from the subtle nature of interparticle interactions mediated by the fluid medium. The strong interaction between flow and the suspended phase has important effects on the macroscopic, optical, mechanical and electrical properties. In order to obtain the requisite macroscopic properties of a product obtained from the processing of suspensions, the factors which control suspension rheology must be understood. Such studies provide an opportunity for innovative manipulation of material and flow properties through the understanding and control of the relation between flow and micro-structure. Experimental studies of suspension rheology are prone to many artefacts and instrumental errors which are difficult to avoid. Numerical simulations have many advantages over experimental studies. In numerical simulation, defects in the experimental studies arising from errors in the measurement technique and unavoidable defects in the material or flow conditions can be eliminated. They also provide the flexibility to exclusively incorporate some effects and study their influence. The availability of fast computers has enabled realistic numerical simulations which can be used for the interpretation of experimental observations and to develop deeper insight into the suspension rheology. The objective of any numerical simulation is to calculate macroscopic rheological properties from microscopic structural mechanics.

Determination of the macroscopic properties of suspensions from a detailed fluid mechanics around the particles originated from Einstein's celebrated work [Einstein, 1906][40], in which he considered the dilute limit where particle interactions are absent at zero particle Reynolds number. Assuming that hydrodynamic interactions between particles are absent, Einstein derived an expression for the effective viscosity η_s, of dilute suspensions as

$$\eta_s = \eta(1 + 2.5\,\phi) \tag{3.1}$$

where η is the viscosity of pure fluid and ϕ is the volume fraction of solid particles. The main finding of Einstein was that the addition of rigid particles to a Newtonian fluid results in a suspension of enhanced viscosity. The above equation is valid in very dilute systems with $\phi < 0.02$, where the relative (with respect to particle size) distance between particles is large. As the concentration increases the velocity disturbance of one particle will influence the velocities of neighboring particles. Accounting for binary interactions, Batchelor and Green [15] derived the $O(\phi^2)$ contribution to the viscosity, ϕ being the particle volume fraction as

$$\eta_s = \eta(1 + 2.5\,\phi + 6.2\,\phi^2) \tag{3.2}$$

Even the above equation is valid only for $\phi < 0.1$. But, in practical industrial problems, we have to deal with suspensions having larger concentrations, where more than two particles can interact simultaneouly. Extending dilute suspension analysis to higher concentrations poses at least two difficulties: determination of many body hydrodynamic interactions and the determination of the spatial distributions of the particles called suspension microstructure. Due to these difficulties, determining the bulk stress analytically at higher concentrations has not been possible. In addition to many-body interactions, lubrication forces play a predominant role in determining the structure and dynamics of suspensions at high concentrations. The determination of many-body interactions at all particle separations is a computationally challenging problem.

3.2 Simulation method

Stokesian Dynamic simulations[Brady & Bossis, 1988][19] are presently considered to be an accurate method for computing the dynamics and rheological properties of suspensions. This technique has been used to solve a large number of problems on Brownian suspensions[Morris and Brady, 1996] [90], [Phung *et al.*,1996] [104], non-colloidal sheared suspensions [Brady and Bossis, 1985] [21], [Durlofsky and Brady, 1989] [38], flow through porous media [Durlofsky and Brady, 1987] [37] and pressure driven flows [Nott and Brady, 1994] [94]. In most of the above studies, there was no direct effect of boundaries on the system, i.e. the properties were calculated for unbounded systems. In most practical situations, the flow is confined between boundary walls. Due to the great extent of the boundaries, the boundary effects become important in Stokes flow problems where the disturbances produced by the particles decay very slowly. The presence of a wall influences the local arrangement of the particles and hence the rheology. To incorporate boundary effects, expression for the interaction of particles with the plane boundaries are required.

For an accurate determination of the dynamics of suspended particles, and thereby the bulk properties of the suspension, the many-body hydrodynamic interactions between particles must be computed correctly. This is accomplished by the Stokesian Dynamics technique [Brady and Bossis, 1988] [19], which computes particle interactions as a sum of the far- and near-field hydrodynamic interactions in a consistent and efficient way. Brady *et al.*[1988] [20] developed a method for simulating an infinite suspension of hydrodynamically interacting particles, by periodically replicating a finite number of particles throughout space. The lattice summation is carried out using the method of Ewald [44], to accelerate the convergence.

Consider a system of N particles undergoing rigid body motion in a linear ambient field $(\mathbf{U}^{\infty} + \mathbf{\Omega}^{\infty} \times \mathbf{x} + \mathbf{E}^{\infty} . \mathbf{x})$, where $\mathbf{U}^{\infty}$, $\mathbf{\Omega}^{\infty}$ and $\mathbf{E}^{\infty}$ denote the velocity, vorticity and rate of strain of the ambient field, respectively. In this analysis, we have used some simplifications in order to understand the rheological properties of the suspensions. It is assumed that the flow is laminar and the fluid motion is so slow that the inertial forces are negligible and do not influence the dynamics of the system. The dimensionless number which determines the relative importance of inertial and viscous effects is the Reynolds number based on particle size given by

$$R_e = \frac{\rho U a}{\eta} \tag{3.3}$$

where ρ is the fluid density, η is the fluid viscosity, U is the characteristic velocity of particles and a is the particle size. When the motion of particles is very slow ($R_e << 1$), viscous forces dominate over the inertial forces and the flow is said to be in the creeping flow regime. The relevant governing equations in this case are the Stokes equations,

$$\nabla \boldsymbol{p} = \eta \nabla^2 \boldsymbol{u} \tag{3.4}$$

$$\nabla \cdot \boldsymbol{u} = 0 \tag{3.5}$$

where $\boldsymbol{u}$ and $\boldsymbol{p}$ are the velocity and pressure fields respectively, and η is the fluid viscosity.

Our second restriction is that the particles are large enough ($> 10\mu$m), that Brownian motion is negligibly small. The relative importance of Brownian motion is characterized by the Péclet number defined by

$$P_e = \frac{\dot{\gamma} a^2}{D_0} \tag{3.6}$$

where $\dot{\gamma}$ is the shear rate and $D_0 = \frac{kT}{6\pi\eta a}$ is the Stokes-Einstein diffusivity of an isolated particle of size a in a fluid of viscosity η.

The no-slip condition on the surface S_p of a particle requires that,

$$\mathbf{u} = \mathbf{U} + \mathbf{\Omega} \times \mathbf{x} \tag{3.7}$$

where $\mathbf{U}$ and $\mathbf{\Omega}$ denote the translational and rotational velocity of the particles, and $\mathbf{x}$ is the position vector of any point on the surface S_p relative to the center of the particle.

Another condition is that at points far away from the particle, the fluid motion is unaffected by the presence of the particles, i.e.,

$$\mathbf{u} = \mathbf{U}^\infty + \mathbf{\Omega}^\infty \times \mathbf{x} + \mathbf{E}^\infty . \mathbf{x} \qquad \text{as} \qquad \mathbf{x} \to \infty \tag{3.8}$$

Given the above boundary conditions and the imposed flow field, one would like to solve for the disturbance in the velocity and pressure fields due to the presence of particles, and thereby calculate the hydrodynamic force $\mathbf{F}$, torque $\mathbf{T}$ and stresslet $\mathbf{S}$, exerted by the fluid on the particles. Since the governing equations (Stokes equations) are linear in the fields $\mathbf{u}$ and $\mathbf{p}$, the solution can be treated as superposition of the following three independent motions:

1.Translation of the particle with a steady velocity $(\mathbf{U} - \mathbf{U}^\infty)$ through a quiescent fluid.

2.Rotation of the particle with a steady angular velocity $(\mathbf{\Omega} - \mathbf{\Omega}^\infty)$ in a quiescent fluid.

3.A fixed particle in a rate of strain field $\mathbf{E}^\infty . \mathbf{x}$.

The general solution for $\mathbf{F}$, $\mathbf{T}$ and $\mathbf{S}$ may be written by superposition in the matrix form

$$\begin{pmatrix} \mathbf{F} \\ \mathbf{T} \\ \mathbf{S} \end{pmatrix} = \eta \mathcal{R} \begin{pmatrix} \mathbf{U}^{\infty} - \mathbf{U} \\ \boldsymbol{\Omega}^{\infty} - \boldsymbol{\Omega} \\ \mathbf{E}^{\infty} \end{pmatrix} \tag{3.9}$$

where

$$\mathcal{R} = \begin{pmatrix} \mathbf{A} & \hat{\mathbf{B}} & \hat{\mathbf{G}} \\ \mathbf{B} & \mathbf{C} & \hat{\mathbf{H}} \\ \mathbf{G} & \mathbf{H} & \mathbf{M} \end{pmatrix} \tag{3.10}$$

is called the grand resistance matrix [Brenner and O'Neill, 1972][22]. **A**, **B** and **C** are second rank tensors, **G** and **H** are third rank tensors and **M** is a fourth rank tensor. The solution of the motion of the particle in response to prescribed forces and torques in a known ambient flow is the so called mobility problem. And it is given by

$$\begin{pmatrix} \mathbf{U}^{\infty} - \mathbf{U} \\ \boldsymbol{\Omega}^{\infty} - \boldsymbol{\Omega} \\ \mathbf{E}^{\infty} \end{pmatrix} = \eta^{-1} \mathcal{M} \begin{pmatrix} \mathbf{F} \\ \mathbf{T} \\ \mathbf{S} \end{pmatrix} \tag{3.11}$$

where

$$\mathcal{M} = \begin{pmatrix} \mathbf{a} & \hat{\mathbf{b}} & \hat{\mathbf{g}} \\ \mathbf{b} & \mathbf{c} & \hat{\mathbf{h}} \\ \mathbf{g} & \mathbf{h} & \mathbf{m} \end{pmatrix} \tag{3.12}$$

is called the grand mobility matrix. Both the grand resistance matrix and grand mobility matrix are symmetric and positive definite and they are related to each other [Kim and Karrila, 1991] [73]. Durlofsky *et al.*[1989] [38] claim that the mobility formulation is more accurate with widely spaced particles, but the resistance formulation is more accurate for closely spaced particles. If an N body mobility matrix is formed using pairwise additivity of velocities, it can not capture lubrication interactions besides lacking many body effects. [Durlofsky *et al.*, 1989] [38] removed these two discrepancies by formulating the problem in the following way: Inverting the mobility matrix yields a far-field approximation to the resistance matrix. Even though the mobility matrix only includes two-body mobility interactions, its inverse includes many body resistance interactions. The near-field lubrication interactions are then introduced in a pair wise additive manner, using the exact two-body resistance functions [Kim and Karrila, 1991] [73]. Thus the general method of Stokesian Dynamics [Brady & Bossis, 1988] [19] can be described in the following steps

* Formation of the grand mobility matrix by pairwise additivity.

* Inversion of the grand mobility matrix to get the far-field part of the grand resistance matrix

* Addition of lubrication resistances.

* Determination of particle velocities.

* Calculation of macroscopic properties.

For a detailed description of the above procedure the reader is referred to [Durlofsky *et al.*,1989] [38], [Brady *et al.*, 1988] [20] and [Brady and Bossis, 1988] [19].

As mentioned above, most studies that have employed Stokesian Dynamics have only investigated unbounded uniform shear, ignoring the effect of boundaries. In realistic situations, flow is set either by the motion of the confining boundaries or driven by a pressure gradient, and the resulting dynamics can be quite different from that of unbounded systems. The impermeable walls alter the microstructure (i.e. the local arrangement of particles) near them, thereby altering the bulk properties.

Durlofsky and Brady [1989] [38] were the first to incorporate the effect of plane boundaries in Stokesian Dynamics simulations. To incorporate the interaction of particles with the plane boundaries in the Stokesian Dynamics method walls are divided into near and far regions. They discretized the near regions into a number of patches (P) and the far region uses a simplified description of the integrated effect of the walls outside the discretized region. A uniform distribution of the force density was assumed on each patch and accounted for interactions between the suspended spheres and the patches. The interaction of spheres with wall patches were analogous to sphere-sphere interactions. They considered a periodically replicated system of N spheres between two parallel walls of infinite extent with shear applied translating the upper boundary with a constant velocity. The grand mobility matrix relating the translational and angular velocities U (of dimension 6N) of the N particles, the bulk rate of strain E (of dimension 5N) and the translational velocity V of the wall patches (of dimension 3P) is related to the forces and torques F of the paticles (of dimension 6N), the stresslets on the particles (of dimension 5N) and the force T exerted by the wall patches (of dimension 3P) is given by

$$\begin{pmatrix} U \\ -E \\ V \end{pmatrix} = \begin{pmatrix} M_{UF} & M_{US} & M_{UT} \\ M_{EF} & M_{ES} & M_{ET} \\ M_{VF} & M_{VS} & M_{VT} \end{pmatrix} \begin{pmatrix} F \\ S \\ T \end{pmatrix} + \begin{pmatrix} B_U \\ B_E \\ B_V \end{pmatrix} \tag{3.13}$$

The vectors B_U, B_E, B_V contain the integrated effect of the wall outside the discretized region as well as a portion of the effect of the wall patches. The sub-matrices M_{UF}, M_{US}, M_{EF}, and M_{ES} are components of the grand mobility matrix $\mathcal{M}$ (3.11) for a finite system spheres in an unbounded fluid. The matrices M_{UT}, M_{ET}, M_{VT}, M_{VF} and M_{VS} involve sphere-patch and patch-patch interactions. These interactions are derived from the integral representation of the Stokes flow equation, except that the force density over the surface of the patch is assumed constant and not expanded in moments. The different components of the vector B are determined by integrating the appropriate interaction functions from the boundary of the discretized region to infinity, multiplied by the appropriate force density. The force density on the wall outside the discretized region is assumed to be that which would exist in the absence of any particles. They argued that for homogeneous suspension this assumption is justified [Durlofsky & Brady, 1989][38] though it is not accurate for inhomogeneous suspensions due the long range nature of hydrodynamic interations. The mobility matrix in equation (3.13) is inverted which results in a resistance matrix which is then corrected for the lubrication forces arising from sphere-sphere and sphere-wall interactions. The wall effect arises because the actual force density on the boundaries, in the presence of a force-free sphere, differs from its value in the absence of the sphere and it will be correctly reproduced only when the discretized region becomes infinite. Increasing the size of the discretized region increases the size of the matrix in equation (3.13) and in effect it will increase the computational labour. Due to these limitations, they studied model problems involving a few spheres with finite number of wall discretizations. Given the velocities of the walls, the final set of equations was solved to calculate the velocities of the spheres and the forces on the walls. From the knowledge of the shear forces on the walls, they were able to calculate the relative viscosity of the suspension. However, they computed the interactions between spheres (or patches) far apart using a simplistic, mean-field approximation approach.

Brady *et al.*[1988] used a more accurate technique to compute the interactions between particles in different periodic cells. They used Ewald's re-summation technique [44] for periodic lattices in order to simulate unbounded flow, which Nott & Brady[1994] subsequently used to study the pressure driven flow of a suspension. Nott and Brady [94] incorporated the boundaries in Stokesian Dynamics simulations on the pressure driven flow of suspensions of rigid particles[94] and some of the spheres were designated as wall particles which were placed in a plane and forced to move at the same velocity, thus providing a "bumpy wall". The grand mobility matrix for all particle (interior as well as wall particles) relates the velocities to the forces and stresslets by

$$\begin{pmatrix} \mathbf{U} - < \mathbf{u} > \\ - < \mathbf{e} > \end{pmatrix} = \mathcal{M} \begin{pmatrix} \mathbf{F} \\ \mathbf{S} \end{pmatrix} \tag{3.14}$$

where

$$\mathcal{M} = \begin{pmatrix} M_{UF} & M_{US} \\ M_{EF} & M_{ES} \end{pmatrix}, \quad \mathbf{U} = \begin{pmatrix} U^s \\ U^w \end{pmatrix} \quad \text{and} \quad F = \begin{pmatrix} F^s \\ F^w \end{pmatrix} \tag{3.15}$$

Each sub-matrix in the grand mobility matrix $\mathcal{M}$ can be broken up into sphere-sphere, sphere-wall and wall-wall contributions as

$$M_{UF} = \begin{pmatrix} M_{UF}^{ss} & M_{UF}^{sw} \\ M_{UF}^{ws} & M_{UF}^{ww} \end{pmatrix} \tag{3.16}$$

and so on. In the above equations, the superscripts s and w on the velocities and forces indicate sphere and wall quantities, and the superscripts ss and sw on the mobilities indicate sphere-sphere and sphere-wall couplings. The moblility matrix is inverted and adjusted for lubrication in exactly the way one would do for an unbounded suspension, and the final resistance matrix after lubrication adjustment is given by

$$\mathcal{R} = \mathcal{M}^{-1} + \mathcal{R}_{2b} - \mathcal{R}_{2b}^{\infty} \tag{3.17}$$

where $\mathcal{R}_{2b}$ is the near-field two-body resistance tensor for all particle pairs and $\mathcal{R}_{2b}^{\infty}$ is the far-field part of $\mathcal{M}^{-1}$, which is subtracted to avoid double counting. The near-field resistance contribution is added only when particle pairs are within a critical distance from each other, which was taken as a center-to-center distances of four radii in the studies cited above. While $\mathcal{M}$ is computed at the two body level, its inverse captures all the many body interactions [Durlofsky *et al.*, 1987] [37]. So in their study, both the far-field and near-field interactions are computed correctly, the wall is approximated as a planar lattice of spheres, creating a "bumpy" wall. Though the use of this "bumpy wall" did not alter the large-scale dynamics of the suspension, it clearly resulted in particles near the walls recording a bumpy motion, which they subtracted off while computing the mean velocity fluctuation. To remove this and other complications arising from a bumpy wall and at the same time to simulate plane Couette flow that is infinite in the flow and vorticity directions Singh and Nott [122] extended the Stokesian Dynamics technique to allow plane boundaries.

The only modification to the procedure developed by Singh & Nott [2000] [122] different from that of Nott & Brady [1994] [94] is to use the exact sphere-wall resistances for interactions of the suspended particles with either of bounding walls. The far-field sphere-wall mobility is still computed as before, as a multipole expansion of the force density; in other words, the walls are discretized as a string of spheres to compute the far-field interactions. This enables us to use the efficient method of Brady *et al.*[1988] [20] for computing $\mathcal{M}$ as a lattice sum using Ewald's re-summation technique, in the simulation of uniformly sized spheres employing periodic conditions. In the formalism of Durlofsky & Brady, this scheme is in effect equivalent to an infinite discretization of the boundaries.

3.2.1 Formation of the grand mobility matrix

Singh and Nott [122] consider a simulation cell with N_l spherical particles each of size a, suspended in a Newtonian fluid of viscosity η and bounded by two plane walls which extend to infinity. Each wall is constructed by sticking spheres together in a plane. Let N_w be the total number of wall particles ($\frac{\mathrm{N}_w}{2}$ in each wall). The grand moblility matrix relates the particle velocities of all $\mathrm{N}_\mathrm{l} + \mathrm{N}_w$ particles to the forces and stresslets and is same as given in (3.14), i.e.,

$$\begin{pmatrix} \mathbf{U} - < \mathbf{u} > \\ - < \mathbf{e} > \end{pmatrix} = \mathcal{M} \begin{pmatrix} \mathbf{F} \\ \mathbf{S} \end{pmatrix} \tag{3.18}$$

where $\mathbf{U}$ is a vector (of dimension 6N) containing translational and rotational velocities of all the particles (N is the sum of wall particles and interior particles in the simulation cell), $\mathbf{F}$ is a vector (of dimension 6N) containing the force and torque on each particle, $\mathbf{S}$ and $< \mathbf{e} >$ each are vectors (of dimension 5N each) including particle stresslets and applied strain rate respectively and $< \mathbf{u} >$ is the average velocity of the whole suspension. In this simulation, flow is driven by the motion of the boundaries (wall particles), and so $< \mathrm{e} >$ is zero. However, while forming the grand mobility matrix, the moblility couplings related to $< \mathbf{e} >$ are retained. The grand moblility matrix thus formed is of dimension 11N×11N. The vectors $\mathbf{U}$, $\mathbf{F}$ and $\mathbf{S}$ are arranged in the following manner:

$$\mathbf{U} = \begin{pmatrix} U^1 & U^2 & \cdots & U^{\mathrm{N}_\mathrm{l}} & U^{\mathrm{N}_\mathrm{l}+1} & \cdots & U^{\mathrm{N}} \end{pmatrix}^t,$$

$$\mathbf{F} = \begin{pmatrix} F^1 & F^2 & \cdots & F^{\mathrm{N}_\mathrm{l}} & F^{\mathrm{N}_\mathrm{l}+1} & \cdots & F^{\mathrm{N}} \end{pmatrix}^t,$$

$$\mathbf{S} = \begin{pmatrix} S^1 & S^2 & \cdots & S^{\mathrm{N}_\mathrm{l}} & S^{\mathrm{N}_\mathrm{l}+1} & \cdots & S^{\mathrm{N}} \end{pmatrix}^t$$

The components of the above vectors for each particle are:

$$U^{\alpha} = \left(U_x^{\alpha} \quad U_y^{\alpha} \quad U_z^{\alpha} \quad \Omega_x^{\alpha} \quad \Omega_y^{\alpha} \quad \Omega_z^{\alpha}\right)^t,$$

$$F^{\alpha} = \left(F_x^{\alpha} \quad F_y^{\alpha} \quad F_z^{\alpha} \quad T_x^{\alpha} \quad T_y^{\alpha} \quad T_z^{\alpha}\right)^t,$$

$$S^{\alpha} = \left(S_{xx}^{\alpha} \quad S_{xy}^{\alpha} \quad S_{xz}^{\alpha} \quad S_{yy}^{\alpha} \quad S_{yz}^{\alpha}\right)^t$$

and the $<\mathbf{e}>$ components are ordered as:

$$<\mathbf{e}> = \left[(<e>_{xx} - <e>_{zz}) \quad 2<e>_{xy} \quad 2<e>_{xz} \quad (<e>_{yy} - <e>_{zz}) \quad 2<e>_{yz}\right]^t$$

For monolayer simulations, where particles are restricted to remain in the $x-y$ plane, the degree of freedom is reduced. The particles will have translational velocities only in x and y direction and rotation only about the z axis. The particles also experience forces in x and y directions and a torque about z axis. Then, the above vectors will have the following components,

$$U^{\alpha} = \left(U_x^{\alpha} \quad U_y^{\alpha} \quad \Omega_z^{\alpha}\right)^t,$$

$$F^{\alpha} = \left(F_x^{\alpha} \quad F_y^{\alpha} \quad T_z^{\alpha}\right)^t,$$

$$S^{\alpha} = \left(S_{xx}^{\alpha} \quad S_{xy}^{\alpha} \quad S_{yy}^{\alpha}\right)^t$$

$$<\mathbf{e}> = \left[(<e>_{xx} - <e>_{zz}) \quad 2<e>_{xy} \quad (<e>_{yy} - <e>_{zz})\right]^t$$

Therefore, the vectors $\mathbf{U}$, $\mathbf{F}$, $\mathbf{S}$ and $<\mathbf{e}>$ in equation (3.18) will be each of dimension 3N and the grand mobility matrix $\mathcal{M}$ will be of dimension 6N×6N.

3.2.2 Adjustment for lubrication

On inverting the grand mobility matrix, we get the following set of equations:

$$\begin{pmatrix} \mathbf{F}^s \\ \mathbf{F}^w \\ \mathbf{S}^s \\ \mathbf{S}^w \end{pmatrix} = \mathcal{M}^{-1} \cdot \begin{pmatrix} \mathbf{U}^s - <\mathbf{u}> \\ \mathbf{U}^w - <\mathbf{u}> \\ -<\mathbf{e}> \\ -<\mathbf{e}> \end{pmatrix} \tag{3.19}$$

This equation is a far-field approximation of the sphere-sphere and sphere-wall interactions, and lacks the near -field lubrication interactions which are added pairwise. However, those involving particle and wall require separate adjustments to account for sphere-wall lubrication. As there is no relative motion between wall discretizations, they do not need any adjustment for lubrication. The final sphere-wall resistance $\mathcal{R}^{sw}_{FU}$ for each wall is computed by summing the mobility inverse over the discretization (which is thought of as spheres for the purpose of calcuating $\mathcal{M}$) in the wall, then adding the exact near-field sphere-wall resistance and lastly subtracting the far-field part of the resistnce. That is,

$$\mathcal{R}^{sw}_{FU} = \sum_{k} (\mathcal{M}^{-1})^{sk}_{FU} + \mathbf{R}^{sw}_{FU} - \mathbf{R}^{sw\infty}_{FU} \tag{3.20}$$

where the summation above is over all the mobility discretization on the wall.

The far-field part of the sphere-wall resistance, $\mathbf{R}^{sw\infty}_{FU}$, is determined by forming a mobility matrix for a sphere and all the wall "particles" and then inverted. The $\mathbf{R_{FE}}$ and $\mathbf{R_{SE}}$ interactions are same as in Nott and Brady [1994] [94].

To generate uniform shear, all the wall particles of a plane translate with the same velocity, making them indistinguishable from each other. Since the approach of including sphere-wall interactions is equivalent to an infinite discretizaion of each plane (by using Ewald's summation), the lubrication interactions can be associated to any wall particle. In this simulation the sphere-wall lubrication interactions are added to the nearest wall particle. Thus only the nearest wall particle will have the lubrication interaction added to it and the total sphere-wall mobility inverse ($\mathbf{R}^{sw\infty}_{FU}$) subtracted from it. While computing the sphere-wall interactions, it is not possible to treat both the infinite planes simultaneously [Durlofsky and Brady, 1989] [38], [Happel and Brenner, 1973] [58] as analytical solutions for the motion of a single particle between two plane walls are not available. However, Ganatos *et al.*[1980] [47] have found that when a particle is close to one plane and more than five radii away from another, the interaction with the near plane dominates. In all our simulations, spacing between plane walls is more than ten radii, and so , for adding lubricaton interactions, the plane walls are treated individually. The sphere-wall interactions are adjusted only when the particles are less than 3 radii away from the wall. For distance more than 3 radii, the mobility inverse is left unchanged.

To simulate plane walls more accurately, Anugrah Singh and Nott [122] modified the procedure of Nott and Brady [94] by using the exact sphere-wall resistances while computing the near field interactions, but used the bumpy wall model for computing the far field interactions. To simulate fully developed plane Couette flow, they introduced a layer of pure fluid adjacent to the layer of suspension in the master cell, which was then replicated periodically in the three directions. While forming the grand mobility matrix, the wall is still considered as a plane of connected spheres, as in Nott and Brady [94]. The adjustment of the resistance matrix for lubrication between two spheres is unchanged, but the interaction between sphere and wall is treated differently. The exact sphere-wall lubrication interactions are added to the nearest wall particle, as done by Durlofsky and Brady [38]. All the "particles" comprising each wall are assigned equal velocities. To generate homogeneous shear flow, the suspension is enclosed between two plane parallel walls, which are given equal and opposite velocities. Upon solution of the final set of equations, the sphere velocities and wall forces are determined. In this work, we follow exactly the procedure of Singh and Nott [122], [Singh, 2000] [123]. In the literature other methods for simulation of Couette flow of non-Brownian suspension for 2D and 3D are available [Janneke Kromkamp *et al.*, 2006] [65].

3.3 Simulation of plane Couette flow

To simulate bounded plane shear, the suspension is restrained between two plane parallel walls translating relative to each other at a constant speed U_0. This cell can not, however, be replicated periodically in the y (gradient) direction, and the Ewald summed mobility matrix with periodic replication only in x and z direction, loses positive definiteness. To allow replication of the simulation cell in the y direction, Singh and Nott [2000] [122] introduced a layer of pure fluid below the lower wall, as shown in figure (3.1). When this cell comprising the layer of suspension restrained between the two walls and the layer of pure fluid, is replicated periodically in all directions (flow, verticity and gradient directions) , a negative shear rate is imposed on the suspension and a positive shear rate on the layer of pure fluid. The distance between the two walls containing the suspension is henceforth referred to as the Couette gaps. In all our simulations, the Couette gap H is equal to the thickness of the layer of pure fluid. The master cell (see fig.(3.1)), containing a finite number of particles, is replicated periodically to achieve a suspension layer of infinite extent in the flow, vorticity and gradient directions to generate fully developed flow between plane parallel walls. The velocities of the walls are fixed and the forces on them are to be determined, while the forces on the particle are fixed and their velocities

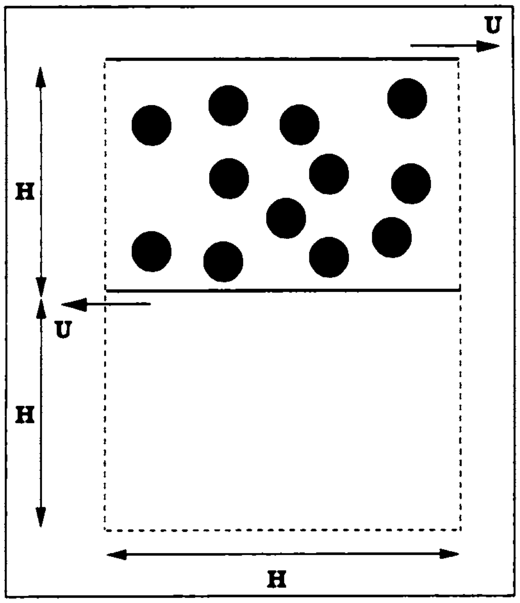

Figure 3.1: A schematic representation of the master cell for our simulations. The layer of pure fluid (below the lower wall) allows us to periodically replicate the master cell and yet impose uniform shear in the suspension (refer [Singh and Nott, 2000] for details). The thickness of the suspension and fluid layers, H, are equal to the length of the unit cell.

are to be determined. For computational convenience, we have performed monolayer simulations in which the spheres are restricted from translating in the z-direction and the rotational movement of the spheres is allowed in the z-direction only. However, we expect that the essential physics of the problem is retained in a monolayer simulation [Nott and Brady, 1994] [94], [Brady and Bossis, 1985] [21].

The velocities of the suspended particles are given by

$$\boldsymbol{R}_{FU}^{ss}\cdot(\boldsymbol{U}^{s}- < u >) + \boldsymbol{R}_{FU}^{sw}\cdot(\boldsymbol{U}^{w}- < u >) = \boldsymbol{F}^{s}, \tag{3.21}$$

and the forces on the walls by

$$\boldsymbol{R}_{FU}^{ws}\cdot(\boldsymbol{U}^{s}- < u >) + \boldsymbol{R}_{FU}^{ww}\cdot(\boldsymbol{U}^{w}- < u >) = \boldsymbol{F}^{w}. \tag{3.22}$$

Here, $\boldsymbol{U}^{s}$ is the vector of velocities of the suspended particles, and $\boldsymbol{F}^{s}$ is the vector of (external) forces on them. Similarly, $\boldsymbol{U}^{w}$ and $\boldsymbol{F}^{w}$ are the velocities and forces, respectively, of the wall discretizations. In order to ensure that the flow in the Couette gap is uniform shear and there is no pressure driven flow, the mean velocity over the entire domain, $< u >$ is set to zero. The resistance $\boldsymbol{R}_{FU}$ depends only on the configuration, or the separation between particles, and the superscripts on it indicate the couplings between the spheres and walls (see [Singh and Nott, 2000] [122]).

Equations (3.21) and (3.22) give the hydrodynamic forces on the spheres and walls. The dynamics of the spheres and walls is determined once the external force is specified.

$$\boldsymbol{F}_{hyd} + \boldsymbol{F}_{ext} = 0 \tag{3.23}$$

While there is no external body force on the particles, we have imposed an inter-particle repulsive interaction between the spheres (there is no inter-particle force between the spheres and the wall) and its utility is to provide a qualitative model of non-hydrodynamic effects when the inter-particle separation is small; the repulsive interaction also prevents frequent particle overlaps. Recenlty Dratler and Schowalter [1996] [34] have shown that Stokesian Dynamics simulations employing a short-range repulsive force result in more realistic micro-structures. In a suspension of non-Brownian spherical particles undergoing shear at zero Reynolds number, the separation between spheres can be very small (less than 10^{-4} of their radius). In this situation, the effects of surface roughness can not be neglected and a short-ranged, repulsive force is usually introduced between the spheres to qualitatively model the behavior of real systems. The introduction of such a force has the further numerical advantage of preventing the occurrence of overlaps during close encounters between spheres even though the time step for the simulation is not reduced. The form of the repulsive force we have used is the same as in the simulations of [Nott and Brady, 1994] [94],

$$F_{\alpha\beta} = F_0 \frac{\mu e^{-\mu\epsilon}}{1 - e^{-\mu\epsilon}} e_{\alpha\beta} \tag{3.24}$$

where $F_{\alpha\beta}$ is the force exerted by sphere β on sphere α. The parameters μ and F_0 specify the range of the force and its magnitude, respectively, ϵ is the separation between the surfaces of the spheres and $e_{\alpha\beta}$ is the unit vector connecting the sphere centers.

Upon determining $\boldsymbol{U}^s$ for a given configuration, the particle positions are updated by integrating the equation

$$\frac{d\boldsymbol{x}^s}{dt} = \boldsymbol{U}^s, \tag{3.25}$$

in time using the fourth order Adams-Bashforth technique. This equation allows one to determine the particle configurations at any time. The shear stress σ_{yx} and the normal stress σ_{yy} are determined directly from the forces on the walls and the entire process of solving (3.21)-(3.25) is repeated to continue the simulation. Equation (3.22) gives the hydrodynamic force exerted by the fluid on each of the wall particles. To compute the force over the entire wall, we simply sum over all the particles of the wall. From the forces on the walls, the shear stress σ_{xy} and normal stresse σ_{yy} in the suspension are easily determined,

$$\sigma_{xy} = \frac{F_x^W}{A_w}; \quad \sigma_{yy} = \frac{F_y^W}{A_w} \tag{3.26}$$

where F_x^W and F_y^W are averages of the magnitude of the x and y components of forces on the two walls and A_w is the total wall area for either plane. All the stresses are nondimensionalised by the shear stress that would exist in the absence of any particles, i.e. by $\eta\dot{\gamma}$, where η is the fluid viscosity and $\dot{\gamma}$ is the nominal shear rate,

$$\dot{\gamma} = \frac{2U_0}{H} \tag{3.27}$$

where U_0 is the speed of the wall and H is the channel width.

3.4 Characterization of stresses

The characterization of total stress is important for the rheological studies of suspensions. In a suspension of solid particles in an incompressible fluid, Batchelor[1970][14] gives the expression for bulk stress averaged over the volume V containing N particles:

$$<\Sigma> = - <p>_f I + 2\eta <E> + <\Sigma^p> \tag{3.28}$$

where $<p>_f$ is the average pressure in the fluid phase that would exist when no particles are present, $2\eta <E>$ is the contribution to the bulk stress from the fluid phase and $<\Sigma^p>$ is the particle contribution to the bulk stress. In the absence of Brownian motion, $<\Sigma^p>$ is given by

$$<\Sigma^p> = \frac{N}{V}\{<S^H> + <S^P>\} \tag{3.29}$$

where $<S^H>$ and $<S^P>$ are the contributions to the stress arising from hydrodynamic and inter-particle forces, respectively. And they are given by

$$\mathrm{S}^H = -\mathcal{R}_{SU}^{ss} \cdot (\mathcal{R}_{FU}^{ss})^{-1} \cdot \mathcal{R}_{FU}^{sw} \cdot (U^w - <u>) + \mathcal{R}_{SU}^{sw} \cdot (U^w - <u>) \tag{3.30}$$

The bulk hydrodynamic stress is then determined from

$$< S^H >= \frac{1}{N}\sum_{\alpha=1}^{N} S^\alpha \tag{3.31}$$

The contribution to the bulk stress by the inter-particle force is computed using

$$< S^P >= \frac{1}{N}\sum_{\alpha=2}^{N}\sum_{\beta<\alpha} \boldsymbol{r}^{\alpha\beta}\boldsymbol{F}^{\alpha\beta} + < \mathcal{R}_{SU}^{ss} \cdot (\mathcal{R}_{FU}^{ss})^{-1} \cdot \boldsymbol{F}^P > \tag{3.32}$$

The presence of suspended particles alter the boundary conditions locally, and thereby altering both velocity field and pressure field. The extra pressure generated by the presence of particles is called particle pressure and is given by the one-third of the trace of the particle contribution to the bulk stress $< \Sigma^p >$, i.e.,

$$\Pi = \frac{1}{3}Tr(< \Sigma^p >) \tag{3.33}$$

In computing the far-field part of the hydrodynamic interaction between the particles, Stokesian Dynamics uses a moment expansion of the force density acting on each particle. The first moment of the surface stress is decomposed into an antisymmetric part (which equals the couple acting on the particle) and a symmetric traceless part or stresslet. It is the trace of the first moment which is needed for the pressure interactions and this has not been incorporated in the mobility matrix. This is because the mobility matrix $\mathcal{M}$, which accounts for the far-field part of the hydrodynamic interactions, was constructed assuming that $\Sigma S_{ii} = 0$. The near-field interactions are accounted for by the exact two-body resistance, $\mathcal{R}_{2b}$, and therefore do capture the isotropic part of the stresslet. In the Singh and Nott simulations, the shear stress σ_{yx} can be computed either by computing the net force on the walls in the x direction or from the mean stresslet on the suspended particles. The net normal stress σ_{yy} on the wall can be written as

$$\sigma_{yy} = -\Pi_{ff}^H + \frac{N}{V}\left\{< S_{yy}^H > + < S_{yy}^P >\right\} \tag{3.34}$$

where Π_{ff}^H comes from the far-field part of the stresslet, which was left out while computing the mobility matrix $\mathcal{M}$. Since σ_{yy} and S_{yy}^H are computed independently in their simulations, and S^P_{yy} is readily determined for each particle configuration, the isotropic far-field stress Π^H_{ff} can be determined from (3.34). The stress σ_{xx} is computed from

$$\sigma_{xx} = -\Pi^H_{ff} + \frac{N}{V}\left\{< S^H_{xx} > + < S^P_{xx} >\right\} \tag{3.35}$$

Thus σ_{yx}, σ_{xx} and σ_{yy} can be computed from the forces on the walls and the particle stresslets.

All the results described in this work are for sheared suspension of spheres confined to a monolayer. The centers of all suspended spheres in the master cell lie in the $x-y$ plane, and are restricted from translating in the z direction. Additionally, rotational movement of the spheres is allowed in the z direction only. In all simulations, the top of the plane translates with velocity $U^t_w = -1$ and the bottom plane with $U^b_w = 1$. The only parameters in the problem are the Couette gap H (rendered non-dimensional by the particle radius), the area fraction of particles ϕ given by

$$\phi = \frac{N_1\,\pi\,a^2}{H\,L_x} \tag{3.36}$$

where N_1 is the number of interior particles, L_x is the cell length in the x direction and, the parameters that determine the repulsive interaction F_0 (3.24) and μ.

The system of equations (3.25) was integrated with a time step of 0.01. The mobility matrix was inverted infrequently (once every 100 time steps), however the lubrication forces were adjusted at each time step. The initial configuration of the suspended spheres was generated by first arranging the particles in a regular array and then applying small random displacements until a uniform distribution was achieved. In all the simulations the structure was allowed to evolve from start till $t = 5000$, and the properties such as the concentration, velocity and stress fields were then averaged over the subsequent 95000 dimensionless time units. We computed the stresses for a range of these parameters, and analyzed their time series. The stresses we report are non-dimensionalized by $\eta U/H$ (see fig.(3.1)), η being the viscosity of the pure suspending fluid.

CHAPTER 4

Nonlinear Time Series Analysis

4.1 Introduction

Deterministic chaos as a fundamental concept is by now well established and described in a rich literature. The fact that simple deterministic systems generate complicated temporal behavior in the presence of nonlinearity has influenced our thinking and has drastically changed our view about understanding of scientific phenomena in many fields. Nonlinear time series analysis (Nonlinear Dynamics Analysis) and chaos theory have posed two important questions: (a)whether chaos theory can be used to gain a better understanding and interpretation of observed complex dynamical behavior and (b) whether chaos theory can give an advantage in predicting or controlling such time evolution. Most dynamical system behavior can be expressed in terms of time series and time evolution as a system property can be measured by recording time series. And so nonlinear time series methods will likely be the key to answer the above questions. While analysing the fluctuations and temporal changes of stresses using nonlinear methods of analysis, we will see how far we are able to give a better interpretation of the results obtained.

The rheology of macroscopically homogeneous sheared suspensions of neutrally buoyant, non-Brownian spheres is analysed in the limit of vanishingly small Reynolds numbers

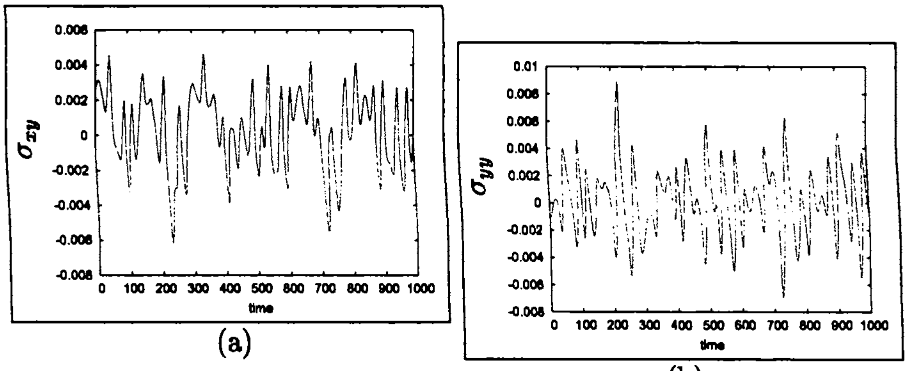

(a) (b)

Figure 4.1: Time series (arbitrary units) of (a) shear stress σ_{xy} and (b) normal stress σ_{yy} at area fraction ϕ=0.05

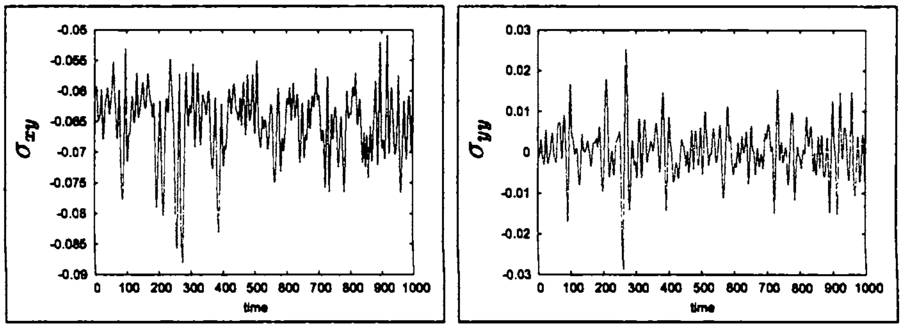

(a) (b)

Figure 4.2: Time series of (a) shear stress σ_{xy} and (b) normal stress σ_{yy} at area fraction ϕ=0.10

using nonlinear time series methods. Most nonlinear time series methods are described in monographs, eg. [Abarbanel, 1996] [2]; [Kantz and Schreiber, 1997] [69]; [Small, 2005] [129].

Systematic analysis of a fluctuating time series can be performed by means of nonlinear methods and/or by linear methods. Some characteristics which can not be quantified using linear methods can be characterised using nonlinear methods and chaos theory. Linear methods interpret all regular structure in a data set, such as a dominant frequency, as linear correlations. That is, the intrinsic dynamics of the system is governed by the linear paradigm that small causes lead to small effects. Linear equations can only lead

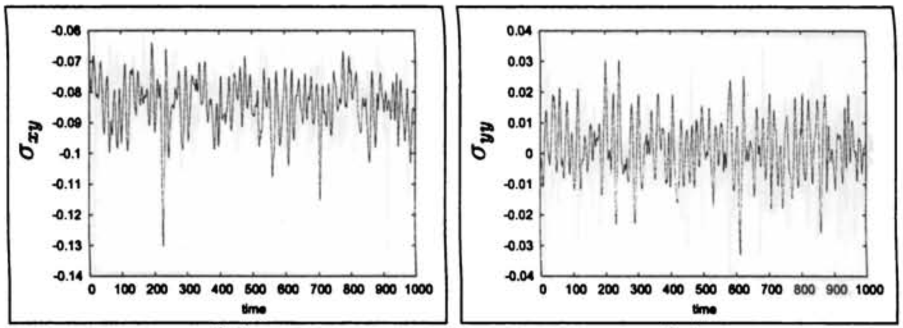

(a) (b)

Figure 4.3: Time series of (a) shear stress σ_{xy} and (b) normal stress σ_{yy} at area fraction ϕ=0.20

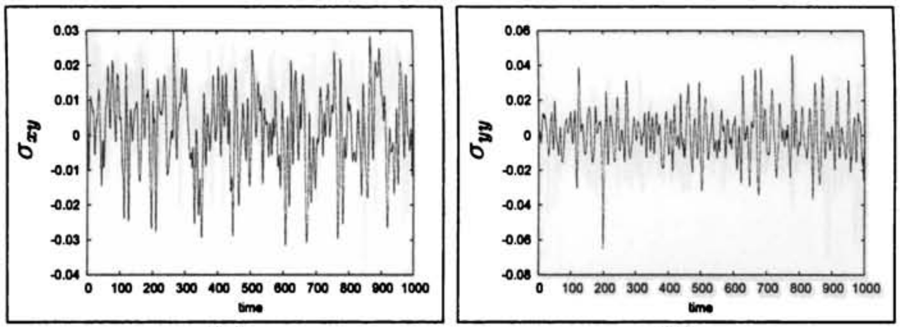

(a) (b)

Figure 4.4: Time series of (a) shear stress σ_{xy} and (b) normal stress σ_{yy} at area fraction ϕ=0.30

to exponentially growing or periodically oscillating solutions, all irregular behavior of the system has to be attributed to some random external input to the system. In some situations a combined application of both linear and nonlinear time series methods will be valuable. Chaos theory yields a new perspective that random input is not the only possible source of irregularity in a system's output, but nonlinear, chaotic systems can produce very irregular data with purely deterministic equations of motion.

We computed the normal stress σ_{yy} and shear stress σ_{xy} for various area fractions of particles. We performed a linear shift of the shear stresses changing its average approximately to zero in most of the shear stress time series so as to make a simultaneous comparison with the corresponding normal stress components at the respective area frac-

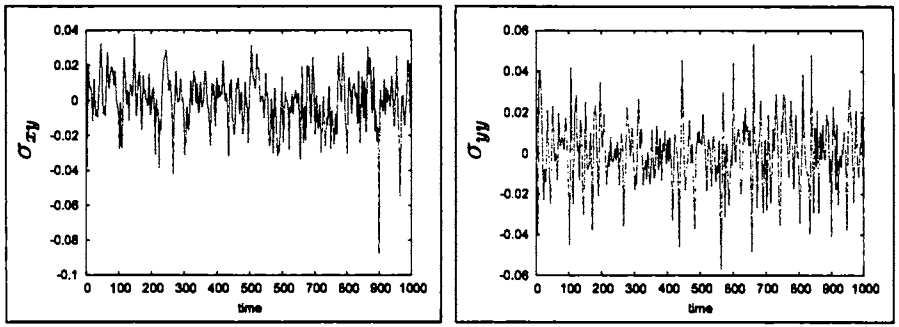

(a) (b)

Figure 4.5: Time series of (a) shear stress σ_{xy} and (b) normal stress σ_{yy} at area fraction ϕ=0.40

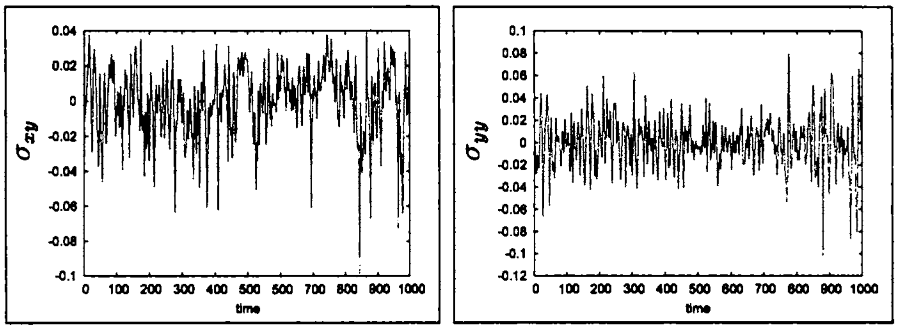

(a) (b)

Figure 4.6: Time series of (a) shear stress σ_{xy} and (b) normal stress σ_{yy} at area fraction ϕ=0.45

tions. Figures (4.1) to (4.8) show the fluctuations in the shear and normal stresses in a non-Brownian suspension of identical spheres in a regime of vanishingly small Reynolds number for various area fractions of particles ranging from 0.05 to 0.6 and Couette gap $H = 18$ particles width. The plot of these fluctuations of stresses for these area fractions show very persistent temporal fluctuations in time. We, also, observe that the rheological properties viz. shear and normal stress components fluctuate about well defined averages [Singh and Nott, 2000] [122].

A detailed analysis of these irregular fluctuations in the stress, using topological and dynamical methods, may reveal significant features about the dynamical system. The basic feature in the analysis using nonlinear dynamical methods is the characterization of

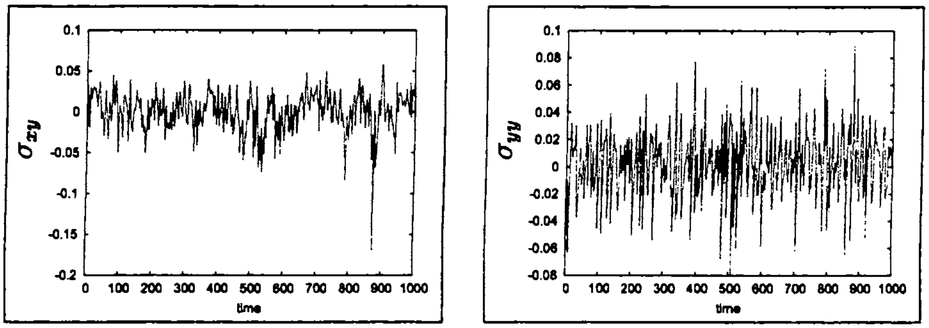

(a) (b)

Figure 4.7: Time series of (a) shear stress σ_{xy} and (b) normal stress σ_{yy} at area fraction ϕ=0.50

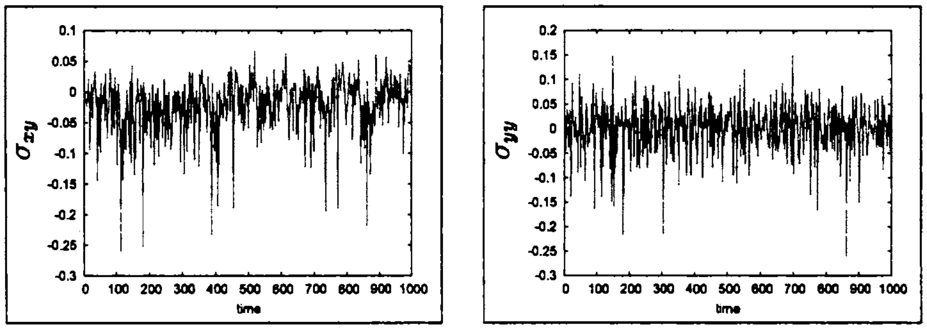

(a) (b)

Figure 4.8: Time series of (a) shear stress σ_{xy} and (b) normal stress σ_{yy} at area fraction ϕ=0.60

the attractor, a bounded subset of the phase space to which the system behavior eventually converges as it evolves in time. This characterization is based on the reconstruction of the attractor of the system using delay reconstruction or other similar methods. A critical review in implementing different methods for the characterization of attractor of dynamical systems and its implications are given in [Schreiber, 1999] [119] and references therein.

4.2 Phase space reconstruction

The works of Takens[132], Casdagli [26], and others have established the methodology for building a dynamical model from a chaotic time series. In their approach, the time series $\{x(t_i)_{i=1}^{N}\}$, describing the system evolution is considered as the output of a deterministic, nonlinear autonomous dynamical system. A continuous dynamical system may be expressed using the differential equation

$$\frac{d}{dt}\boldsymbol{x}(t) = F(t, \boldsymbol{x}(t)), \quad \text{where } t \in R \tag{4.1}$$

where $\boldsymbol{x}(t)$ represent the dynamics of a system, $\boldsymbol{x}$ being the properties that identify its state. In an experiment, we may be able to measure only a single scalar as a function of time $y(t)$. For instance, in a fluid flow experiment we may be able to measure the pressure as a function of time. Since the pressure depends only on the state of the system, we have a functional relation $y(t) = h(\boldsymbol{x}(t))$, where h is a scalar valued measurement function which relates the dynamical system (4.1) with the measured variable y. When working with measured data, we generally do not know the state equations describing the dynamical system; but we are restricted to the observed output of the dynamical system (4.1) in the form of a time series; in most cases just one column of data of finite length. So a fundamental issue is what can be inferred about the dynamics of the system from the observations of the output time series $\{x(t_i)\}_{i=1}^{N}$. As a starting point to find a solution to this issue, we now define, what we call, the **delay coordinate vector**:

$$[y(t),\ (y(t+\tau),\ y(t+2\tau),\ \ldots,\ y(t+(m-1)\tau)]$$

with time delay τ, and propose that it is related to $\boldsymbol{x}(t)$ by

$$\begin{aligned} \Phi[\boldsymbol{x}(t)] &= [y(t), y(t+\tau), \ldots, y(t+(m-1)\tau)] \\ &= [h(\boldsymbol{x}(t)), h(\boldsymbol{x}(t+\tau)), \ldots, h(\boldsymbol{x}(t+(m-1)\tau)] \end{aligned} \tag{4.2}$$

[Takens,1981][132] showed that for autonomous and purely deterministic systems, the delay reconstruction map Φ, a bicontinuous differentiable function (diffeomorphism) which maps the state $\boldsymbol{x}$ into an m-dimensional delay vector, is an embedding when $m \geq 2n+1$, where n is the dimension of the phase space in which the attractor of the dynamical system evolves. (We say that $\Phi : \boldsymbol{X} \to \boldsymbol{Y}$ is an embedding of one compact space $\boldsymbol{X}$ into another $\boldsymbol{Y}$, if there is a one to one correspondence between $\boldsymbol{X}$ and $\Phi(\boldsymbol{X})$ with Φ and Φ^{-1} continuous, such that it preserves differentiable structure [Ott *et al.*, 1994] [95] of the attractor including such quantities as Lyapunov exponents, dimension estimates etc.) This theorem, called **Takens' Embedding theorem**, asserts that if the attractor dimension is n, then for a complete understanding of the attractor $2n + 1$ dimensions in the embedded space are sufficient. Further generalizations [Sauer and Yorke, 1997,1993] [117], [118] assert that any embedding dimension larger than the box counting attractor dimension (see §4.4) is sufficient, and in most cases the smallest integer greater than the correlation dimension (see §4.4) is sufficient for a complete characterization of the attractor [Ding *et al.*, 1993] [33]. Hence most of the significant characteristics, dynamical and geometrical, of the original system are carried over to the reconstructed phase space. Mathematically speaking, the characteristics of the original phase space are topologically and metrically equivalent to its mirror dynamical flow in the reconstructed phase space i.e., the orbits of the original phase space are transformed into orbits in the reconstructed phase space in such a way that their sense of orientation is preserved. Further, topological properties such as the number of significant eigen values, and dynamical and metrical properties such as Lyapunov exponents and different types of dimension measures (correlation dimension, Lyapunov dimension, box counting dimension, information dimension etc.) are preserved [Ott *et al.*, 1994] [95]. In view of embedding theory, we can estimate the various dimensions and Lyapunov exponents, and perform reasonable predictions of future events based on this mapping. There are different methods of phase space reconstruction. Another popular method of the phase space reconstruction is using derivative coordinates. A comparative study of embedding methods is discussed in [Cellucci *et al.*, 2003] [28].

4.3 Choosing the time delay τ

A direct application of the embedding theorem in real situations is impractical as it is valid only for an infinitely long and noise free time series of a dynamical system. In principle, there is no restriction on the choice of the time delay. In practice, however, proper choice of both time delay and embedding dimension are of great significance and the information contained in a time delay representation of real data is greatly influenced by the choice of these embedding parameters. Noise is usually of frequencies higher than those of the inherent dynamics of the system, and therefore imposes a lower bound on the time delay; using a time delay smaller than the largest significant noise time period will result in artificially high dimension. Even in the absence of noise, choosing too small a time delay will illustrate only the temporal correlation in the data, rather than its chaotic dynamics. Using too large a time delay runs the risk of missing genuine variations at smaller time scales. Thus, the optimal time delay is one for which the characteristics of the dynamics observed in the embedded space are not due to noise and temporal correlations [Galka, 2003] [49] of points on the one hand, but the inherent dynamics of the system are not left out on the other. There are different methods to estimate proper time delay. In the following, we consider some popular methods to determine the suitable time delay from a time series.

4.3.1 Autocorrelation function

This can be quantified by using the autocorrelation function,

$$\mathcal{A}(\tau) = \sum_{n} (x_n - \bar{x})\,(x_{n+\tau} - \bar{x}), \tag{4.3}$$

which is a normalized measure of the linear correlation among successive values of a time series $\{x_n\}_{n=1}^{N}$. Above, $\bar{x}$ is the temporal mean of the time trace $\bar{x} = 1/N \sum_{n=1}^{N} x_n$. The decay of the autocorrelation with τ is a direct way to determine the decorrelation lag time (the time needed for the system to 'forget' its initial conditions). The optimal time delay can be taken as the value of τ at which the autocorrelation function attains its first zero [Holzfuss and Mayer-Kress, 1986] [63], or its first local minimum [Graf and Elbert, 1990] [54].

4.3.2 Average mutual information

The time delayed average mutual information (AMI) is also a tool to determine a reasonable delay. A distinguishing feature of AMI over autocorrelation function is that it takes into account the nonlinear correlations in the data; it is given by

$$\mathrm{AMI} = -\sum_{\mathrm{ij}} \mathrm{p_{ij}}(\tau)\ \ln \frac{\mathrm{p_{ij}}(\tau)}{\mathrm{p_i}\,\mathrm{p_j}} \tag{4.4}$$

where p_i is the probability that one data point (observation) falls in the i-th interval for some partition on the real numbers and $p_{ij}(\tau)$ is the joint probability that an observation falls into the i-th interval and the observation time τ later falls into the j-th interval. Here too the optimal delay is that corresponding to the first minimum or zero of the AMI.

4.3.3 Space-time separation plot

Another method to find a proper time lag is the space-time separation plot [Provenzale *et al.*, 1992] [109]. This procedure estimates the time lag for the system to free itself from the temporal correlations of points in phase space [Kantz and Schreiber, 1997] [69]. That is, pairs of points which are measured within a short time span tend to be close in phase space and this will adversely affect the computation of the correlation integral. We use the correlation integral to compute the effective dimension of the underlying dynamics which is not related to the close neighborhood of points in phase space due to temporal correlation. The idea in a space time separation plot is that in the presence of temporal correlations the probability that a given pair of points has a distance smaller than ϵ does not only depend on ϵ but also on the time that has elapsed between the two measurements. This inter-dependence can be detected by plotting the number of pairs of points as a function of two variables, the time separation Δt and the spatial distance ϵ. Using this method, we estimate a proper time delay as that after which the contour lines will attain saturation. This value can be regarded as a fair estimate of the decorrelation time which will exclude the influence of successive points due to temporal correlations. From experience we found that this value is an upper bound to the suitable delay required for the estimation of certain topological and dynamical characteristics of the dynamical system. Another important use of space-time separation plots is to identify stationarity and non-stationarity of the signal. Saturation of the space time separation plot excludes the possibility of non-stationarity in the signal [Kantz and Schreiber, 1997][69].

4.4 Choosing the embedding dimension m

The next crucial problem in nonlinear time series analysis is to fix the number of independent coordinates required to reconstruct the attractor governing the dynamics of the system. The usual procedure is the following: a value of m is assumed and the data embedded in m-dimensional space. The volume of the resulting set is then determined by counting the number of m-dimensional cubes of size ϵ needed to enclose the set. The box counting dimension of the attractor is then given by

$$D_0 = \lim_{\epsilon \to 0} \frac{\ln N(\epsilon)}{\ln(1/\epsilon)}. \tag{4.5}$$

In practice, $N(\epsilon)$ is determined for various embedding dimensions starting from unity, over a range of ϵ. If the plot of $\frac{\ln N(\epsilon)}{\ln(1/\epsilon)}$ against ϵ shows a plateau at approximately the same value for a sufficiently large range of ϵ for all embedding dimensions greater than a critical value m_c, a good approximation to the box counting dimension of the attractor is m_c. In computing the box counting dimension of an attractor, equal importance is given to all the cubes that enclose the data in phase space. However, for attractors having a fractional dimension, certain regions in phase space are visited more frequently by the trajectory and hence greater weightage should be given to cubes in that region. [Grassberger, 1983] [56], [Grassberger and Procaccia, 1983] [57] and others introduced the generalized (information) dimension D_q which depends continuously on q as

$$D_q = \frac{1}{1-q} \lim_{\epsilon \to 0} \frac{\ln I(q,\, \epsilon)}{\ln(1/\epsilon)} \tag{4.6}$$

where

$$I(q,\, \epsilon) = \sum_{i=1}^{N(\epsilon)} \mu_i^q \tag{4.7}$$

where μ_i is the natural measure of cube i and the sum is taken for all the $N(\epsilon)$ cubes of size ϵ needed to enclose the attractor. Here the natural measure of cube i is given by

$$\mu_i = \lim_{T \to \infty} \frac{\eta(i,\, \boldsymbol{x}_0,\, T)}{T} \tag{4.8}$$

where $\eta(i,\, \boldsymbol{x}_0,\, T)$ is the amount of time the orbit originating from a typical point $\boldsymbol{x}_0$ spends in the cube i in the time interval $0 \leq t \leq T$ [Ott, 1993] [96].

4.4.1 Correlation integral method

Of all the D_q dimensions, the correlation dimension D_2 is easiest to compute from a time series. Further simplification of D_2 from the above expression gives

$$D_2 = \lim_{r \to 0} \frac{\ln C(r)}{\ln r} \tag{4.9}$$

where C(r) is the correlation integral for radius r which obeys a scaling relation $C(r) \sim r^{D_2}$ in the limit $r \to 0$. (In general, for a self-similar structure, the correlation integral $C_q(\epsilon)$ of order q satisfies $C_q(\epsilon) \sim \epsilon^{(q-1)D_q}$ as $\epsilon \to 0$). The correlation integral depends on the embedding dimension m of the reconstructed phase space as

$$C(r, m) = \frac{2}{N(N-1)} \sum_{i=1}^{N} \sum_{j=i+1}^{N} \Theta(r - \| \boldsymbol{x}(i) - \boldsymbol{x}(j) \|) \tag{4.10}$$

where $\Theta(a) = 1$ if $a > 0$, and $\Theta(a) = 0$ if $a \leq 0$, $\boldsymbol{x}(t)$ is the m-dimensional vector of time-delay coordinates and N is the length of the time series. The scaling exponent d increases with m and saturates to a final value D_2 for sufficiently large embedding dimension m_c [Ott *et al.*, 1994][95]. In general, it is difficult to find a plateau region for a given value of m. Theoretically, D_2 has to be determined as the radius of the hypersphere r tends to 0 and m large. However, in calculation, small values of r are blurred by noise and limitations on the accuracy of the data and large values of m are not considered due to practical limitations. Practically, one finds a range $(r_L\,,\ r_U)$ of r over which $\frac{\ln C(r,m)}{\ln r}$ gives an approximate plateau region with some tolerance $\pm\,\Delta m$.

For non-stochastic signals, the correlation dimension estimate is unaffected by small variations in the time delay. On the other hand, signals dominated by white noise will show statistically significant changes in the correlation dimension for different embedding dimensions, rarely converging to a fixed estimate of the correlation dimension as m increases (never converging for pure white noise), and small changes in time delay will affect the correlation dimension estimate significantly. In most cases, m_c is the smallest integer larger than D_2 [Ding *et al.*, 1993] [33]. When the exponent d of the correlation integral for various embedding dimensions reveals a plateau at low values of r and the plateau converges for increasing m, there is strong evidence for a low-dimensionality of the underlying dynamics of the system. Usually, the correlation dimension from a time series is compared with other dimension estimates to ensure its veracity. In most cases, it yields a good approximation to the number of equations required to model the system. Further, an accurate measurement of correlation dimension will reveal the possibility of a strange attractor if D is not an integer. Different methods are available for the calculation of the fractal dimension of a strange attractor (attractor with fractional dimension) [Ashkenazy, 1999] [9]. For example, the fractal dimension can be calculated using the Lyapunov spectrum (4.5.3) and the Kaplan-Yorke conjecture [Kaplan and Yorke, 1987] [71]. But the computation of the Lyapunov exponent spectrum see (4.5.3)is very difficult and is not economical. So, in most of the literature, the method introduced by [Grassberger *et al.*, 1991] [55], [Grassberger and Procaccia, 1983] [56], is utilized [Veronig *et al.*, 2000] [136], [Freistetter, 2000] [46] and there is a host of literature pertaining to both theoretical and practical considerations of the correlation integral method. There are different modifications and generalized methods in the literature [Ashkenazy, 1999][9], [Pawelzik and Schuster, 1987a, 1987b] [101], [102] for the computation of the fractal dimension of an attrator.

4.4.2 False nearest neighbor method

Another technique for finding the minimum number of independent variables to describe the dynamics of the system is the false nearest neighbor (FNN) method [Abarbanel, 1996] [2]; [Kennel *et al.* 1992] [72]. The basic idea behind the method is that if an embedding dimension less than the actual dimension of the attractor is chosen, it will not unfold the true geometry of the attractor and there will be self-intersections leading to false neighbors. For example, if a sphere is embedded in two dimensions, the resulting structure will be a circular disc, and diametrically opposite points on the sphere (in the direction of projection) will become false neighbors. To determine the sufficient number of time delay coordinates, one looks for the nearest neighbor $x_d(j)$ in d dimensional embedded space of each vector $x_d(i)$, with respect to any metric. The distance $r_d(i,j)$ between the vectors in d dimensional embedded space is then compared with the distance $r_{d+1}(i,j)$ if the data were embedded in $(d+1)$ dimensions. For instance, if the $\mathcal{L}_2$ metric is used, $r_{d+1}(i,j)$ can be written in terms of $r_d(i,j)$ as

$$r^2_{d+1}(i,j) = r^2_d(i,j) + (x(i+d\tau) - x(j+d\tau))^2. \tag{4.11}$$

If $r_{d+1}(i,j)/r_d(i,j) \gg 1$, $x_d(j)$ is a false neighbor of $x_d(i)$; the cut-off value of the ratio in our calculations, above which the point is taken to be a false neighbor, is 10. If only a small fraction of the neighbors are false, d can be considered to be an embedding dimension for the dynamics of the attractor.

Another popular method to find the minimum embedding dimension from a time series is based on model construction[Ataei *et al.*, 2003][11]. Use of the above methods of finding the dimension of an attractor together leads to a good estimate of the actual dimension of the attractor, but neither of them can replace the other.

4.4.3 Principal component analysis

Along with these methods we used the principal component analysis to find the number of principal components (or significant eigenvalues) contributing to the dynamics of the system. We do not describe the procedure here, but refer the reader to [Broomhead and King 1986] [23] for details. This method gives an upper bound to the number of independent coordinates required to reconstruct the attractor of the dynamical system. We also used some standard tools for the estimation of invariants of the dynamical system which we explain at the appropriate places below. **Most of the figures we consider in this analysis are in arbitrary units.**

4.5 Results and discussion

We restrict our attention to neutrally-buoyant suspensions, where the densities of the suspended particles and the fluid are equal. The initial configuration of the suspended spheres was generated by first arranging the particles in a regular array and then applying small random displacements until a uniform distribution is reached. The system is allowed to evolve for about 5000 dimensionless time units and, the velocity and stress fields are then recorded over the subsequent 95000 time units.

We used the softwares "Chaos Data Analyzer Professional Version 2.1" of the Academic Software Library of the American Physical Society, the TISEAN Package [Hegger

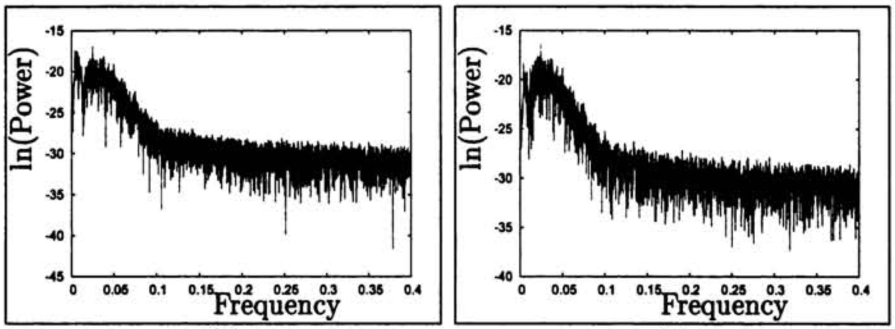

(a) (b)

Figure 4.9: Power spectrum versus frequency for (a) shear stress σ_{xy} and (b) normal stress σ_{yy} at area fraction ϕ=0.05. Exponential decay of the power with frequency is clearly seen, which is characteristic of both chaotic and linear stochastic signals.

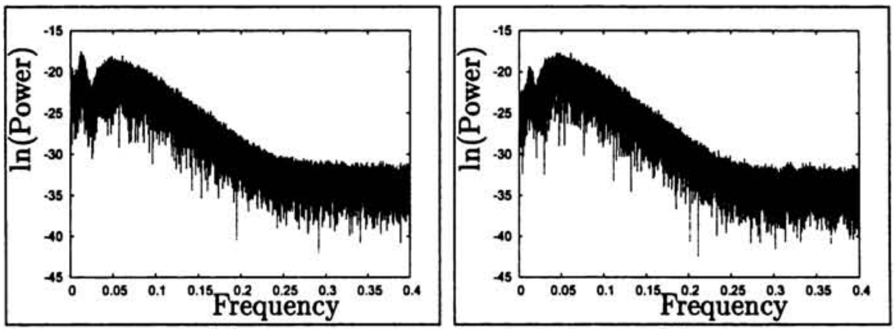

(a) (b)

Figure 4.10: Power spectrum versus frequency for (a) shear stress σ_{xy} and (b) normal stress σ_{yy} at area fraction ϕ=0.10. Exponential decay of the power with frequency is clearly seen, which is characteristic of both chaotic and linear stochastic signals.

et al., 1999] [60], and Visual Recurrence Analysis [Kononov, 1999] [75] for performing the tests on the time series. Of these softwares, we mainly used the TISEAN package as it takes into account most necessary precautions while applying a specific nonlinear time series analysis technique to calculate the required characteristic of the dynamics system from a time series.

A frequency decomposition of the shear and normal stresses for area fractions of particles $\phi = 0.05, 0.1, 0.2, 0.3, 0.4, 0.45, 0.5$ and 0.6 show a broad band power spectrum. Figures (4.9) to (4.16) show the logarithm of the power spectrum versus frequency of

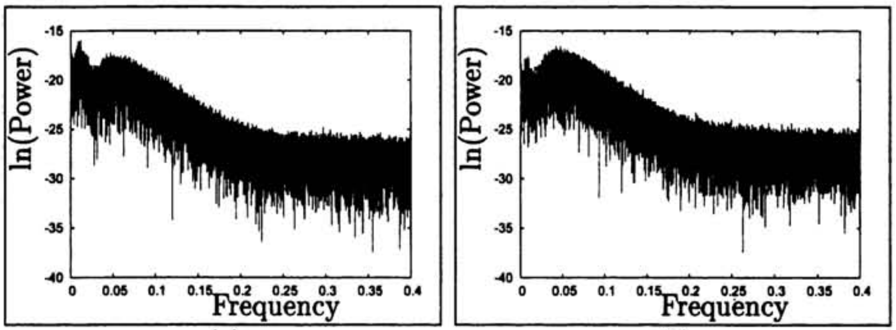

(a) (b)

Figure 4.11: Power spectrum versus frequency for (a) shear stress σ_{xy} and (b) normal stress σ_{yy} at area fraction ϕ=0.20. Exponential decay of the power with frequency is clearly seen, which is characteristic of both chaotic and linear stochastic signals.

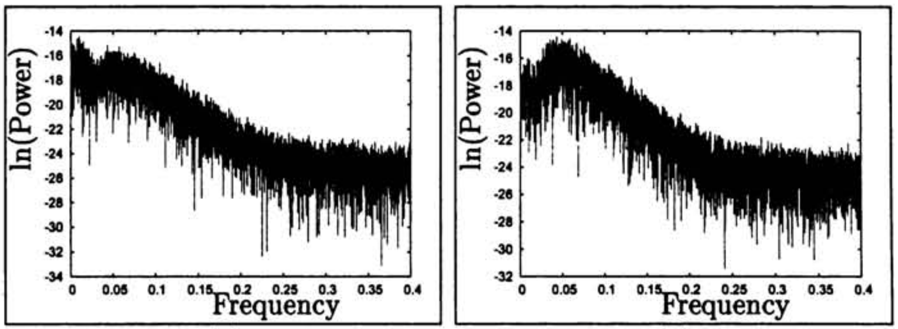

(a) (b)

Figure 4.12: Power spectrum versus frequency for (a) shear stress σ_{xy} and (b) normal stress σ_{yy} at area fraction ϕ=0.30. Exponential decay of the power with frequency is clearly seen, which is characteristic of both chaotic and linear stochastic signals.

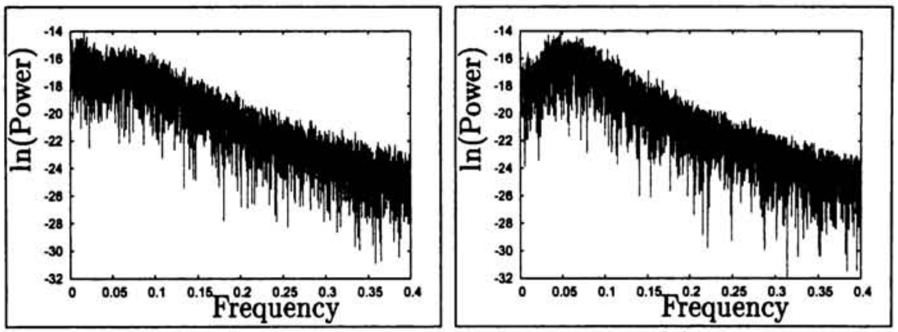

(a) (b)

Figure 4.13: Power spectrum versus frequency for (a) shear stress σ_{xy} and (b) normal stress σ_{yy} at area fraction ϕ=0.40. Exponential decay of the power with frequency is clearly seen, which is characteristic of both chaotic and linear stochastic signals.

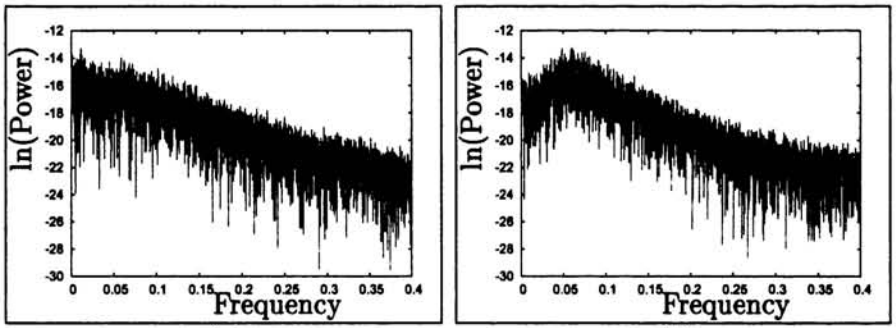

(a) (b)

Figure 4.14: Power spectrum versus frequency for (a) shear stress σ_{xy} and (b) normal stress σ_{yy} at area fraction ϕ=0.45. Exponential decay of the power with frequency is clearly seen, which is characteristic of both chaotic and linear stochastic signals.

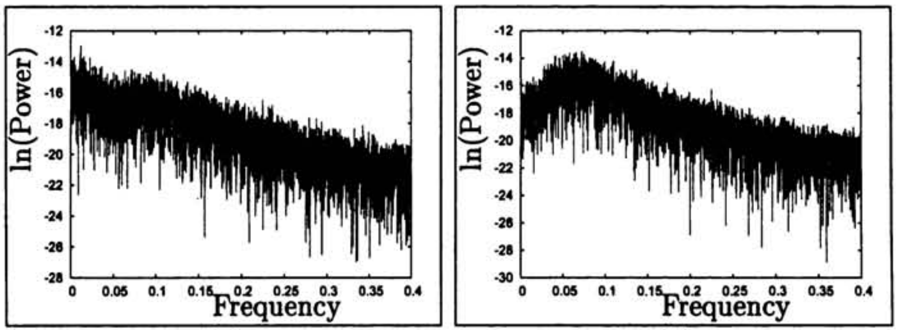

(a) (b)

Figure 4.15: Power spectrum versus frequency for (a) shear stress σ_{xy} and (b) normal stress σ_{yy} at area fraction ϕ=0.50. Exponential decay of the power with frequency is clearly seen, which is characteristic of both chaotic and linear stochastic signals.

the stress components for the above area fractions of particles. The broad band nature of power spectrum is a characteristic of both deterministic chaos and a linear stochastic process [Schuster, 1988] [120]; [Tsonis, 1992] [135]. Also, the figures show exponential decay of the power spectrum, which again is common to both deterministic chaos and linear autocorrelated noise[Schuster, 1988] [120]; [Tsonis, 1992] [135]. The above two properties: broad band power spectrum and exponential decay of power are clearly visible for both the shear and normal stresses at all area fractions of particles.

Therefore, a complete characterization of this behavior must be investigated by meth-

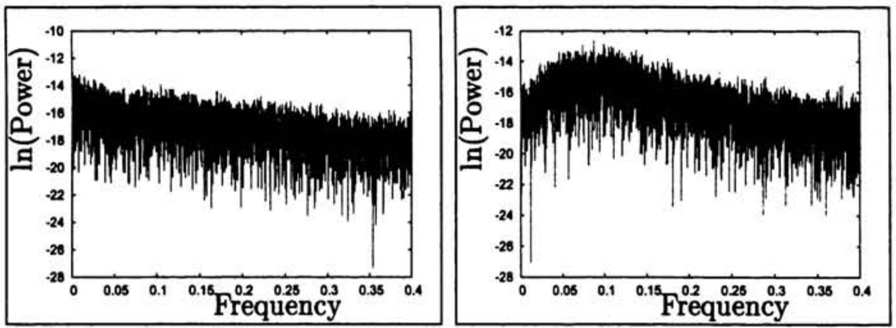

(a) (b)

Figure 4.16: Power spectrum versus frequency for (a) shear stress σ_{xy} and (b) normal stress σ_{yy} at area fraction ϕ=0.60. Exponential decay of the power with frequency is clearly seen, which is characteristic of both chaotic and linear stochastic signals.

ods that can distinguish between deterministic chaos and linear autocorrelated noise (or a stochastic process). In this paper we use both surrogate data analysis method [Kugiumtzis, 2004] [77] and visual recurrence analysis method [Kononov, 1999] [75], which are described below[see sec.4.5.2], to differentiate linear autocorrelated noise (or a stochastic process) from deterministic chaos. Another important observation we make is that the range of frequencies for which the exponential decay of powers occurs increases with increasing concentration. This implies that the rate at which 'loss of memory' of the system occurs increases with concentration.

That is,within a small interval of time, the system loses its information about the initial condition as concentration of particles increases. A comparison of the power specturm of both shear and normal stresses at a fixed area fraction of particles reveal that the range of frequency over which the fast expoenential decay of power spectrum occurs is almost the same. This important characteristic we observe for both the stress components at all area fraction of particles we considered.

We computed the autocorrelation function for both the stress components over the same range of particle concentrations. The figures (4.17) to (4.24) show plots of autocorrelation functions versus delay time for both stress components for the range of particle

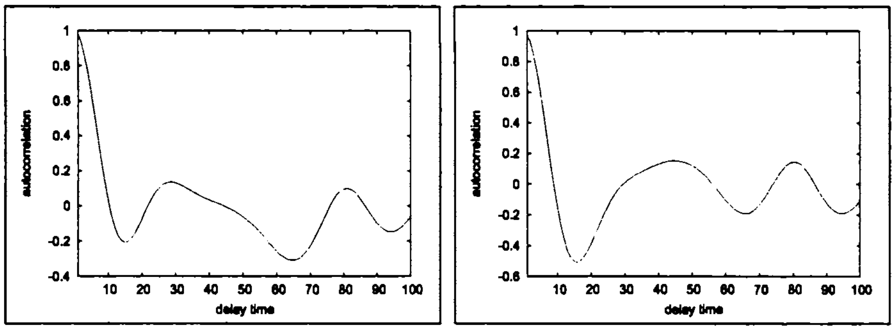

(a) (b)

Figure 4.17: Autocorrelation versus time delay for (a) shear stress σ_{xy} and (b) normal stress σ_{yy} at area fraction ϕ=0.05

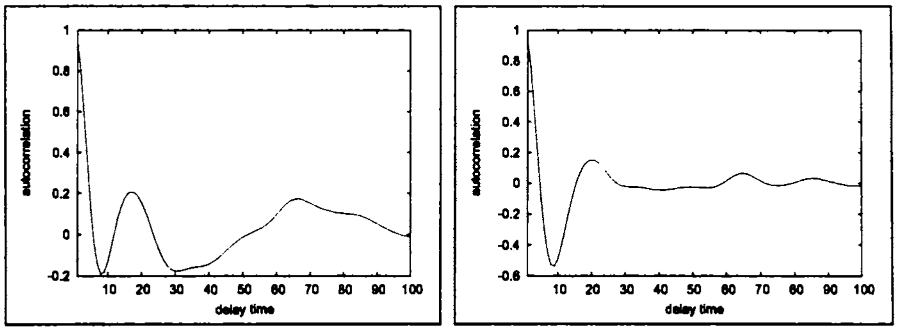

(a) (b)

Figure 4.18: Autocorrelation versus time delay for (a) shear stress σ_{xy} and (b) normal stress σ_{yy} at area fraction ϕ=0.10

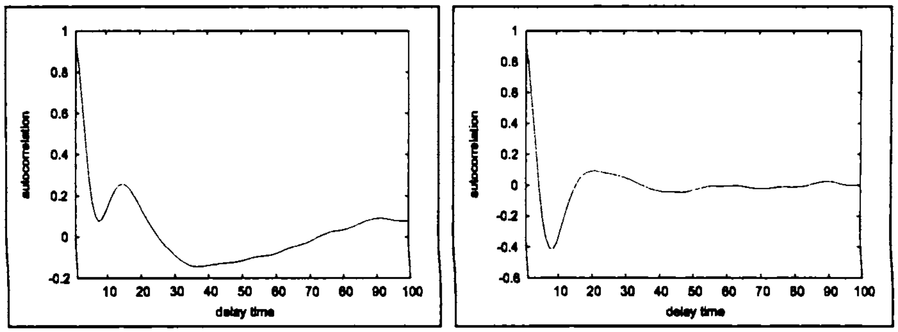

(a) (b)

Figure 4.19: Autocorrelation versus time delay for (a) shear stress σ_{xy} and (b) normal stress σ_{yy} at area fraction ϕ=0.20

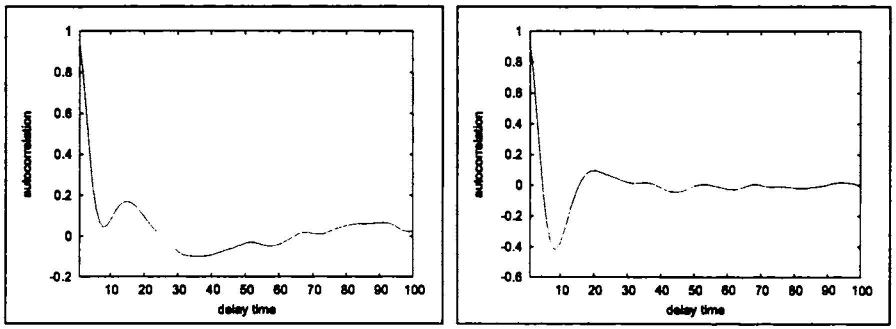

(a) (b)

Figure 4.20: Autocorrelation versus time delay for (a) shear stress σ_{xy} and (b) normal stress σ_{yy} at area fraction ϕ=0.30

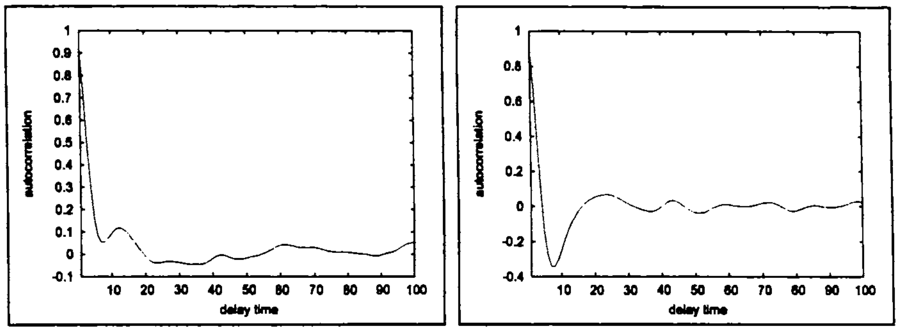

(a) (b)

Figure 4.21: Autocorrelation versus time delay for (a) shear stress σ_{xy} and (b) normal stress σ_{yy} at area fraction ϕ=0.40

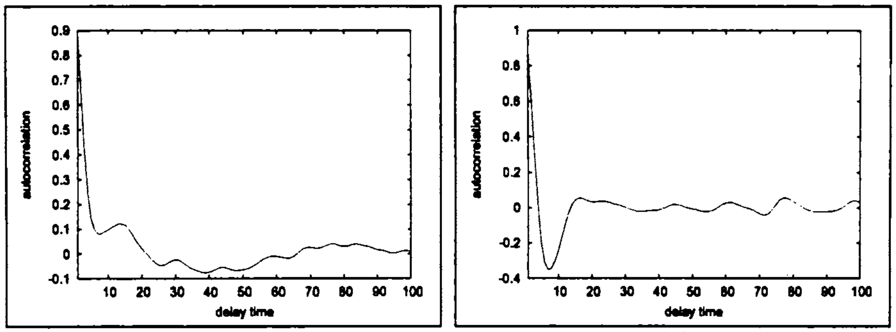

(a) (b)

Figure 4.22: Autocorrelation versus time delay for (a) shear stress σ_{xy} and (b) normal stress σ_{yy} at area fraction ϕ=0.45

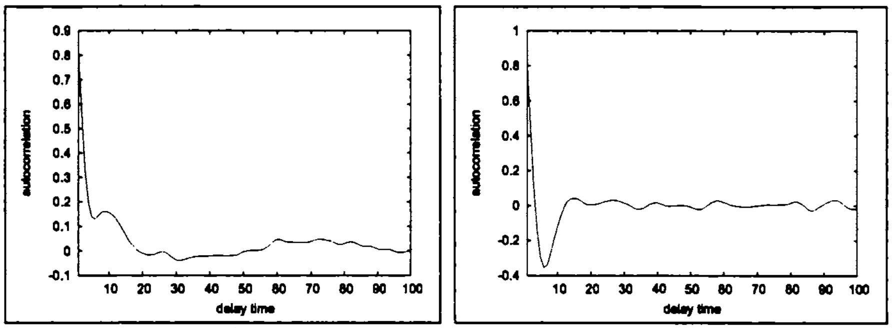

(a) (b)

Figure 4.23: Autocorrelation versus time delay for (a) shear stress σ_{xy} and (b) normal stress σ_{yy} at area fraction ϕ=0.50

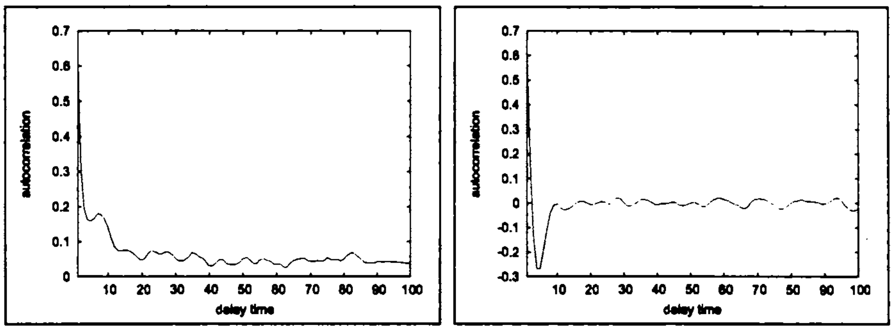

(a) (b)

Figure 4.24: Autocorrelation versus time delay for (a) shear stress σ_{xy} and (b) normal stress σ_{yy} at area fraction ϕ=0.60

concentrations $\phi = 0.05, 0.1, 0.2, 0.3, 0.4, 0.5$ and 0.6 at the Couette gap $H = 18$ particle width. We observe different local minima of autocorrelation function for different area fractions of particles. The Table (4.1) illustrates the different local minima we observed from the figures (4.17) to (4.24) for both the stress components.

ϕ	0.05	0.10	0.20	0.30	0.40	0.45	0.50	0.60
σ_{xy} or σ_{yy}	15	9	8	8	7	7	6	4

Table 4.1: Table shows the delay time at which autocorrelation function of the stress components σ_{xy} and σ_{yy} attain local minima as observed from figures (4.17) to (4.24).

The local minima attained by the autocorrelation function decreases with increase in

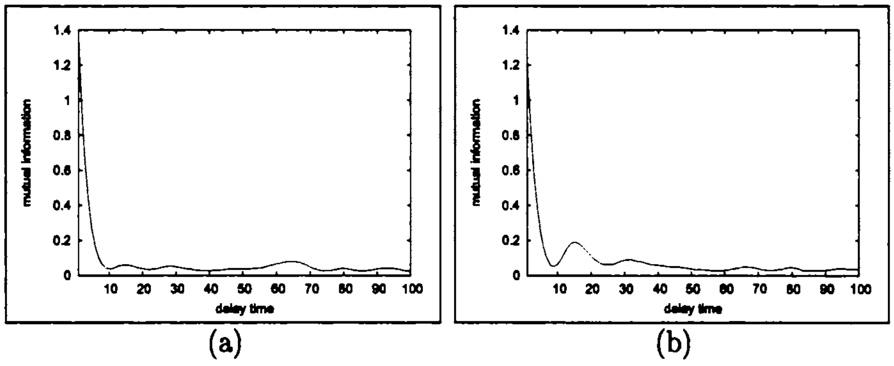

(a) (b)

Figure 4.25: Average mutual information versus time delay for (a) shear stress σ_{xy} and (b) normal stress σ_{yy} at area fraction ϕ=0.05.

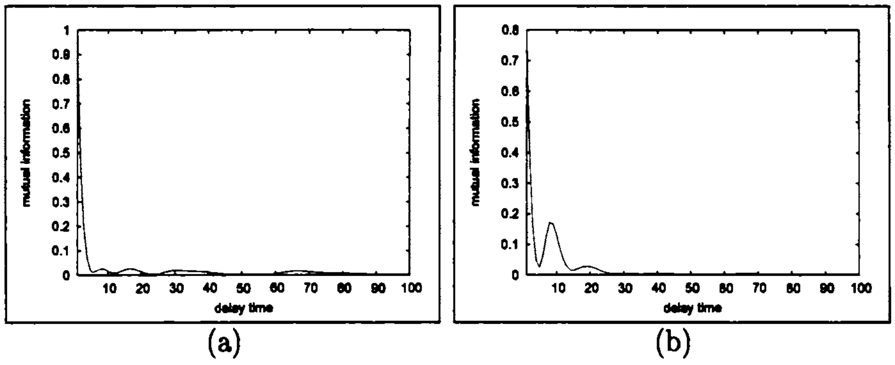

(a) (b)

Figure 4.26: Average mutual information versus time delay for (a) shear stress σ_{xy} and (b) normal stress σ_{yy} at area fraction ϕ=0.10

area fraction of particles in the suspension. That is, the lag time at which the system dynamics forgets information about the initial condition decreases as the concentration of suspension increases. In other words, the rate at which the system loses information about the previous state increases with increase in concentration of the particles in the suspension. We, also, observe that the local minima of the autocorrelation function for both stress components are the same for a fixed area fraction of particles. We observe this characteristic for both stress components at all area fractions of particles.

We have also computed the average mutual information for both the stress components at these area fractions of particles. The figures (4.25) to (4.32) plot average mutual

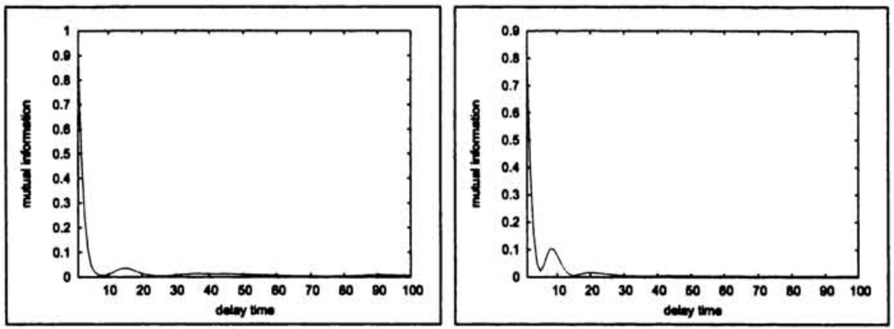

(a) (b)

Figure 4.27: Average mutual information versus time delay for (a) shear stress σ_{xy} and (b) normal stress σ_{yy} at area fraction ϕ=0.20.

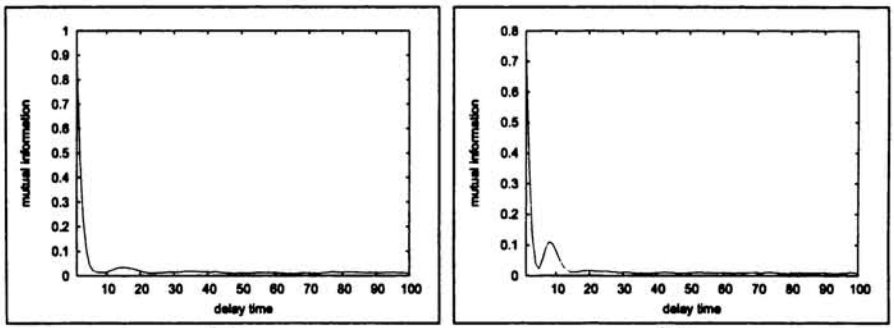

(a) (b)

Figure 4.28: Average mutual information versus time delay for (a) shear stress σ_{xy} and (b) normal stress σ_{yy} at area fraction ϕ=0.30

information versus delay for both the stress components at the above area fractions of particles. Here, we observe different local minima or zero of the average mutual information for different area fraction of particles.

The Table (4.2) illustrates the different local minima that we observe from the figures (4.25) to (4.32). Here, also, we observe the same trend that we noticed in the case of the autocorrelation function for the stress components in the Table (4.1). That is, the delay at which the average mutual information attains a local minima for the stress components decreases with increase in concentration of particles in the suspension. Again, we notice that the local minima of average mutual information for both the stress components

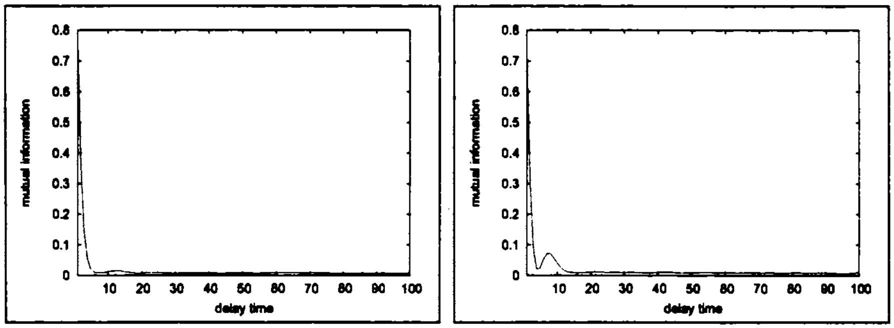

(a) (b)

Figure 4.29: Average mutual information versus time delay for (a) shear stress σ_{xy} and (b) normal stress σ_{yy} at area fraction ϕ=0.40.

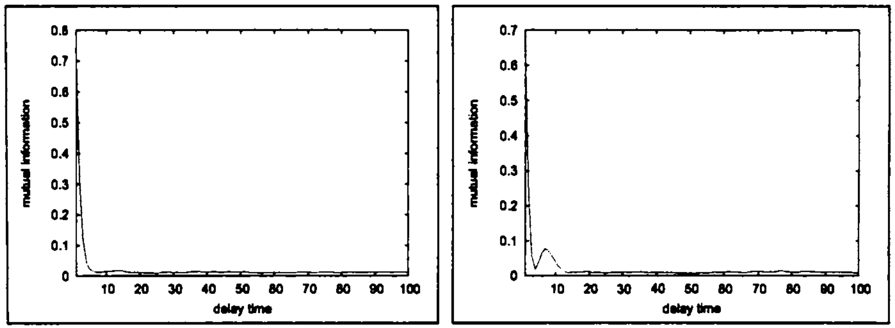

(a) (b)

Figure 4.30: Average mutual information versus time delay for (a) shear stress σ_{xy} and (b) normal stress σ_{yy} at area fraction ϕ=0.45

are almost the same for a fixed area fraction of particles. The slight difference may be attributed to the computational artefacts.

Along with these methods, we used the space-time separation plot [Provenzale *et al.*, 1992] [109] to analyse the suspension behavior. One differentiating characteristic of this method compared to the above two methods is the fact that it excludes temporal correlations of points in phase space. That is, pairs of points which are measured within a short time span tend to be close in phase space and this will adversely affect the computation of the correlation integral[see sec. 2.8.3]. We use the correlation integral to compute the effective dimension of the underlying attractor governing the dynamics which is in no

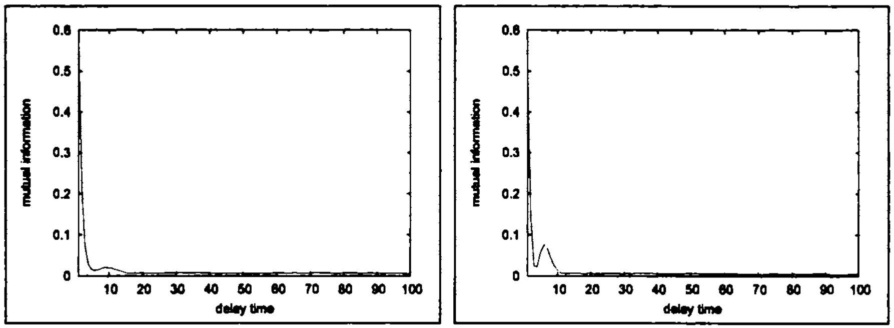

(a) (b)

Figure 4.31: Average mutual information versus time delay for (a) shear stress σ_{xy} and (b) normal stress σ_{yy} at area fraction ϕ=0.50.

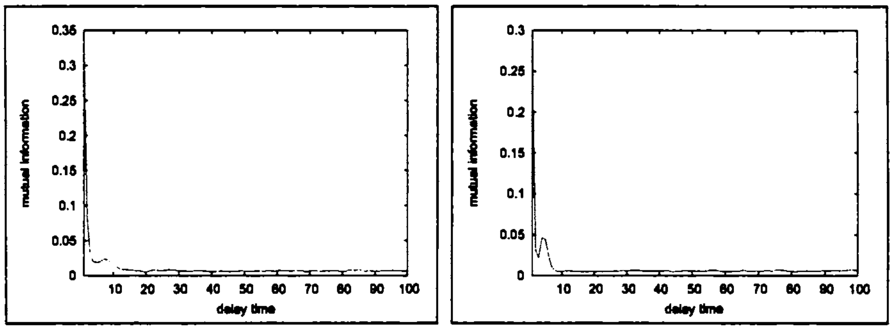

(a) (b)

Figure 4.32: Average mutual information versus time delay for (a) shear stress σ_{xy} and (b) normal stress σ_{yy} at area fraction ϕ=0.60

ϕ	0.05	0.10	0.20	0.30	0.40	0.45	0.50	0.60
σ_{xy}	10	6	7	6	6	6	5	3
σ_{yy}	9	5	6	5	5	5	4	3

Table 4.2: Table shows the delay time at which average mutual information function of the stress components σ_{xy} and σ_{yy} attain local minima as observed from figures (4.25) to (4.32)

way related to the closeness of points in phase space due to temporal correlation. The idea in a space-time separation plot is that in the presence of temporal correlations the probability that a given pair of points has a temporal correlation between a given pair of points depends both on the distance in space ϵ and on the time that has elapsed between the two measurements. This inter-dependence is determined by plotting the number of pairs of points as a function of the two variables, the time separation Δt and the spatial distance ϵ.

We performed the space-time separation analysis for both stress components. The figures (4.33) to (4.40) are the space-time separation plots of both the stress components for the area fractions of particles ϕ = 0.05, 0.10, 0.20, 0.30, 0.40, 0.45, 0.50 and 0.60 at Couette gap H = 18 particles width. In figures (4.33) to (4.40), contour lines are shown at the spatial distance ϵ where for a given temporal separation Δt, a fraction of 1/20, 2/20, ... of pairs are found. If we ignore two or three upper contour lines, we see saturation of these contour lines for all area fractions of particles. One of the uses of space-time separation plots is to check whether the system is stationary or not. A positive signature of stationarity is the saturation of the contour lines at some lag time [Kantz and Schreiber, 1997] [69]. We observe positive signatures of stationarity in the fluctuations of the stress components at all area fractions of particles we dealt with. The stress components attain saturation of the contour lines at different lag times for various area fractions of particles in the suspension. The Table (4.3) illustrates the approximate lag time at which contour lines of the space-time separation plots of the stress components attain saturation.

Here, also, we find that the lag time at which the system free itself from the nearness of points both in space and time decreases with increase in concentration. The analysis of the stress fluctuations using the three methods viz. autocorrelation function, average mutual information and space-time separation plots all reveal analogous conclusions about the

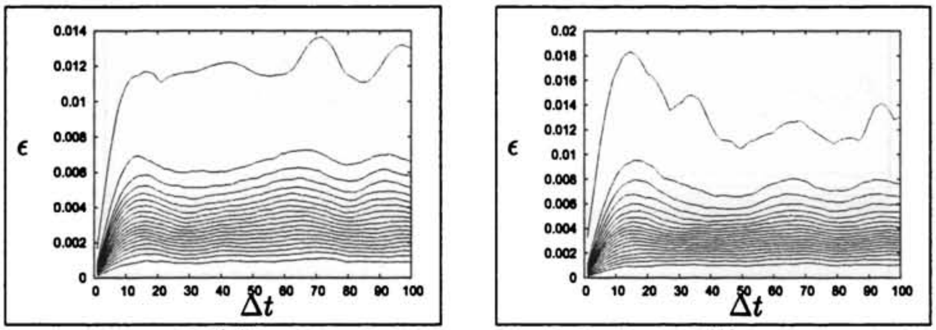

(a) (b)

Figure 4.33: Space-time separation plot for (a)shear stress σ_{xy} and (b)normal stress σ_{yy} at area fraction ϕ=0.05

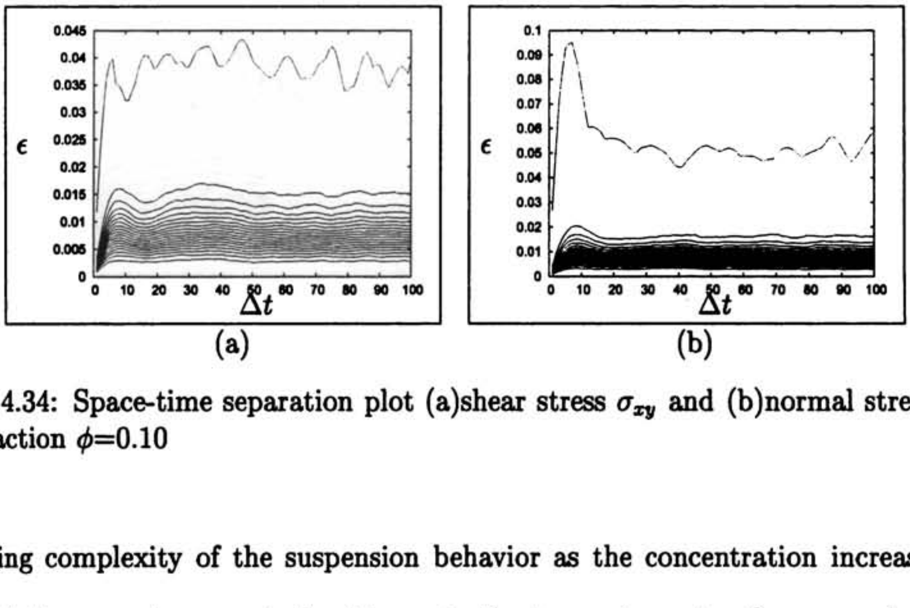

(a) (b)

Figure 4.34: Space-time separation plot (a)shear stress σ_{xy} and (b)normal stress σ_{yy} at area fraction ϕ=0.10

increasing complexity of the suspension behavior as the concentration increases. We, also, obtain concrete numerical evidence to the increasing rate of memory loss of the system dynamics with increase in concentration of the particles in the suspension. This directly indicates the microstructural change that is taking place in suspension due to the many-body interactions as the concentration increases.

One major use of the autocorrelation function, average mutual information and space-time separation plots is to find a reliable value of time delay for an efficient and reliable estimate of certain topological (geometrical) and dynamical invariants such as correlation dimension (geometrical invariant) and Lyapunov exponents (dynamical invariant) from time series. From the Tables (4.1) to (4.3), we get reliable values that can be regarded as a

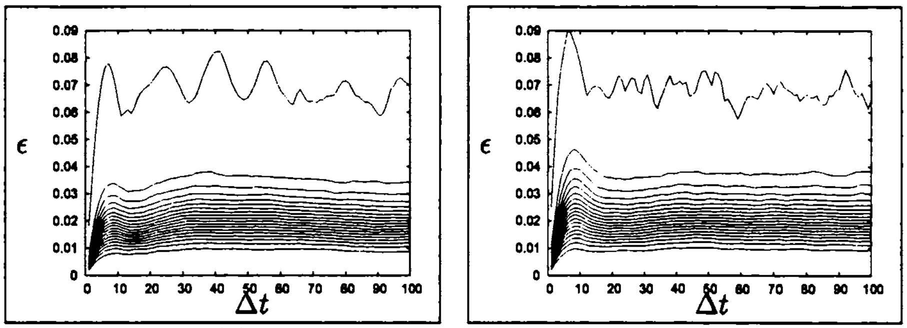

(a) (b)

Figure 4.35: Space-time separation plot for (a)shear stress σ_{xy} and (b)normal stress σ_{yy} at area fraction ϕ=0.20

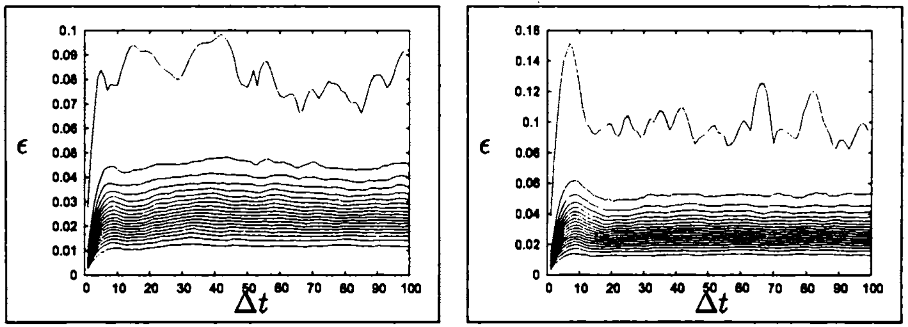

(a) (b)

Figure 4.36: Space-time separation plot for (a)shear stress σ_{xy} and (b)normal stress σ_{yy} at area fraction ϕ=0.30

fair estimate of the decorrelation time which will exclude the influence of successive points resulting temporal correlations due to nearness of points in space and time. Theoretically, any value as time delay is admissible, but in practice, due to limited accuracy and finite number of data points, a proper choice of time delay is needed for a reliable estimate of correlation dimension and Lyapunov exponent. The above methods should be taken as guidelines for proper choice of time delay. They are not hard and fast rules to estimate the correct value of time delay. From experience, we find that, space-time separation plot gives an upper bound for the choice of time delay. The average mutual information gives a value which is close to the optimum value of time delay.

The estimation of certain invariants viz. correlation dimension, Lyapunov exponents

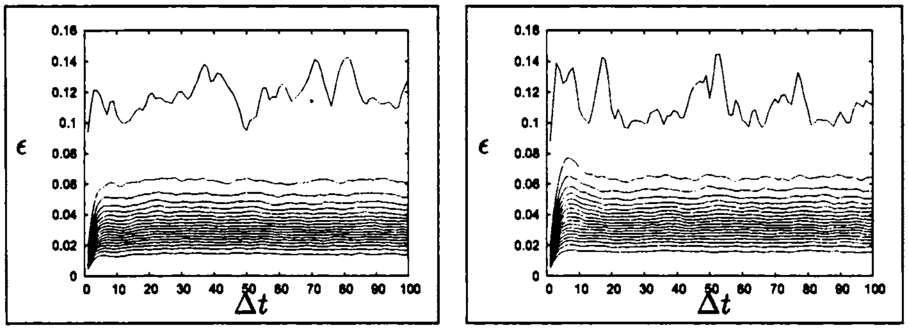

(a) (b)

Figure 4.37: Space-time separation plot for (a)shear stress σ_{xy} and (b)normal stress σ_{yy} at area fraction ϕ=0.40

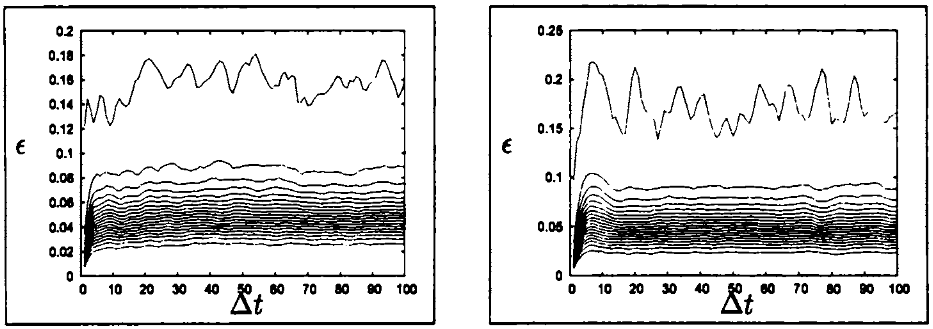

(a) (b)

Figure 4.38: Space-time separation plot for (a)shear stress σ_{xy} and (b)normal stress σ_{yy} at area fraction ϕ=0.45

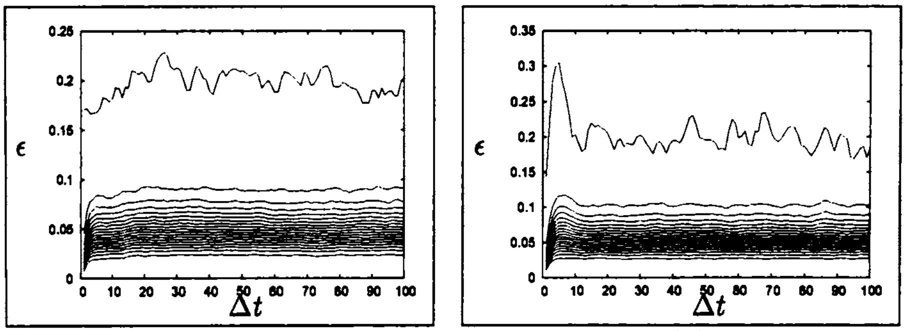

(a) (b)

Figure 4.39: Space-time separation plot for (a)shear stress σ_{xy} and (b)normal stress σ_{yy} at area fraction ϕ=0.50

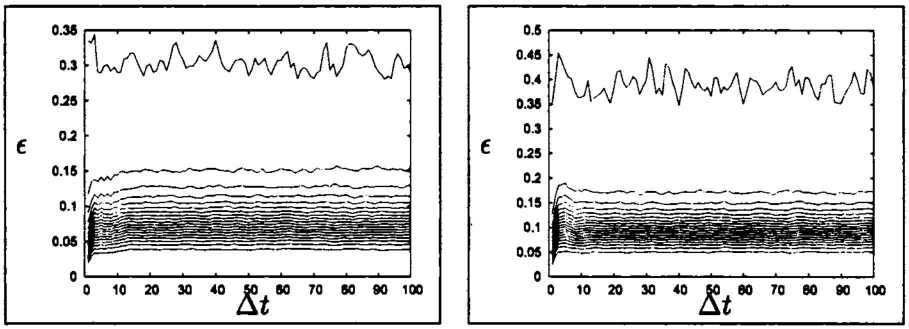

(a) (b)

Figure 4.40: Space-time separation plot for (a)shear stress σ_{xy} and (b)normal stress σ_{yy} at area fraction ϕ=0.60

etc. require a proper choice of Theiler's window ω [Theiler, 1995] [134], [Theiler, 1990] [133] which provides guidelines for proper sampling of points from a time series of data. [Theiler, 1995] [134] suggested that all pairs of points whose time indices differ by less than ω may be ignored, where $\omega \approx m\tau$, m being the embedding dimension and τ, the time lag that can estimated using guidelines from the analysis of autocorrelation function or average mutual information or space-time separation plots.

ϕ	0.05	0.10	0.20	0.30	0.40	0.45	0.50	0.60
σ_{xy}	35	25	23	20	15	18	13	13
σ_{yy}	30	17	17	17	15	15	12	9

Table 4.3: Table shows the approximate delay time at which the contour lines in the space-time separtion plots of the stress components σ_{xy} and σ_{yy} attains saturation as observed from figures (4.33) to (4.40)

For the computation of the correlation dimension, for instance, this requires the lower limit of j in (13) to be changed to $i+\omega$, and the factor multiplying the summation to be replaced by $2/N(N-\omega)$. Using the above information as a basis, we take the Theiler's window appropriately depending on the embedding dimension and time delay mainly for the estimation of certain invariant characteristics, mainly, Lyapunov exponent from the time series.

4.5.1 Low dimensionality of the attractor

In nonlinear time series analysis we are interested in characterizing the underlying attractor, a bounded limit set for typical initial conditions in some region of the phase space of the dynamical system. One of the parameters that characterizes an attractor is its dimension, which can be regarded as a measure of the amount of information necessary to specify the position of a point on the attractor within a given accuracy. For an accurate estimation of the attractor dimension, we use the *Principal component analysis* [Broomhead and King, 1986] [23], the *False nearest neighbor method* [Abarbanel, 1996] citeaba-96 and *the Grassberger-Procaccia algorithm* [Grassberger and Procaccia, 1983] [57].

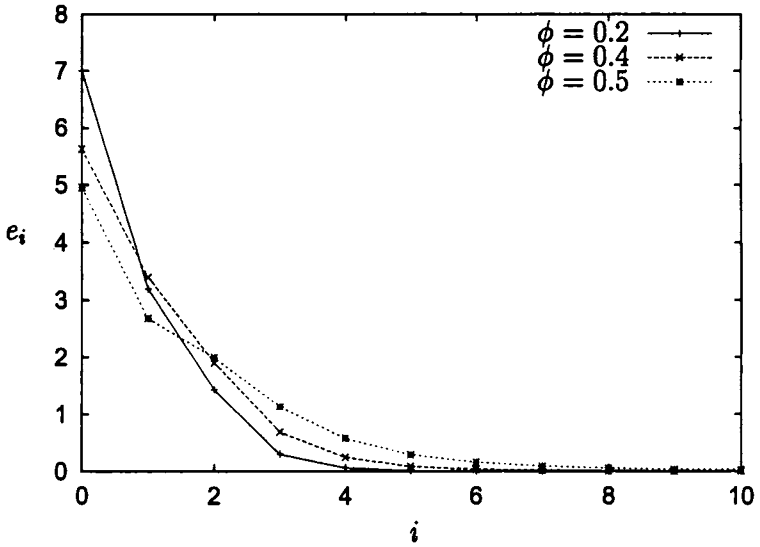

Figure 4.41: The eigenvalues versus dimension of the covariance matrix [Broomhead and King, 1986] [23] of shear stress σ_{xy} at area fractions $\phi = 0.2, 0.4, 0.5$ for H = 18.

Using the above guidelines to find proper time delay for embedding, we performed a principal component analysis (see sec.4.4) on the normal and shear stress components for different area fractions of particles. We get three significant eigen values when $\phi < 0.2$ and four or five significant eigenvalues for stress fluctuations measured from suspensions with area fraction $\phi = 0.2$, between five and seven values for stress components with area fractions ranging $0.2 < \phi < 0.5$ and seven and above significant eigenvalues for $\phi \geq 0.5$. We observe a monotonic increase in the number of significant eigen values for both the stress components with rise in concentration of particles in the suspension. The figure (4.41) illustrates principal eigenvalues obtained from a principal component analysis for the shear stress time series for three values of area fractions of particles $\phi = 0.2, 0.4, 0.5$.

As the number of significant (i.e. positive and greater than the noise floor) eigenvalues is an upper bound for the dimension of the attractor [Albano *et al.*, 1988] [5]; [Kantz and Schreiber, 1997] [69], this is a clear indication to the fact that there is a drastic change in the system microstructure and it becomes more and more complex if we take the number of independent coordinates required to capture the sytem dynamics as a measure of complexity of the system behavior. A principal component analysis on both the stress components at fixed area fraction of particles results in the same number of principal components (significant eigen values). Another important observation we make is that only a finite number (at most eight in number) of independent variables are sufficient to capture the dynamics of the rheological parameters viz. shear and normal stress components for the range of particle concentration $0.05 \leq \phi \leq 0.6$. This finding is likely to have significant impact in the processing of industrial suspensions as it reveals that to produce a product of the required quality we need to control only a finite number of factors where as the actual suspension dynamics is a consequence of an infinite number of factors.

The false nearest neighbor method, described in sec.4.4, shows that the dynamical behavior of the attractor can be described by three independent coordinates when the concentration of particles in the suspension is less than 0.2 and four or five independent coordinates are required to describe the fluctuations in stress components when the area fractions of particles lie in the range $2 \leq \phi < 0.4$. For stress components computed from suspensions with area fractions of particle $\phi = 0.4$ five or six independent coordinates are sufficient. For a suspension with area fraction of particles $0.4 < \phi \leq 0.6$, six to eight

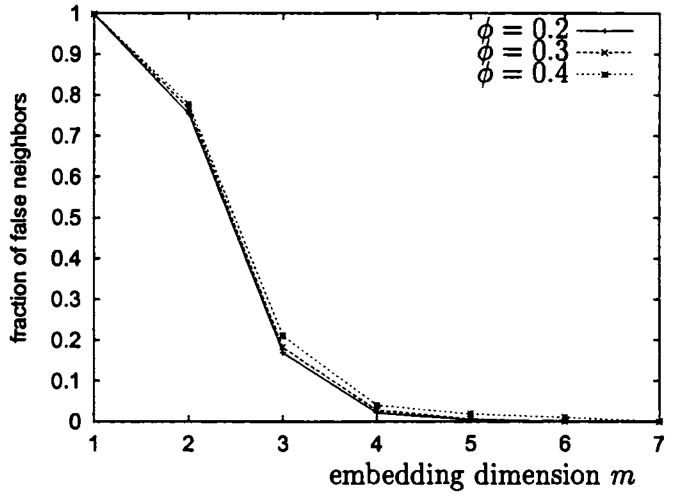

Figure 4.42: Fraction of false nearest neighbors as a function of the embedding dimension m for the σ_{xy} time series for area fraction $\phi = 0.2$, 0.3, 0.4 and $H = 18$.

independent coordinates are sufficient to describe the stress fluctuations. The figure (4.42) shows the plot of embedding dimension versus percentage of false nearest neighbors for shear stress fluctuations of suspension for area fractions particles $\phi = 0.20$, 0.30, 0.40 at the Couette gap $H = 18$ particles width. The increasing trend of the embedding dimension at which the percentage of false nearest neighbor reduces to zero is in agreement with what we observed in the principal component analysis. We, also, observed that, at a fixed area fraction of particles, the embedding dimensions at which the false nearest neighbors attains zero is the same. This is also in agreement with our findings using principal component analysis.

An estimate of the correlation dimension strengthens this conclusion. For an accurate estimation of the correlation dimension, we used the Grassberger-Procaccia algorithm [Grassberger and Procaccia, 1983]. We took 95000 data points of the time series of the normal and shear stresses, after deleting the initial transients, and computed the correlation integral for embedding dimensions ranging from 1 to 25 with a time delay $\tau = 17$. The figure (4.43) plots radius of the hypersphere versus correlation integral of the shear stress for area fractions of particles 0.2 at Couette gap $H = 18$ particles width. Each contour lines gives the correlation integral corresponding to embedding dimension varying from 1 to 25. We obtained a plateau region as r , radius of the hypersphere; varies from 0.27 to 0.37. This plot shows a plateau region for a range of values of r, the radius of the hypersphere, and the plateau region converges for higher embedding dimensions. Though the curves in this region converge to a constant value (approximately) for higher values of embedding dimension, we can observe local peaks in this region indicating absence of clear correlaton and so this method is only partially successful in yielding a positive result. We note, however, that this figure is typical of many in the literature.

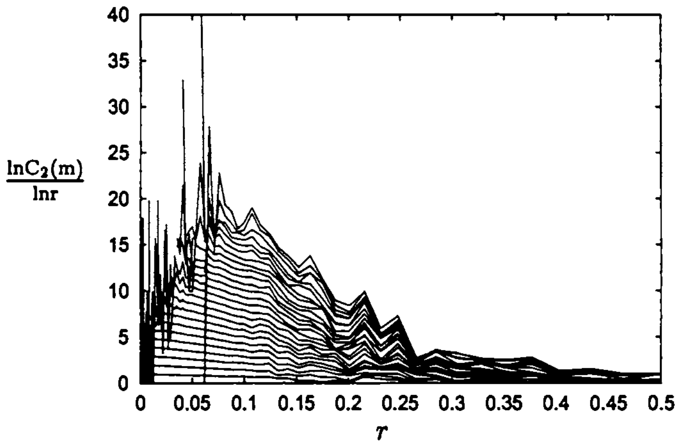

Figure 4.43: A typical plateau region showing approximate value of correlation dimension of the σ_{xy} time series, for $H = 18$ particle width and $\phi = 0.2$. The plateau region converges for higher embedding dimension indicating evidence for low-dimensionality of the attractor.

However, principal component analysis, false nearest neighbors method, nonlinear prediction method (discussed below) and the presence of structure in the three dimensional phase space plot point to a positive result. So the partial failure of correlation integral (correlation dimension) method should not be considered a major flaw in this analysis.

We can observe that the approximate plateau region converges to a constant value for high values of embedding dimensions for values of r ranging from 0.27 to 0.37 indicating the existence of low-dimensional attractor.

This plateau region shows that the attractor dimension lies between 2 and 4. We computed the correlation dimension of the normal and shear stresses for area fractions ϕ between 0.05 to 0.6 at the Couette gap $H = 18$ particles width. We obtained fractional correlation dimension for both the stress components for all area fractions of particles indicating the fractal nature of the attractor. In all cases we obtained a fractional correlation dimension indicating the existence of a low-dimensional strange attractor. The correlation dimension estimate of both the stress components for a range of particles concentration is tabulated in the Table (4.4). It is clear that the correlation dimension estimate of the stress components increases with increase in concentration. We, also, observe that for any given particle concentration the correlation dimension estimates for the normal and shear stress time series are quite close. These observations are in good agreement with our findings in the principal component analysis and false nearest neighbor method.

ϕ	σ_{xy}	σ_{yy}
0.2	3.2	3.4
0.4	4.1	4.2
0.5	4.8	4.3
0.6	5.5	5.5

Table 4.4: Correlation dimension D_2 determined from the time series of σ_{yy} and σ_{xy}, for $H = 18$ and a range of the area fraction ϕ. Note that the estimates of D_2 (with ± 0.062 to $\pm$ 0.098 variation) from the two stress components are quite close. Also note the increase in D_2 with particle concentration ϕ.

In high dimensional systems, the prediction of succeeding data points is a robust method for estimating the dimension of the underlying attractor. The embedding dimension at which the prediction error is a minimum is a good estimate of the dimension of the attractor. We used the locally constant predictor method (see sec.4.6) for predicting *one-step ahead* the successive fluctuations of the stresses. We used 13000 data points in the time-trace of the shear or normal stress to determine the structure of the underlying attractor, and predicted the evolution for nearly 35 succeeding dimensionless time steps. The figure (4.55) in sec.4.6 shows the prediction of successive fluctuations, using one-step ahead prediction method, of shear stress of the suspension at area fraction $\phi = 0.2$ and Couette gap $H = 18$ particle width. We then computed the normalized mean square error (NMSE) of prediction. We observed that for area fraction less than 0.4, the NMSE is minimum when the embedding dimension is 4 or atmost 5. Further evidence for low-dimensionality of attractor is discussed in the chapter on modeling. All these tests put together indicate strong evidence for the low dimensionality of the underlying attractor.

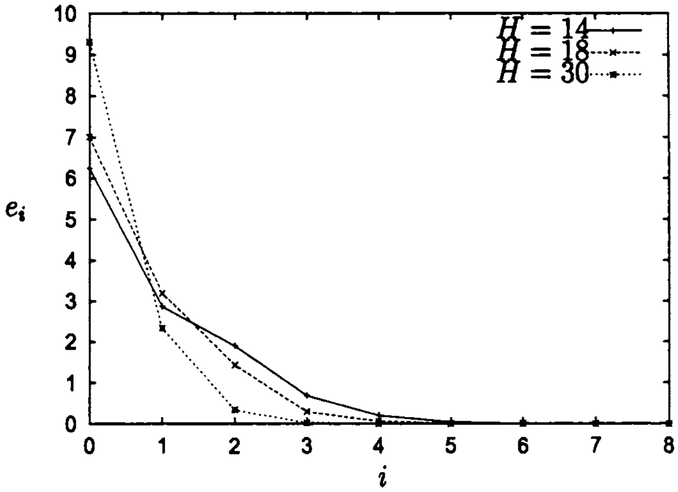

Figure 4.44: The eigenvalues versus dimension of the covariance matrix for the shear stress σ_{xy} for Couette gaps $H = 14, 18, 30$ at $\phi = 0.2$.

To study the influence of the Couette gap H on the invariant properties, we analyzed the time series of the stress components for $H = 14$, 18 and 30 for a fixed area fractions of particles $\phi = 0.20$. We computed the correlation dimension of the shear stress at

$\phi = 0.20$ for three Couette gaps H = 14, 18 and 30 particles width. The correlation for these Couette gaps is tabulated in Table (4.5). These computations reveal a slight decreasing trend in the correlation dimension as the Couette gap increases. We have also performed a principal component analysis on the stress components at these Couette gaps and the results are given in the figure (4.44). The finding is in agreement with what we observed in Table (4.5). The number of significant eigen values of the stress components at Couette gap H= 14 particle width is five or six, with Couette gap H = 18 particle width the number of significant eigen values become four or five and, with Couette gap H = 30 particle width the number of significant eigen values reduced to three or atmost 4. Thus, the principal component analysis is in agreement with what is observed in the correlation dimension analysis, which strengthens the conclusion that the complexity of the suspension behavior increases with the relative increase in the concentration of the particles in the suspension.

H	σ_{xy}	σ_{yy}
14	3.7	3.8
18	3.2	3.4
30	3.1	3.2

Table 4.5: Correlation dimension (with ±0.058 to ±0.087 variation) determined from time series of σ_{yy} and σ_{xy} for different Couette gaps, H = 14, 18 and 30 for $\phi = 0.2$. There is a slight decreasing trend in D_2 with increasing H.

To study the effect of inter-particle interaction in the suspension behavior, we estimated the correlation dimension for different values of μ, the range of the repulsive inter-particle interaction keeping $F_0\,\mu = 0.01$ a constant and chanaging the values of μ to 10, 100, and 1000 and correspondingly we change the value of F_0 to 10^{-3}, 10^{-4}, and10^{-5} for Couette gap of $H = 18$ at particle concentration $\phi = 0.4$. These results are tabulated in table (4.6); it is apparent that there is no significant variation in the correlation dimension with μ. That is, these variations in the repulsive inter-paricle interaction do not produce significant changes in the microstructure of the suspension.

4.5.2 Deterministic nature of the system

A finite length time series with broadband power spectrum may be a realization of a stochastic process governed by an autoregressive moving average model or of a low dimensional deterministic chaotic process [Eckman and Ruelle, 1985] [42]. Further, some geometrical or dynamical characteristics (low correlation dimension or positive Lyapunov exponent etc) of the low dimensional chaotic dynamics can be observed from particular linear stochastic dynamics. Hence, the analysis of a time series has to distinguish between linear stochastic and deterministic dynamics. We used both surrogate data analysis and the Visual Recurrence Analysis (VRA) method [Kononov, 1999] [75] to make this distinction. According to surrogate data analysis theory the geometrical and dynamical characteristics of a time series must be compared with those of stochastic signals which have the same power spectrum and amplitude distribution as the original data [Pavlos *et al.*, 1999a] [98], [Prick and Theiler, 1994] [108].

One surrogate of a time series which tests for linear stochastic processes is obtained by randomizing the phases of the Fourier coefficients of the time series. One takes an ensemble of surrogates of the time series for comparing with the original time series. In order to distinguish the nonlinear deterministic process from a linear stochastic process, we use a discriminating static Q defined by

$$Q = \frac{\mu_{obs} - \mu_{sur}}{\sigma_{sur}} \tag{4.12}$$

where μ_{obs} is a characteristic measured from the original time series, μ_{sur} is the average value of the same characteristic measured from the ensemble of surrogates and σ_{sur} is the standard deviation of the characteristic for the ensemble of surrogates. We computed the

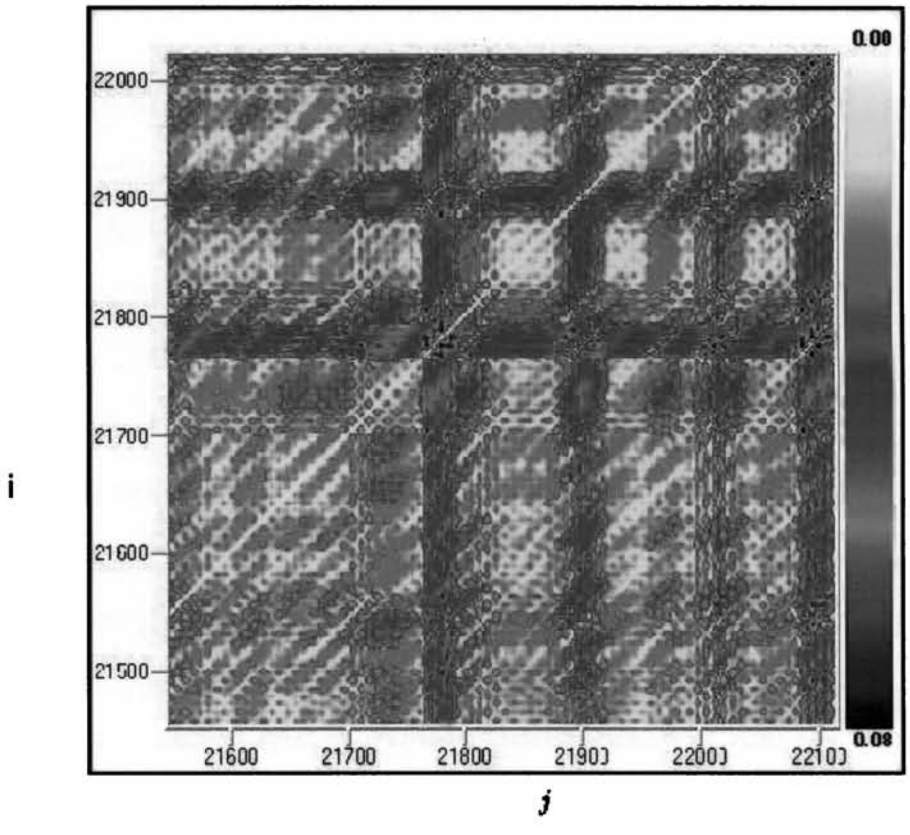

Figure 4.45: Recurrence plot for the shear stress σ_{xy} for $H = 18$ and $\phi = 0.2$. The definite structure in the plot is apparent; data with white noise will give a uniform distribution of color.

correlation dimension of ten sets of such phase shuffled time series for the shear and normal stresses. We found that $10 < Q < 15$, i.e. the correlation dimension of the original time series differs by 10 to 15 standard deviations from the mean correlation dimension of the ensemble of surrogates, clearly indicating that the differences is statistically significant. We also used the VRA method to determine the presence of structure in the stress fluctuations.

The importance of the recurrence plot, one of the tools available in VRA, is that the presence of structure can be visualized by means of color graphics. Once the dynamical system is reconstructed by means of delay coordinates, the distance between all pairs of vectors $x(i)$ and $x(j)$ are computed and various color codes are assigned to different distances. In a two dimensional recurrence plot, a color code at (i, j) position specifies the distance between the vectors $x(i)$ and $x(j)$. For random signals, a uniform distribution of colors over the entire plane is obtained and for deterministic signals we obtain coherent structures in the recurrence plot. This method demonstrated the existence of a coherent structure in the stress fluctuations in the suspension. The figure (4.45) is a (typical) recurrence plot for the shear (or normal) stress σ_{xy} of the suspension at area fraction of particles $\phi = 0.20$ and Couette gap $H = 18$ particle. The figures indicates the presence of deterministic structure in our system. For data with white noise, the recurrence plot will result in a uniform distribution of colors.

We also, computed the spatio-temporal entropy for the stress components. This quantity compares the distribution of colors over the entire recurrence plot with the distribution of colors over each diagonal line ($j = i + \text{const.}$) of the recurrence plot. The higher the combined differences [Peacock, 1983] [103] between the global distribution and the distributions over the individual diagonal lines, the more structured the image is. The small parallel off-diagonal lines, also, indicate the predictability of the system dynamics. However, the long term or short term predictability depends on other characteristic of the system, which we will explain in the next section.

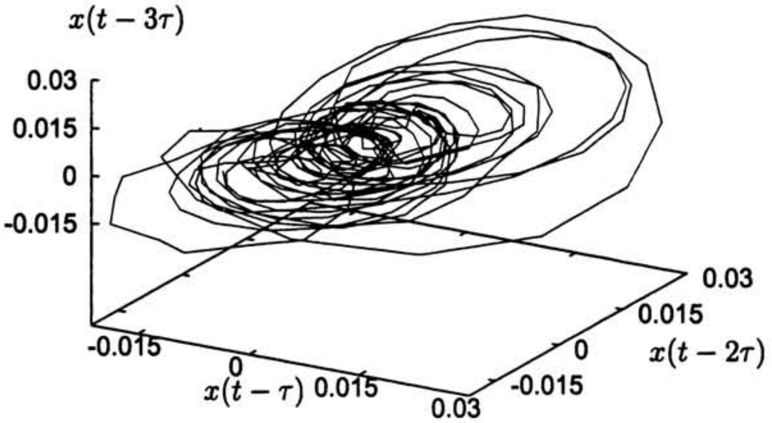

Figure 4.46: Phase space plot of the normal stress σ_{yy}, for $H = 18$ and $\phi = 0.2$.

In physical terms, this compares the distribution of distances between all pairs of vectors in the reconstructed state space with the distribution of distances between different orbits evolving in time (for details see [Carr and Schwart, 1998] [25]). For random signals the value of spatio-temporal entropy will be close to 100% and for deterministic signals the value will be considerably less. The calculated values of the spatio-temporal entropy for the shear and normal stresses were nearly zero showing almost perfect structure in the data. We observed definite structure in the phase space plot of the stress components. Figure (4.46) shows a typical phase space plot which is a three dimensional projection of the normal stress in four dimensions at area fraction $\phi = 0.4$. The predictability of the signal is also strong evidence for the deterministic nature of the system. From the above tests, we conclude that the fluctuations in the normal and shear stresses are due to a low-dimensional deterministic process.

4.5.3 Chaotic nature of the system

A striking behavior of many dynamical systems is their sensitive dependence on initial conditions, i.e. the divergence with time of trajectories from arbitrarily close initial conditions. An aperiodic bounded system having sensitive dependence on initial conditions is termed a **chaotic system**. To determine the existence of such behavior in our system, we computed the stress components viz. normal σ_{yy} and shear σ_{xy} stresses from a suspension of spheres in simple shear flow for two slightly different initial distribution of particles(the position of two suspended particles differed slightly in the two initial configurations) at different area fraction of particles in the Couette flow. The figure (4.47) shows the rapid divergence of two aribitrarily close trajectories of the shear stress for the two initial configurations, which differ in just one particle position, with area fraction of particle $\phi = 0.20$ and Couette gap $H = 18$ particle width. We computed the difference between the trajectories of the shear stress from the figure (4.47) and we observe an exponential increase in the difference of the two trajectories from figure (4.47). In figure (4.48), the logarithm of the difference $|x_t - y_t|$ (logarithm is taken after proper shifting to make the numbers positive) of the two shear stress time series in figure (4.47) against time

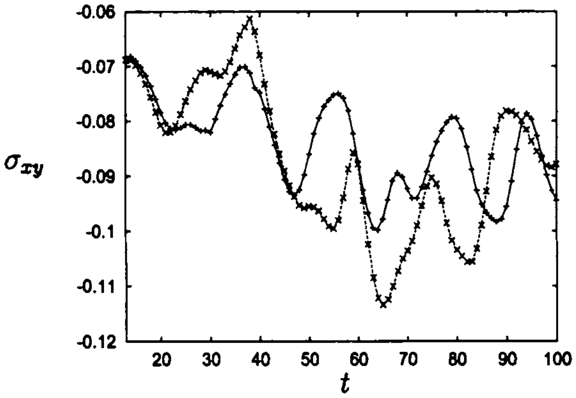

Figure 4.47: Divergence of close trajectories of the shear stress σ_{xy} for Couette gap H=18 and ϕ=0.2.

is plotted. Clear exponential increase is visible for small $t > 0$. This is a strong indication of the chaotic nature of the system dynamics. Computing this exponential divergence of arbitrarily close trajectories over a time interval is of great significance in analysing a time series obtained from a dynamical system. For a comprehensive characterization of the underlying attractor, we computed the maximum Lyapunov exponent (computation of the complete spectrum of Lyapunov exponents is tedious and requires a large amount of data), which measures the average rate of divergence or convergence of nearby orbits per iterate basis. The existence of a positive Lyapunov exponent is clear evidence for the chaotic nature of the system dynamics [Kantz and Schreiber, 1997] [69].

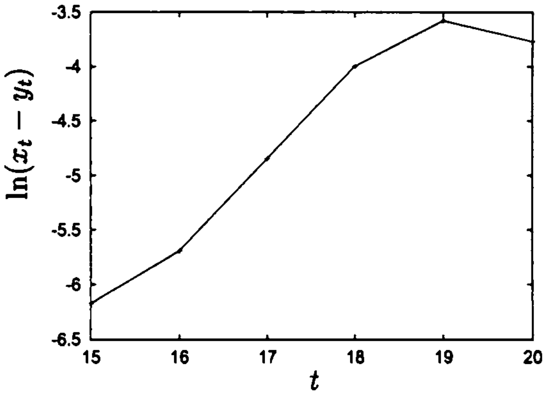

Figure 4.48: Logarithm of the difference $x_t - y_t$ of the time series in fig. 4.47 against t, showing clearly the exponential increase for small t in the difference between the stresses for the two trajectories, indicating chaotic nature of the system. Logarithm is taken after proper shifting of the values to make them positive.

Several methods have been reported in the literature for efficient and accurate estimation of Lyapunov exponents from time series. The first algorithm reported in the literature for estimating Lyapunov exponent from time series is suggested by [Wolf *et al.*, 1985] [138]. Wolf's algorithm uses only a delay reconstruction of phase space and it is not very robust and some times it results in a finite Lyapunov exponents for stochastic data. Another class of algorithms which make use of approximation of the underlying

μ	σ_{xy}	σ_{yy}
10	4.3	4.2
100	4.1	4.2
1000	4.2	4.1

Table 4.6: Correlation dimension determined from time series of σ_{yy} and σ_{xy} for different ranges of the inter-particle repulsive force, $\mu = 10$, 100 and 1000 (with $F_0\,\mu = 0.01$). The data are for $H = 18$ and $\phi = 0.4$. Note that D_2 (with ±0.052 to ±0.097 variation) is relatively insensitive to changes in μ.

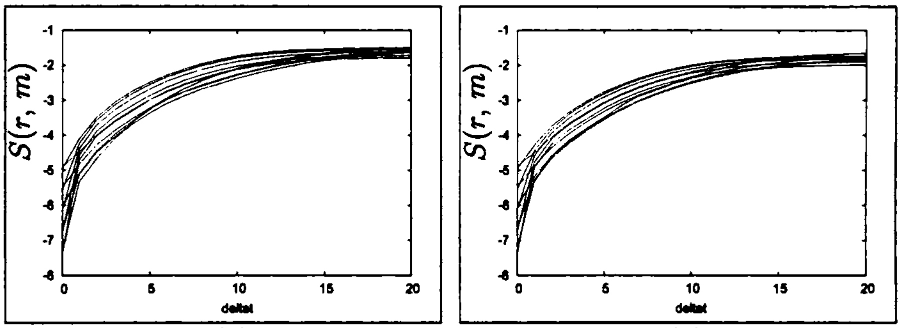

(a) (b)

Figure 4.49: The function $S(r, m, \Delta t)$ (see eqn. 4.13) versus Δt for various embedding dimensions for (a)shear stress σ_{xy} and (b)normal stress σ_{yy} for $H = 18$ at ϕ=0.05

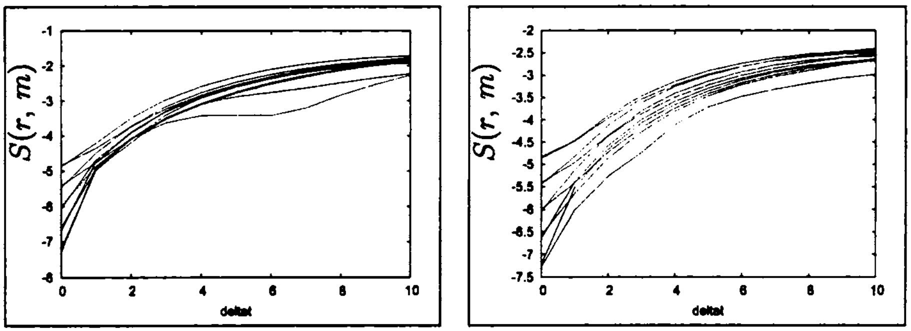

(a) (b)

Figure 4.50: The function $S(r, m, \Delta t)$ (see eqn. 4.13) versus Δt for various embedding dimensions for (a)shear stress σ_{xy} and (b)normal stress σ_{yy} for $H = 18$ at ϕ=0.10

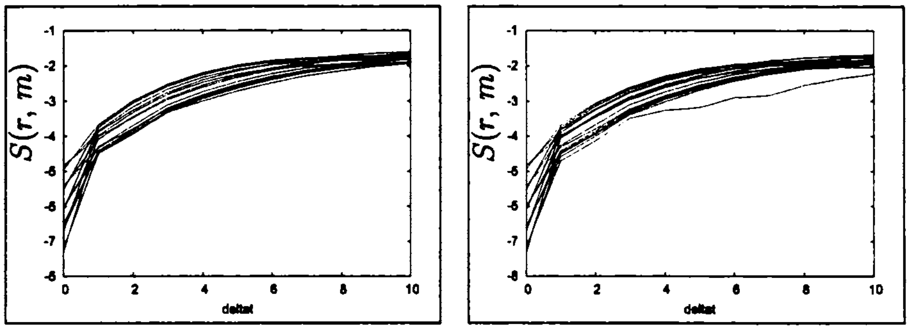

(a) (b)

Figure 4.51: The function $S(r, m, \Delta t)$ (see eqn. 4.13) versus Δt for various embedding dimensions for (a)shear stress σ_{xy} and (b)normal stress σ_{yy} for $H = 18$ at ϕ=0.20

deterministic dynamics are by [Sano and Sawada, 1985] [116] and [Eckmann *et al.*, 1986] [41]. This class of algorithms is very efficient and robust if the data allow for good approximation of the governing dynamics. Here we make use of the algorithm introduced by [Rosenstein *et al.*, 1993] [112] and independently by [Kantz, 1994] [70].

This algorithm tests directly for the exponential divergence of nearby trajectories and thus allows us to decide whether it really makes any sense to compute a Lyapunov exponent for a given data set. A time series, the image under a measurement function of the true state space, is a type of projection and so it may make distances apparently shrink apparently for short times, though they grow in the true state space. Also, in the true state space, distances do not grow everywhere on the attractor with the same rate, and locally they may even shrink. Thus, the Lyapunov exponent is an average of these local divergence rates over the whole data. Also, experimental data can be contaminated by noise and its influence can be minimized by using an appropriate averaging statistics when computing the exponent.

With the above guidelines for computing Lyapunov exponent, we consider the representation of the time series data as a trajectory in the embedding space with proper time delay. Then, we choose a point x_{n_0} in the embedded space and construct a neighborhood

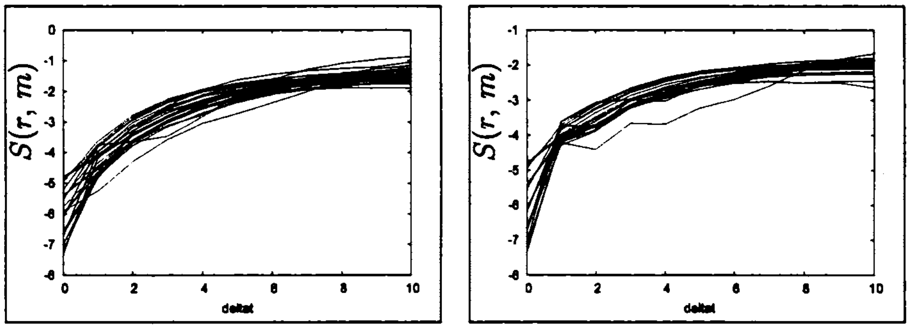

(a) (b)

Figure 4.52: The function $S(r, m, \Delta t)$ (see eqn. 4.13) versus Δt for various embedding dimensions for (a)shear stress σ_{xy} and (b)normal stress σ_{yy} for $H = 18$ at ϕ=0.30.

$\mathcal{U}_n$ with radius r and centre x_{n_0} in the embedded space. Then, we consider all neighbors or close returns x_n of the previously visited point x_{n_0} whose distances are less than r, then $\Delta_0 = x_{n_0} - x_n$ is a small perturbation. If one finds that its future $\Delta_t = x_{n_0+t} - x_{n+t}$ is given by $|\Delta_t| \approx \Delta_0 e^{\lambda t}$, then λ is the maximal Lyapunov exponent. Compute the average over the distances of all neighbors to the reference part of the trajectory as a function of the relative time Δt. The logarithm of the average distances at time Δt is an effective expansion rate over the time span Δt (plus logarithm of initial distance) containing all the deterministic fluctuations due to projection and dynamics. Using the Kantz method [Kantz, 1994][70]; [Kantz and Schreiber, 1997] [69], we compute

$$S(r\,,\,m\,,\Delta\,t) = \frac{1}{N}\sum_{n_0=1}^{N} \ln\left(\frac{1}{|\mathcal{U}(x_{t_0})|}\sum_{x_t \in \mathcal{U}(x_{t_0})} |x_{t_0+\Delta t} - x_{t+\Delta t}|\right) \tag{4.13}$$

for a point x_{t_0} of the time series in the embedded space, where $\mathcal{U}(x_{t_0})$ is the neighborhood of x_{t_0} with diameter r, $|\mathcal{U}(x_{t_0})|$ is the cardinality of the set $\mathcal{U}(x_{t_0})$. If $S(r\,,\,m\,,\,\Delta\,n)$ increases linearly with Δt for small Δt, with identical slope for all dimensions m larger than some m_c and for a reasonable range of r, then the slope can be taken as an estimate of the maximal Lyapunov exponent λ . Here the effective expansion rate over a time span is averaged for a range of values of t_0.

We computed the quantity in Eq. (4.13) and plotted against $\Delta\,t$ in the range $r =$

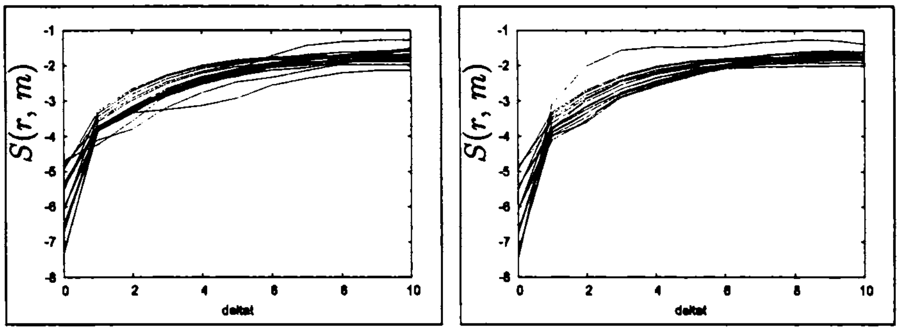

(a) (b)

Figure 4.53: The function $S(r, m, \Delta t)$ (see eqn. 4.13) versus Δt for various embedding dimensions for (a)shear stress σ_{xy} and (b)normal stress σ_{yy} for $H = 18$ at ϕ=0.40.

1.069255×10^{-04}, 1.901435×10^{-04}, 3.381282×10^{-04}, 6.012865×10^{-04}, 1.069255×10^{-03} for both the stress components σ_{xy} and σ_{yy} for different area fractions of particles in the range $\phi = 0.05, 0.10, 0.20, 0.30, 0.40$,. The figures (4.49) to (4.53) show plots of $S(r\,, m)$ versus $\Delta\, t$. We observe separate identical slopes for stress fluctuations at each of the area fractions $\phi = 0.05, 0.10, 0.20$ and these slopes are roughly independent of the embedding dimension for embedding dimension greater than three for $\phi < 0.20$ and greater than four for $\phi = 0.2$. For stress components of suspension with area fractions $\phi = 0.30$ and 0.40, we get separate identical slopes for embedding dimension above five for $\phi = 0.30$ and above five or six for $\phi = 0.40$. We estimated these slopes for different embedding dimension and for different t_0.

The approximate average values of these slopes (Lyapunov exponent) of both shear and normal stresses are tabulated in the Table (4.7) for different area fractions of particles in the range $\phi = 0.05, 0.10, 0.20, 0.30, 0.40$ and 0.50. It is easy to observe from the Table (4.7) that the value of $S(r\,, m\,, \Delta\, t)$ increases linearly with Δt. Thus, in all the area fractions of particles, the underlying attractor of the stress components show exponential divergence of nearby trajectories. Also, we observe an increasing trend in the Lyapunov exponent of the stress components with rise in concentration and for a fixed area fraction of particles both the stress components give roughly the same estimate for the Lyapunov exponent.

ϕ	σ_{xy}	σ_{yy}
0.05	0.23	0.25
0.1	0.31	0.35
0.2	0.43	0.44
0.3	0.50	0.45
0.4	0.53	0.52
0.5	0.60	0.57

Table 4.7: The maximum Lyapunov exponent for the σ_{yy} and σ_{xy} time series, for $H = 18$ and various particle concentrations ϕ. The Lyapunov exponent increases with ϕ, implying that the system is more chaotic when the particle concentration is increased.

The general trend of a rise in the maximum Lyapunov exponent with ϕ is apparent. This increase in the Lyapunov exponent is strong indication of many particle interactions leading to chaotic behavior. We obtained numerical evidence for the presence of a chaotic attractor in the system even for the smallest area fraction of particles we considered. We also computed the entropy of the system, which indicates the chaotic nature of the system, defined in the following manner: If the system is embedded in m-dimensional space with delay τ, then the m dependence of the correlation integral $C_q(r, m)$ of order q for large m can be expressed [Schreiber, 1999] [119]; [Grassberger and Procaccia,1983] [56]; [Ott *et al.*, 1994] [95] as

$$C_q(r,m) = \alpha(m)\, e^{-(q-1)\,h_q\,\tau m}\; r^{(q-1)\,D_q} \tag{4.14}$$

as $r \to 0$ and $m \to \infty$, where h_q is called the q -th order entropy. Computing the entropy for $q = 2$ is the easiest, and it can be performed along with the computation of the correlation dimension D_2. Our calculations show that the entropy, which is always less than or equal to the sum of the positive Lyapunov exponents, is positive for all particle concentrations.

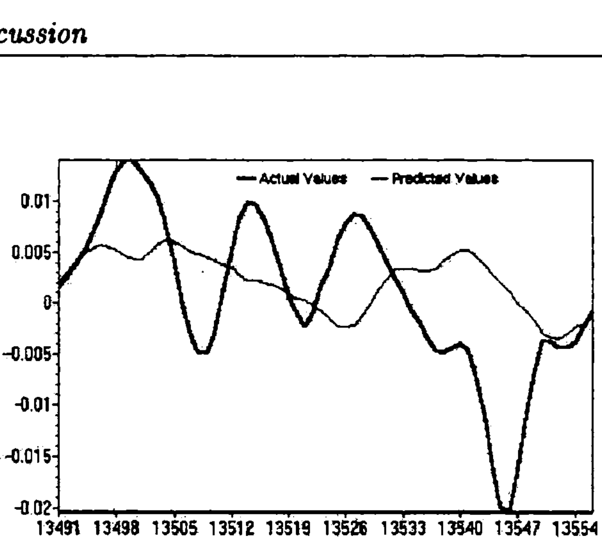

Figure 4.54: Multi-step predictions of the normal stress σ_{yy} for $H = 18$ particle width and $\phi = 0.2$. Exponential divergence of the predicted value from the actual value is clearly visible

Further evidence of chaos is provided by the one-step ahead and multi-step ahead predictions of successive fluctuations of the stresses (see sec.4.6). While the one-step ahead successive prediction is quite accurate up to nearly 35 time-steps in the future (4.55), the multi-step ahead prediction diverges from the actual time-trace after 3-5 time units (see fig.(4.54)). This apparent distinction between the two predictions is a clear indication of the sensitive dependence on initial conditions of nearby trajectories. With these strong and concrete evidences of the chaotic nature of the rheological parameters, the exponential decay of the power spectrum (see figs. (4.9) to (4.16)), which a common characteristic of both deterministic chaos and linear stochastic signals, of these parameters indicate the chaotic nature of the signal.

Given all the above evidence, we conclude that the attractor underlying the fluctuations in the stress has a fractional correlation dimension, and is a consequence of low-dimensional chaotic dynamics.

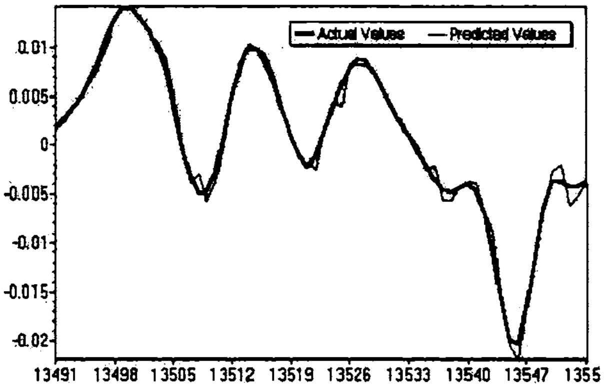

Figure 4.55: One-step predictions of the normal stress σ_{yy} for $H = 18$ particle width and $\phi = 0.2$. Note the close agreement of the predicted value with the actual value

4.6 Prediction of successive fluctuations

An important feature of chaotic systems is their exponential sensitivity to initial conditions: the average error made when forecasting the outcome of a future measurement increases exponentially with time. The length of the period over which accurate short term predictions of the successive fluctuations of the signal is possible is determined by the accuracy of the initial conditions and estimate of the Lyapunov exponent and if we get a local model which is better that than the one obtained using probablistic or global model it is reasonable to assume that there is a deterministic mechanism which governs the process under study, providing in this a tentative crieterion to discriminate between chaos and noise [Sugihara and May, 1990] [130], [Rubin, 1992] [114], [Ikeguchi and Ahara, 1997] [64], [Barahona and Chi-Sang Poon, 1996] [13]. We use local models to predict [Xiaofeng and Lai, 1999] [139] the one-step and multi-step procedures. That is, instead of fitting one complex model with many coefficients to the entire data set, we fit many simple models (low order polynomials) to small portions of the data set depending on the geometry of the local neighborhood of the dynamical system. The general procedure is the following: the last known state of the system, represented by a vector $\boldsymbol{x} = [x(n), x(n+\tau), \ldots, x(n+(m-1)\tau)]$, is determined, where m is the embedding dimension and τ is the time delay. Then p close states (usually nearest neighbors of $\boldsymbol{x}$) of the system that have occurred in the past are found, by computing their distances from $\boldsymbol{x}$. The idea then is to fit a map which extrapolates $\boldsymbol{x}$ and its p nearest neighbors to determine the next values. Using this map an approximate value of $x(n+1)$ can be estimated. We use both *one-step* and *multi-step head prediction* methods. In the one-step prediction, after each step in the future is predicted, the actual value is utilized for the next one-step prediction; in contrast, the multi-step prediction is based only on the initial p states. The Normalized Mean Squared Error (NMSE), referred to in §4.5.1, is computed by comparing the mean square error (between data and prediction) of the above method with MSE of the unconditional mean predictor method (a trivial method which predicts the average of the observed values as the subsequent value). As stated in sec.4.5.1, we observed that the NMSE is minimum when m is between 3 and 4 for ϕ less than 0.4, and roughly 5 for ϕ between 0.4 and 0.5 and is above 5 for ϕ greater than 0.5.

From the time-series of the stresses up to a given time t_0, we predicted their subsequent evolution (i.e. the multi-step prediction) using the locally constant predictor (in VRA see [75]). A good prediction is possible only up to $t = t_0 + 3$, as shown in fig.(4.54). In contrast, the one-step prediction [Kononov, 1999] [75] of successive fluctuations of the stress is quite accurate up to 35 time units in the future (see fig. (4.55)).

4.7 Cross prediction of the time series

Cross-prediction of one time series from the time series of another related variable was introduced recently by [Abarbanel *et al.*, 1998] [1]. This technique has potential application in situations where the measurement of one quantity is difficult or expensive, while the measurement of a related variable is easy or inexpensive. In such a case, simultaneous measurements of both variables need to be made for a baseline period, and then the easily measured variable can be used to predict the other. The cross-prediction of a signal (response signal) $y(t)$ from another signal (drive signal) $x(t)$ implies the existence of a functional relation Ψ such that $y(t) = \Psi(x(t))$. One significance of this technique is that the prediction of one variable from another can be made without knowing the properties of Ψ. When the phase space points of the driving and response systems are connected by such a functional relation Ψ, two nearby states in the phase space of the driving system correspond to two nearby states in the phase space of the response system. This property of a pair of such systems can be characterized by the mutual false nearest neighbors (MFNN) parameter [Abarbanel, 1996] [2].

For systems preserving this identity of neighbors in state space, the value of the parameter will be close to unity [Abarbanel *et al.*, 1998] [1]. We computed the MFNN for the shear and normal stresses and found that it was close to unity at almost all the points in the phase space. We used the nearest neighbor method [Hegger *et al.*, 1999] [60] of the TISEAN package to cross-predict the fluctuations in the normal (shear) stresses from the fluctuations in the shear (normal) stresses of the suspension with the proper time delay and embedding dimension obtained from previous analysis. We performed the cross-prediction for different area fractions of particles and the figures (4.56) to (4.57)show the cross-prediction of the normal stresses σ_{xx}, σ_{yy}, σ_{yy} at area fractions $\phi = 0.20, 0.20, 0.40$ from the correposding shear stresses respectively. We observed that the cross-prediction deteriorates with rise in concentration (area fraction) of particles in the suspension in both shear and normal stresses. This can be attributed to increasing trend in the Lyapunov exponent. As we already observed, the increasing trend of Lyapunov exponent is a consequence of frequent many-body interactions taking place in the suspension as concentration increases. The above observation shows that many-body particle interaction is responsible for the deterioration in the cross-prediction of one stress component

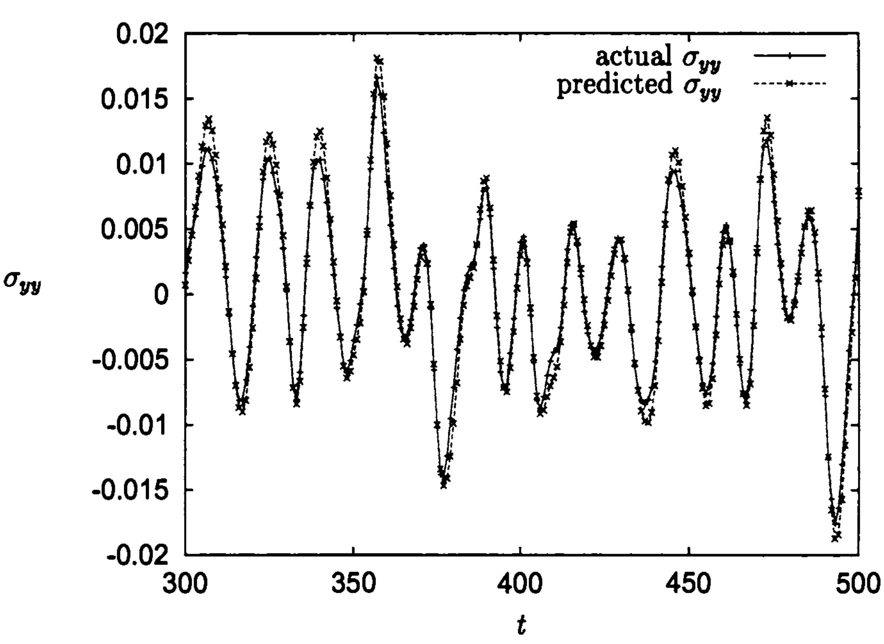

Figure 4.56: Cross-prediction of normal stress σ_{yy} from shear stress σ_{xy} at area fraction $\phi = 0.20$ and Couette gap $H = 18$ particle width.

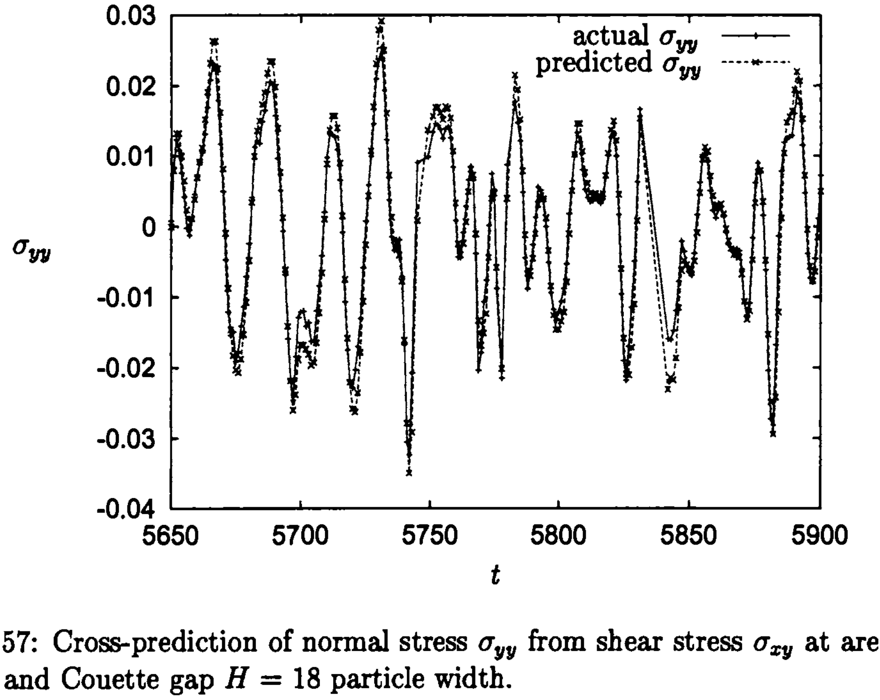

Figure 4.57: Cross-prediction of normal stress σ_{yy} from shear stress σ_{xy} at area fraction $\phi = 0.40$ and Couette gap $H = 18$ particle width.

from the other stress component. The ability to cross-predict one stress component from the other stress component, indicates the existence of a functional relationship between the stress component. Frequent many-body interactions appear to weaken the functional relationship between the different stress components. Hence, we anticipate that there will be a stage, as the area fraction increases, at which the different stress components will have no functional relationship with each other. If we look at these observations from a macroscopic level, there will reach a stage at which the whole system evolution will be governed by randomness.

4.8 Discussion

We have analyzed, using the tools of nonlinear dynamics and chaos theory, the fluctuations in the rheological parameters viz. the shear and normal stresses developed when a neutrally buoyant non-Brownian Stokesian suspension of identitical speheres is subjected to simple shear flow in the regime of vanishingly small Reynolds number. We have found numerical evidence for the existence of a low dimensional deterministic chaotic attractor governing dynamics of the fluctuations in the stress components for particle area fraction ϕ in the range 0.05 to 0.6. We obtained this non-trivial conclusion using the tools of nonlinear dynamics and chaos theory. The main tools we used are (a) autocorrelation function, (b) average mutual information, (c) space-time separation plot, (d) power spectrum (Fourier series analysis), (e) Principal component analysis, (f) False nearest neighbor method, (g) correlation integral method, (h) Surrogate data analysis, (i) Visual recurrence analysis, (j)prediction methods (both one-step ahead prediction and multi-step ahead prediction methods) and (k) computation of the Lyapunov exponent. We used the autocorrelation function, average mutual information, and space-time separation methods to obtain a guideline for estimating optimal time delay to make a robust and reliable estimate of the embedding dimension (correlation dimension). With proper optimal time delay, we used the principal component analysis, false nearest neighbor method, correlation integral method, prediction method and modeling method [see chap. 5] to establish the low-dimensional nature of the underlying attractor. To disprove the fact that the attractor is not an artefact of linear autocorrelated noise or some stochastic process (and hence to prove the deterministic nature of the attractor), we used visual recurrence analysis, surrogate data analysis and the prediction method. Thus, with a combined application of these methods, we established the low-dimenional and deterministic nature of the underlying attractor governing the stress fluctuations.

Next, we provided evidence to the chaotic nature of the attractor. For this, we computed the Lyapunov exponent, a measure of the rate at which arbitrarily close trajectories diverge from each other, and found that for all the area fractions of particles in the range $0.05 \leq \phi \leq 0.6$ the Lyapunov exponent is positive indicating the chaotic nature of the attractor. Thus, we numerically established that underlying attractor of the rheological parameters is low-dimensional, deterministic and chaotic. The fact that the attractor is low-dimensional and chaotic implies that though the system behavior is erratic and long term prediction is impossible, due to the exponential divergence of arbitrarily close trajectories, meaningful short term predictions can be performed with desired accuracy. We used this information about the underlying deterministic and chaotic structure in the fluctuations to make short-range predictions of the shear and normal stresses for different area fraction of particles.

The analysis of the simulated stress fluctuations using autocorrelation function [4.3.1], average mutual information [4.3.2] and space-time separation plot [4.3.3] reveals that the rate at which dynamics of the system loses its information (memory) about the previous (or initial) stress fluctuations increases with increasing concentration (area fraction) of the particles. The rapid loss of information is due to the increasing particle-particle and other many-body hydrodynamic interactions frequently occurring in the suspension. The figures (4.17) to (4.24) of the autocorrelation function, (4.25) to (4.32) of the average mutual information and (4.33) to (4.40) of the space-time separation plots for the stress components for different area fraction of particles over the range $0 \leq \phi \leq 60$ reveals a sustained and regular increase in the rate of loss of information of the system dynamics as the concentration (area fraction) of the particles increases. This sustained regular increase in loss of information in the stress fluctuations is due to the increasing chaotic nature of the system dynamics. Contemporary to our work [Dasan *et al.*, 2002] [32], [Drazer *et al.*, 2002] [35] investigated the velocity profiles of this system. They claim that the chaotic motion is resposible for the loss of correlation in phase space of the velocity field. The loss of memory at the microscopic level of individual particles is also shown in terms of the autocorrelation function for the two tranverse velocity components. In Stokesian suspensions, stress is a product of the fluid viscosity, the shear rate and a function of microstructure. Since we apply a constant force to create shear in the suspension, the scaled stress fluctuation is directly connected to a function of the microstructure. The stress fluctuations is hence mostly determined by the microstructure of the suspension. This shows that the chaotic motion of the particles (a microscopic property of the system) is responsible for the chaotic nature of the stress fluctuations (a macroscopic property of the system). Analysis of coupled map lattices are a means to determine the qualitative behavior of spatial averages (viz. stresses) of individual chaotic oscillators [Roy and Amritkar, 1997] [113], [Bunimovich and Jiang, 1997] [24]. Failure of the *law of large numbers* for weakly coupled map lattices of chaotic oscillators is observed in the literature [Sinha, 1992] [125]. We observe that the chaotic nature of the stress fluctuations (which is a macroscopic property of the system) is due to the chaotic motion (a microscopic property of the system) of the individual particles (chaotic oscillators) where motion is coupled to each other's motion and position through hydrodynamic interaction. Comparing our simulations to a typical globally coupled map lattice, we note that the relative particle positions in our simulations correspond to the values attained by individual chaotic oscillators in a coupled map lattice, and the coupling between any two particles is a chaotic function of the difference in positions between any two particles. As the stress measured from the system is a macroscopic property of the system, in this system we observe the failure of *the law of large numbers*.

Recently [Drazer *et al.*, 2004] [36] analysed the system for the connection between velocity fluctuations and microstructure of the suspension using Stokesian Dynamic simulations. Drazer *et al.*[2004] [36] observed that the standard deviation of the velocity fluctuations is directly proportional to the volume fraction of the particles in the dilute limit upto 10% of concentration of particles in the suspension.

Estimation of the embedding dimension (using principal component analysis, false-nearest neighbor method, correlation integral method) in our simulation revealed that for a fixed area fraction of particles both the stress components viz. shear stress and normal stress give almost the same value for the estimates in all the three cases. This observation is strengthened by the prediction method as both components yield good prediction of the future values at almost the same embedding dimension. This finding hints at the possibility of a functional relationship between the different stress components. We confirmed this abstract finding by computing the mutual false-nearest neighbor parameter for the stress components and we found that the computed value is close to unity at almost all the points in the embedded phase space indicating the existence of a functional relationship between the stress compoents at all the area fractions of particles. Taking advantage of this fact, we predicted one stress component from another stress component. We observed that the accuracy of cross-prediction deteriorates with increase in concentration. This is an expected consequence of the increasing Lyapunov exponent of the stress fluctuations with increase in area fraction of particles in the suspension. The rise in the correlation dimension and Lyapunov exponent with ϕ gives a clear indication of the influence of particle interactions on the chaotic response of the suspension. The existence of a low dimensional chaotic attractor underlying the fluctuations opens up the possibility of technological applications such as chaos control to temper the fluctuations.

For non-Brownian Stokesian suspensions, the instantaneous value of the stress is related to the instantaneous separation between particles, i.e. their configuration. The evolution of the n-particle configuration distribution function $f_n(\boldsymbol{r})$, is governed by the Smoluchowski equation [Brady and Morris, 1997] [18], which reduces to a balance between accumulation and advection in the absence of Brownian motion,

$$\frac{\partial f_n}{\partial t} + \sum_{\alpha=1}^{n} \nabla_\alpha \cdot (\boldsymbol{U}_\alpha f_n) = 0. \tag{4.15}$$

If the velocities $\boldsymbol{U}_\alpha$ are independent of f_n, it is clear that (4.15) yields a fixed point for f_n. This was the basic assumption of [Batchelor and Green, 1972] [15]and [Brady and Morris, 1997] [18]. However, for bounded shear flows of the kind considered in this work that one usually encounters in practice, the velocities are determined by the local viscosity of the suspension, which in turn is a function of the configuration. There is hence a coupling between (4.15) and the equations of motion of the suspension. The non-linearity in the coupling in (4.15) allows the possibility of chaotic variation of the microstructure and therefore the stress, as is evident from our results.

For large samples and over long time scales, one intuitively expects that the evolution of the stress will be captured by a hydrodynamic description, an expectation that is in agreement with our observation of low dimensionality of the attractor. However, we must emphasize that this conclusion is not *a priori* obvious or evident: a suspension of macroscopic non-Brownian particles differs in a significant way from molecular fluid in that there is no inherent time-scale (set by the temperature) in the system. The imposed shear rate, which is the time-scale of macroscopic motion, is the only time-scale in the problem and, therefore, there is no separation of time scales normally observed in molecular systems. In other words, the frequency of fluctuations in the stress scale as the imposed shear rate. Thus, low dimensionality is an interesting observation we make, rather than a foregone conclusion: even at the pair-interaction level, the position distribution function f_2 is a *field* which in the dynamical sense is an infinite dimensional quantity. Our observation of low dimensionality of the stress fluctuations implies that only a few (between 4 and 8) moments of the position distribution function contribute to the stress fluctuations over a range of area fractions $0.05 \leq \phi \leq 0.6$. This appears to be an important and far-reaching result, as the task of connecting the microstructure to rheology is then much easier if we knew which of the moments of the former were the important ones and how we can compute them.

A clear physical picture of the stress fluctuations can be had if we recognize that large fluctuations in the stress arise from the formation and breakage of clusters of many particles that sometimes span the distance between the bounding walls. In simple shear, for instance, clusters form in the compression quadrant where hydrodynamic forces squeeze particles together. The clusters are then rotated by the vorticity of the flow, and the particles in the cluster are pulled apart in the extension quadrant. The rate of formation and breakage of the clusters, which determines the frequency of the stress fluctuations, is determined by the local number density and mobility of clusters, and one therefore gets a range of frequencies, as shown in figures (4.9) to (4.16). We also note both the shear stress and the normal stress fluctuations have similar correlation dimensions and maximum Lyapunov exponent. Since both the shear stress and the normal stress are determined by an appropriate function of the microstructure, our results seem to indicate that the dynamics of the microstructure is governed by a low-dimensional attractor having approximately the same correlation dimension and maximum Lyapunov exponent.

Comparing our simulations to a typical globally coupled map lattice, we note that the relative particle positions in our simulations correspond to the values attained by individual chaotic oscillators in a coupled map lattice, and the coupling between any two particles is a chaotic function of the difference in positions between any two particles. In a coupled map lattice sense this would correspond to a globally coupled map lattice where the coupling is calculated by summing up a chaotic function of the difference in values at any instant between the oscillators (particles) taken pairwise. Our system thus represents a generalization of a typical globally and democratically coupled map lattice. This result may thus have significant implications for the theory of coupled map lattices.

CHAPTER 5

Modeling System Dynamics

5.1 Introduction

The concept of model implies a degree of simplicity, stripping away of all that is thought to be unnecessary in dynamical system modeling. By modeling, we can escape mathematical difficulty and can prove deeper results for the model equations than one could hope to achieve for the true equations, if they were known. By reformulating the underlying equations, we create a model whose laws of interaction no longer precisely matches those of the true equations. Our objective is to have model equations whose solutions possess general behavior qualitatively similar to the behavior of the original equations. The mathematical reasoning for dealing with qualitative results goes back to the time of Poincaré. The classical equations of motion are well known for a variety of problems. In fluid mechanics, the governing equations of motion, the Navier-Stokes equations, are an excellent description of the motion of weakly compressible fluids. Fluid flows are quite complicated and our intution is shaped by the knowledge of solutions of the Navier-Stokes equation. The problems encountered in seeking solutions of the Navier-Stokes equations reflect the profound difficulties in dealing with such a complicated equation of motion. For example, to determine accurate time-dependent solutions of the Navier-Stokes equations is a formidable numerical task. Most realistic models of physical or biological phenomena are complicated and there are mathematical methods to extract simplifications to highlight and elucidate certain aspects of the underlying process. Simpler representations extracted using mathematical analysis can be used to suggest new experiments and to corroborate the model equation.

Modeling natural phenomena has been a standard practice among scientists, especially among physicists. Traditionally, modeling a dynamical system requires one to derive the equations of motion from first principles, to measure initial conditions and, finally, to integrate the equations of motion forward in time. Alternately, when a first principles model is unavailable or initial conditions are not accessible or even though the equations describing the system are available, long range simulations are not feasible, empirical laws governing the physical processes can be obtained by model-fitting approaches based on the observed variability of the system evolution. Until recently, the most applied method to approximate dynamics from time series, assumed that the time series is produced by a linear system excited by white Gaussian noise. The variability of the time series is assigned to the stochastic nature of the excitation, which can not be modeled. The underlying idea of this approach assumes complex phenomena to result from complicated physics among many degrees of freedom. Nowadays, it is known that not all random-looking behavior is the product of complicated physics, but it may result from the chaotic nature of nonlinear and deterministic dynamics involving few degrees of freedom. In such cases, it is possible to exploit this determinism to make short-term forecasts that are more accurate than those obtained employing a linear stochastic model [Casdagli *et al.*, 1992] [27]. These forecasts are carried out by deterministic models directly built from observations of the system evolution.

Under the basic assumption that the system evolution is the output of a deterministic, nonlinear autonomous dynamical system, [Takens, 1981] [132], [Casdagli, 1989] [26], [Abarbanel *et al.*, 1993] [3], [Abarbanel, 1996] [2] [Kantz and Schreiber, 1997] [69] have put a strong foundation for buliding a dynamical model from a chaotic time series. Taken's embedding theorem [Taken, 1981] [132] guarantees that the system's state information can be recorvered from a sufficiently long observation of the output time series. According to this theorem, there exists a smooth mapping $\Psi{:}R^m \to R$ having the property

$$y(t) = \Psi[y(t-\tau),\, y(t-2\tau),\, \ldots,\, y(t-m\tau)] \tag{5.1}$$

Thus, building a dynamical model from a time series is a two-step process. First, using the immediate past behavior of the time series, we reconstruct the current state of the system (state space reconstruction). This is accomplished with a time delay embeddiing equation, where the dimension d_e of the attractor is estimated by the correlation dimension algorithm (and/or false-nearest-neighbor method, principal component analysis, etc.). In the previous chapter, we analysed the stress fluctuations of Stokesian suspension under simple shear flow and we obtained an insight into the dynamics of the system behavior. For each of the different area fractions ϕ = 0.05, 0.10, 0.20, 0.30, 0.40, 0.50 and 0.60, we estimated the number of independent variables (or independent coordinates or eigen vectors) required to reconstruct the chaotic attractor governing the system dynamics. We, also, computed the optimal time delay required for both the estimation of embedding dimension and reconstruction of the attractor in its actual phase space. Along with this, we computed the dynamic exponent viz. the Lyapunov exponent which is a measure of the rate at which two arbitrarily close trajectories in the chaotic region diverges from each other exponentially. The Lyapunov exponent plays a major role in model building, for a slight difference in any one of the building components (coefficients) will produce errors during iteration process and this error will be amplified within a short period of time due to the chaotic nature of the system. This amplification of error adversely affects the efficiency, reliability and robustness of the model equation. So, model building, especially, from a chaotic time series is a very difficult process which has to be performed with great caution. Agreement at both the quantitative and qualitative levels of the model equation properties with that of the original system properties is a rare event in the case of model building from chaotic time series. In most situations, we get model equations of the time series giving results which qualitatively agree with that of the original system. With this understanding we shall proceed to the second part of the model building procedure.

In the second part, we construct the predictive model Ψ using some standard methods. In the following sections, we describe a systematic procedure to accomplish this part with the insight gained from the analysis of the original time series described in the previous chapter. We note that, the estimation of embedding dimension (correlation dimension or number of principal components) gives us an estimate of the upper bound to the number of independent variables required in the phenomenological model for the stress components at each of the different concentrations of the particles in the suspension. So model building is both instructive and informative in the sense that if we are able to construct a reliable and efficient model with as many number of independent variables as the estimated embedding dimension for the stress components at the respective concentrations of the particles in suspension, then the model equation will indirectly provide more justification of our analysis. In the formal sense, an efficient and reliable model equation opens up more directions (possibilities) to further our analysis of the original system such as controlling the temporal fluctuations of the stress components through the proper handling of the parameters in the model equation, synchronizing one stress component with another stress component, expanding the parameter space to search for new phenomena or already existing phenomena of similar (or related) systems, etc.

5.2 Evolutionary algorithm

Various techniques can be used to the task of approximating the predictive model Ψ [Correa *et al.*, 2000] [31], [Judd, 2003] [68]. The prominent methods in this direction are based on polynomial fitting, neural networks, radial basis functions [27]. Another important method is the global vector field reconstruction for the reconstruction of a set of differential equation that models both theoretical and experimental data. The papers [Gouesbet, 1991] [52], [Gouesbet, 1991] [53], [Letellier *et al.*, 1995] [79], [Letellier *et al.*,1997] [80],[Letellier *et al.*, 1998] [81] describe global vector field reconstructoin technique for both theoretical and experimental data. Of these different methods of model selection for nonlinear time series, most methods need large numbers of parameters and they tend to overfit [Namamura *et al.*, 2003] [92]. A host of papers deal with the comparison of different methods of model selection for time series [Nakamura *et al.*, 2004] [93] and some paper propose a heuristic method of approach [Nakamura *et al.*, 2004]. Recently, a functional search procedure based on Darwinian theories of natural selection and survival has been described [Koza, 1992] [76]. The main advantage of the so-called evolutionary algorithms[Eiben *et al.*, 2003] [39], is that sparse data are sufficient and as a by-product, these algorithms attempt to approximate the functional form underlying the data [Szpiro, 1997] [131], providing more direct knowledge of functional relations between past, present and future values of the time series. Based on the algorithm developed by [Szpiro, 1997] [131], an evolutionary algorithm called DARWIN, programmed by [Alvarez *et al.*, 2001] [7], provides capabilities of modeling chaotic time series.

The evolutionary algorithm DARWIN is programmed to approximate the equation, in symbolic form, that describes the time series. The searching procedure followed by this algorithm is more sophisticated than enumerating all possible equations. The evolutionary algorithm considers an initial population of potential solutions which are subjected to an evolutionary process, by selecting from the initial population those equations (individuals) that best fit the data. The strongest strings choose a mate for reproduction whereas the weaker strings become extinct. The newly generated population is subjected to mutations that change fractions of information. The evolutionary steps are repeated with the new generation. The process ends after a number of generations *a priori* determined by the user. The symbolic form of the equation strings is encoded into a numerical structure to facilitate processing of the symbolic strings. The important stages in the evolutionary algorithm are the following. For a more comprehensive and exhaustive treatment of the algorithm the reader is referred to [Szpiro, 1997] [131], [Alvarez *et al.*, 2001] [7].

5.2.1 Generating the initial population

The first stage in the evolutionary process is the generation of an initial population of individuals as a basis for future generations. If initial estimates of potential solutions of the problem are not available, the usual procedure is to consider a randomly generated population of equations derived from random combinations of arguments and operators. This is accomplished by randomly determining the nature, argument or operator of each element in the string followed by the requirement that the final individuals must be consistent mathematical expressions.

5.2.2 Computing the strength of the individuals

The criterion of the strength of each individual (equation string) in the population is its fitness measure. Each individual $\Psi_j(\cdots)$ is used to compute estimates of all $y(t)$ in part of the time series, called the training set, as a function of the previous values of the time series. For μ-step ahead predicton problem, the fitness for a candidate model $\Psi_j(\cdots)$ is then computed as

$$\Delta_j^2 = \sum_{t=L+1}^{T} [y(t)-\Psi_j(y(t-\mu\tau), y(t-(\mu+1)\tau), y(t-(\mu+2)\tau), \ldots, y(t-(\mu+m-1)\tau)]^2 \quad (5.2)$$

for a scalar time series, where $L = m\tau$, m being the embedding dimension, τ being the optimal time delay, and T is the total length of the training data set. The numerical evaluation of each expression Ψ_j is carried out using *stacks* where the arguments of the expression are stacked until required by an operator [Bamford and Curran, 1991] [12]. A strength index for each individual can be expressed in the form

$$R_j = 1 - \frac{\Delta_j^2}{\sum_{t=L+1}^{T}[y(t) - \bar{y}]^2} \tag{5.3}$$

where $\bar{y}$ represents the mean value of the training data. The factor R_j, called explained variance, can be interpreted as the percentage of the training set's total variance explained by the j-equation string. The closer to the unit value R_j, the stronger will be the j-individual. A validation or out-of-sample testing set is constituted by the data not included in the training set, ie., $\{y(t)\}_{t=T+1}^{N}$, where N is the total number of data points in time series. The validation set is not employed by the algorithm during the selection process. A strength of the final best individual allows differentiation between cases in which a good estimation of the dynamics is obtained from over-fitting situations. In the first case, the strength indexes in the training and validation sets are near one. Over-fitting occurs when the final individual is weak in the validation set.

5.2.3 Reproduction and mutation

Once the mates are selected according to their strength, a crossover of self-contained parts between the two parent strings is carried out to generate two new offspring. The procedure starts determining randomly one of the arguments, real number or element of the time series, in the first string. If the next element to the right of this randomly selected argument is an operator, only this argument is considered for interchanging. If the next pair to the randomly selected argument represents another argument, the part of the string used for the crossover is that which is limited between the randomly selected argument and that element of the string where the numbers of arguments, n_{ar}, and the number of operators,n_{op} between the randomly selected argument and the element (including both) verify the relation $n_{\mathrm{ar}} = n_{\mathrm{op}} + 1$. If any of the above criteria are not realized, another argument in the string is randomly selected. The object of this procedure is to interchange self-consistent parts between the equation strings in order to avoid inconsistent mathematical expressions in the offspring. The same operation is carried out for the second equation string. The offspring strings can be longer than the parents but always bounded by a maximum length n_{tot}. If a determined interchange of self-contained parts between the parent strings generate an offspring longer than n_{tot}, then this specific interchange is not allowed and another self-contained part in one of the parent strings is randomly selected for interchanging. This is repeated till the condition is valid. Two replicas of the parent strings are also considered as offspring in the reproduction process. A mutation is applied to the individuals of the population, except to the top ranked equation strings in order to avoid inadvertently losing their information. Each element of a determined string has some probability to be changed by a mutation process. A more detailed and technical exposition of this evolutionary algorithm is given in [Alvarez*et al.*, 2001] [7].

We make good use of this evolutionary algorithm for modeling our system using the information gained from analysis of the attractor. The knowledge of the dynamic characteristic Lyapunov exponent also gives insight about the model and the consequent prediciton. We build models for data with area of fractions varying from 5% to 40%.

5.3 Model equations of the stress components

Using the evolutionary algorithm, we modeled the shear stress σ_{xy} component with area fraction of particle $\phi = 0.05$ and with embedding dimension $m_e = 6$ and time delay τ = 2. We used 38000 data points of which 7000 data points were used for training and the remaining data points were used for validation of the model equation. Our analysis described in the previous chapter revealed that at most four dimensions are sufficient for complete characterization of the stress fluctuations at area fraction $\phi = 0.05$. We put a higher embedding dimension to see if it needs more dimensions than revealed by our analysis. The evolutionary algorithm produced a model equation of the following form

```
x_0(t) = (x_0(t-6)+((((-2.23)-((x_0(t-6)-(((9.50)*((x_0(t-10)/
 (0.89))-(x_0(t-4)+ x_0(t-6))))-(x_0(t-6)+x_0(t-6))))*
 (-1.55)))-((0.54)+x_0(t-10)))*(x_0(t-4)-x_0(t-2))))
```

Taking x = x_0(t-2), y = x_0(t-4), z = x_0(t-6), u = x_0(t-10) and w=x_0(t), we simplified this to the form

$$w = (x - y)(2.23 - 14.725y - 16.275z + 16.55u) \tag{5.4}$$

The equation is able to make global prediction of the future values with more than 99% accuracy. We observe that the equation contains only four independent variables which is in good agreement with our analysis using the tools of nonlinear dynamics and chaos theory. Here, we took different sections of a single time series length 50000 and modeled each of the different sections. We found that the model equations are statistically equivalent to the above equation. Next we took the normal stress σ_{yy} component with area fractions $\phi = 0.1$. Using the evolutionary algorithm we modeled the normal stress σ_{yy} component with embedding dimension $m_e = 7$ and time delay $\tau = 2$. Our analysis using the tools of nonlinear dynamics and chaos theory revealed that four independent variables are sufficient to describe the behavior of the system dynamics. For this data we got the following model equation in the form

```
x_0(t) =(x_0(t-2)+((x_0(t-4)-(x_0(t-2)-x_0(t-4)))/
(((-2.42)-(x_0(t-4)-(((9.43)+(-4.41))*
```

```
((x_0(t-10)-(x_0(t-6)-x_0(t-2)))+(x_0(t-2)*
((-6.19)-x_0(t-2)))))))-x_0(t-6)))
```

Taking x = x_0(t-2), y = x_0(t-4), z = x_0(t-6), u = x_0(t-10) and w = x_0(t), we simplified the above equation to the form

$$w = x + \frac{2y - x}{ax - abx - ax^2 - y - z - az + au - 2.42} \tag{5.5}$$

where $a = 5.02$, $b = -6.19$. This model equation is able to give a global prediction of stress component values with more than 95% accuracy. Note that the number of independent variables is four which is what we anticipated from the analysis described in the previous chapter. Here, also, we performed model construction for different sections of time series of normal stress component and found that the model equations for each of the parts are equivalent to the above equation. Next, we took normal stress fluctuations with area fraction of particles $\phi = 0.2$. Our analysis on this data revealed that for a complete description of the attractor five independent variables required. We modeled this normal stress component and got the following equation as the model equation for the data.

```
x_0(t)= (x_0(t-2)-(x_0(t-4)+(((x_0(t-6)/((-4.21)+((-6.84)+
((x_0(t-12)-(x_0(t-4)*((4.58)+(x_0(t-14)/x_0(t-6)))))*
((-3.61)*(9.24))))))*(2.15))-(x_0(t-2)/(2.17)))))
```

Taking x = x_0(t-2), y = x_0(t-4), z = x_0(t-6), u = x_0(t-12), v = x_(t-14) and w = x_0(t), we simplified the above equation to the form

$$w = \frac{3.15}{2.15}x - y - \frac{2.15z^2}{auz - abyz - avy - 11.05z} \tag{5.6}$$

where $a = 33.3564$, $b = 4.58$.

This equation is able to make global prediction of the future values of the stress fluctuations with an accuracy of more than 92% accuracy. The number of independent variables is in good agreement with our analysis of this time series using methods of nonlinear dynamics methods and chaos theory. Also, we, constructed model equation for the stress component with area fractions $\phi = 0.3$ with embedding dimension $m_e = 8$ and time delay $\tau = 2$ using evolutionary algorithm. Our analysis revealed that five or six independent variables are required to reconstruct the system dynamics of the stress fluctuations at area fractions $\phi = 0.3$. We got the following model equation,

```
x_0(t)=(x_0(t-2)+((((-5.22)*x_0(t-4))+((x_0(t-2)-(x_0(t-8)*
(x_0(t-4)*(x_0(t-4)*((8.55)/((x_0(t-14)-(x_0(t-2)*
x_0(t-6)))-(x_0(t-8)*(9.61))))))))*(2.08)))/(7.17)))
```

for normal stress component with area fraction of particles $\phi = 0.3$. We simplified the above equation to the following form by taking x = x_0(t-2), y = x_0(t-4), z = x_0(t-6), u = x_0(t-8), v = x_(t-14) and w=x_0(t)

$$w = x + \frac{a}{e}y + \frac{d}{e}\left(x - \frac{buy^2}{v - xz - cu}\right) \tag{5.7}$$

where a = -5.22, b = 8.55, c = 9.61, d = 2.08 and e = 7.17. This equation is able to give global prediction of the future values of the stress component with more than 85% accuracy. We modeled the stress component of the suspension with area fraction of particles $\phi = 0.4$ and we got equations having number of independent variables five. We oberved that accuracy of the model equations decreases drastically with rise in concentration of particles in the suspension.

In all the above model construction, we used the time delay $\tau = 2$. We made this choice of time delay after going through a lot of experimentation with different time delays. The methods autocorrelation function, average mutual information and space time separation plot, give guide lines to choose the proper time delay by suggesting a range of possible time delays. We experimented with different time delays suggested by these methods and

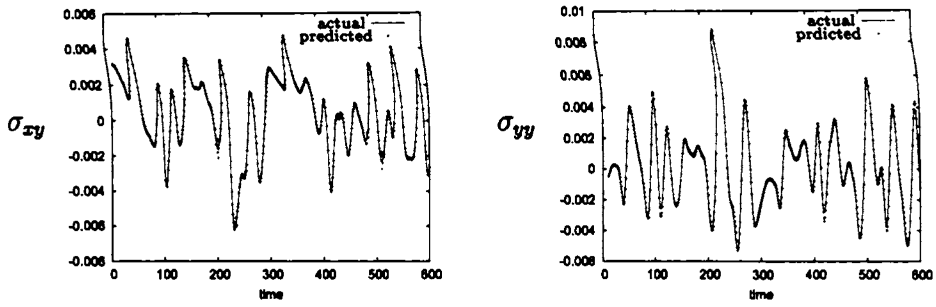

(a) (b)

Figure 5.1: Global prediction of (a) shear stress σ_{xy} and (b) normal stress at ϕ=0.05.

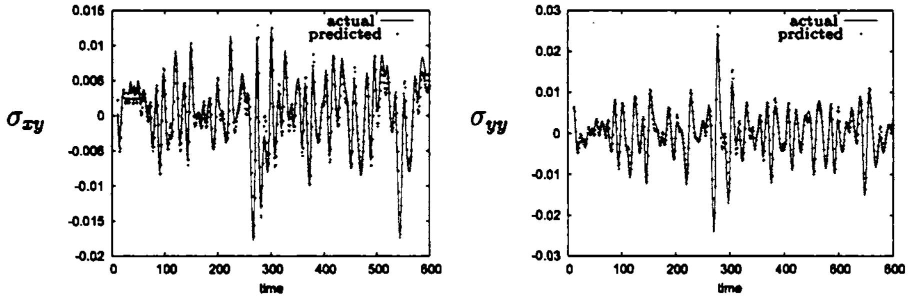

(a) (b)

Figure 5.2: Global prediction of (a) shear stress σ_{xy} and (b) normal stress at ϕ=0.10.

chose that value of time delay to construct reliable model equations whose qualitative and quantitative properties are in good agreement with those of the original system. We found that the properties of model equations are closer to the properties of the original time series for time delays close to 2, 3, 4 and 5. For these time delays the properties of time series generated from the model equations agree well with the properties of the actual time series both qualitatively and quantitatively (see sec.5.4).

5.4 Comparison of model properties with that of the data

We would like to see to what extent our model equations are able to reproduce the qualitive and quantitative properties of the original attractor. We constructed model

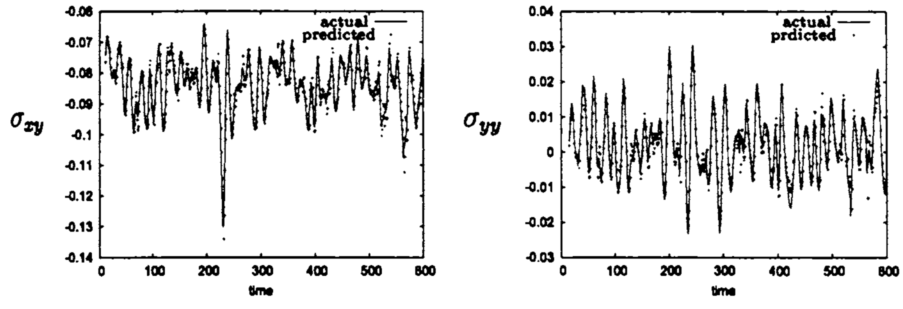

(a) (b)

Figure 5.3: Global prediction of (a) shear stress σ_{xy} and (b) normal stress at ϕ=0.20.

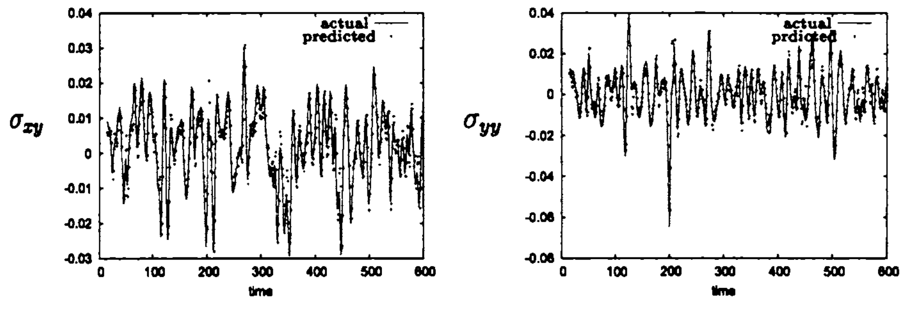

(a) (b)

Figure 5.4: Global prediction of (a) shear stress σ_{xy} and (b) normal stress at ϕ=0.30.

equations for both the shear and normal stresses for area fractions of particles ϕ in the range $0.05 \leq \phi \leq 0.4$ In the following, we shall compare the properties captured by the model equations with the corresponding properties of the respective time series. Figures (5.1) to (5.5) illustrate the predicted time series using model equations with the corresponding time series of the actual stress components at their respective area fraction.

In figure (5.1), figure (a) compares the predicted shear stress at the area fraction $\phi =$ 0.05 with the original shear stress at that area fraction of particles and figure (b) compares the predicted normal stress at the same area fraction of particles with the original normal stress at that area fraction of particles. We observe good agreement in both the stress components. Similarly, each of the figures (5.2) to (5.5) compares the predicted shear and normal stresses with the corresponding shear and normal stresses at area fractions

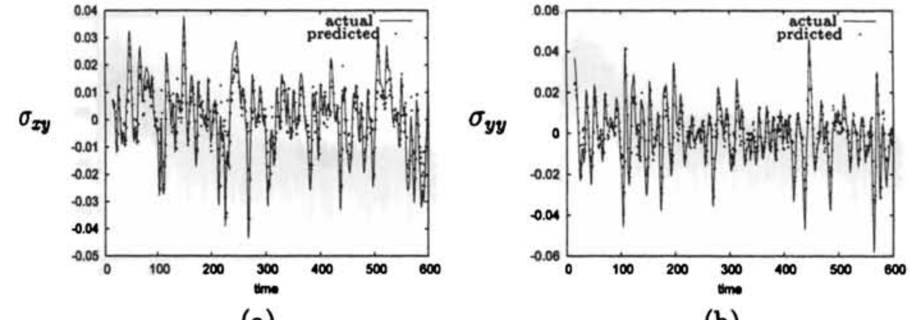

(a) (b)

Figure 5.5: Global prediction of (a) shear stress σ_{xy} and (b) normal stress at ϕ=0.40.

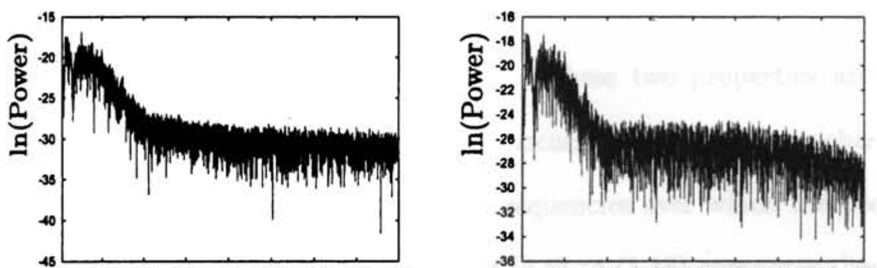

(a) (b)

Figure 5.6: Logarithm of power spectrum versus frequency for shear stress σ_{xy} at ϕ=0.05, (a) actual and (b) predicted

ϕ = 0.10, 0.20, 0.30 and 0.40 respectively. We observe good agreement of the predicted stress components with corresponding actual stress components. We, also, remark that the model building becomes more time consuming as the concentration of the particles increases and we observe that the accuracy of the predicted stress components decreases with increase in concentration and this is expected as there is monotonic increase in the Lyapunov exponent with increasing concentration as a consequence of frequent many-body interactions in the suspension.

We, next, performed a frequency decomposition of the predicted stress components for the above range of area fraction of particles. We observe a broad band power spectrum for each of the stress components for area fractions ϕ in the range $0.05 \leq \phi \leq 0.40$.

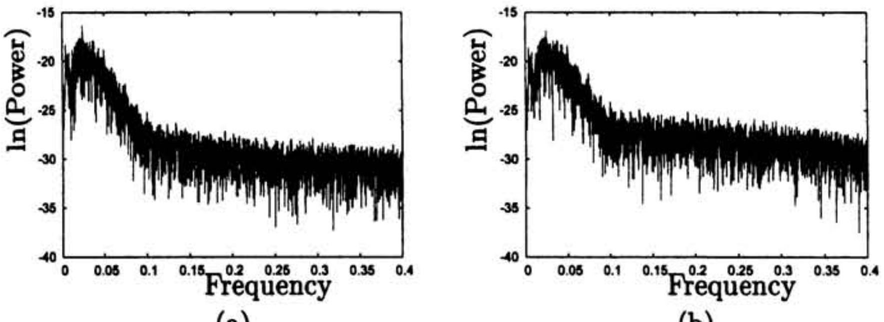

(a) (b)

Figure 5.7: Logarithm of power spectrum versus frequency for normal stress σ_{yy} at ϕ=0.05, (a) actual and (b) predicted

The power spectrum shows exponential decay. These two properties are common to both deterministic chaotic signals and linear autocorrelated noise (or stochastic process). We, also, observe an increase in the range of frequencies over which the decay of power occurs with rise in concentration. The figures (5.6) to (5.15) compares these properties of the predicted stress components with those of the original stress components for the area fractions ϕ over the range $0.05 \leq \phi \leq 0.40$. In figure (5.6), we compare the power spectrum of shear stress predicted using the model equation with the power spectrum of the original shear stress with area fraction $\phi = 0.05$. We observe a good degree of agreement both qualitatively and quantitatively. It is interesting to note that power spectrum plots of the predicted shear stress and actual shear stress are almost identical. In figure (5.7) the power spectrum of the predicted normal stress at area fractions $\phi = 0.05$ is compared with that of the original normal stress at that area fraction of particles. Here, also, we see that both the figures are almost identical having broad band power spectrum and exponential decay. The range of frequency over which the exponential decay occurs is same. That is, the properties of the original shear and normal stress components are carried over to the predicted shear and normal stress components as far as the power spectrum properties are concerned. This shows that predicted and actual stress components agree both in qualitative and quantitative properties upto the power

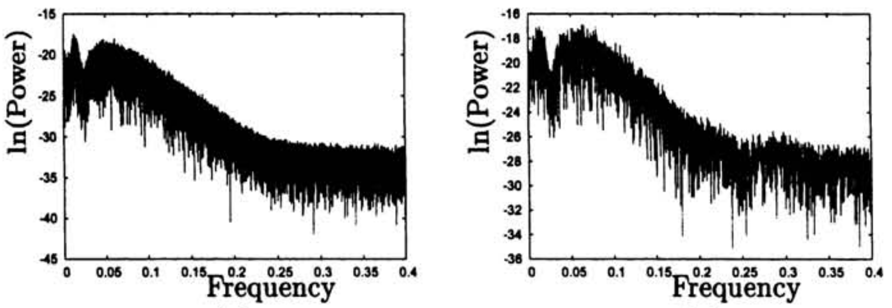

(a) (b)

Figure 5.8: Logarithm of power spectrum versus frequency for shear stress σ_{xy} at ϕ=0.10, (a) actual and (b) predicted

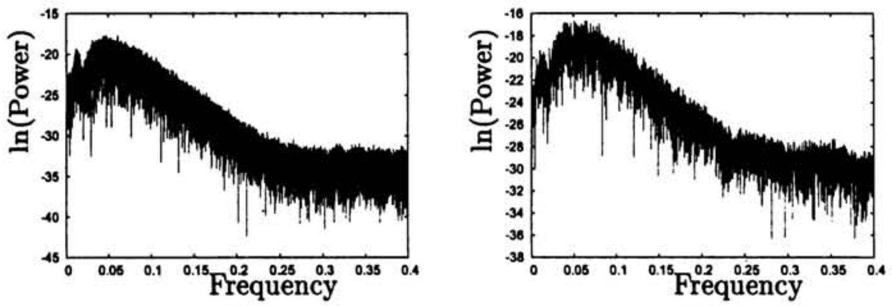

(a) (b)

Figure 5.9: Logarithm of power spectrum versus frequency for normal stress σ_{yy} at ϕ=0.10, (a) actual and (b) predicted

spectrum properties for the area fraction particle $\phi = 0.05$. Figures (5.8) to (5.15) make a comparison of shear and normal stresses alternately for area fractions of particles over the range $0.10 \leq \phi \leq 0.40$. For each of the stress components viz. shear and normal stresses, the power spectrum plots shows broad band nature and exponential decay of powers for time series generated by the respective model equations and these properties of model generated stress components agree with those properties of the actual stress components at the respective area fraction of particles.

We, next, computed the autocorrelation function for both stress components viz. shear and normal stress components of the model generated stress components over the above range of area fraction of particles. We observe good qualitative agreement of

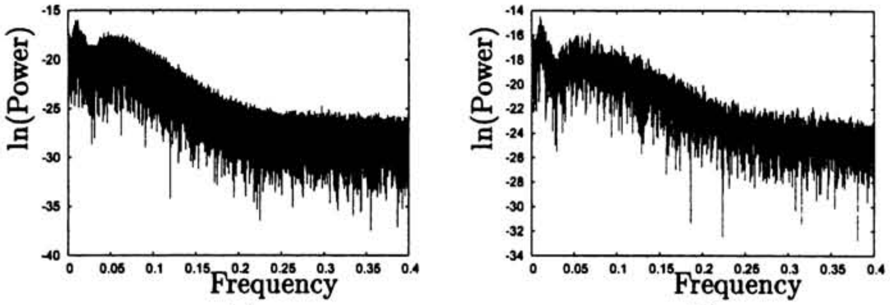

(a) (b)

Figure 5.10: Logarithm of power spectrum versus frequency for shear stress σ_{xy} at ϕ=0.20, (a) actual and (b) predicted

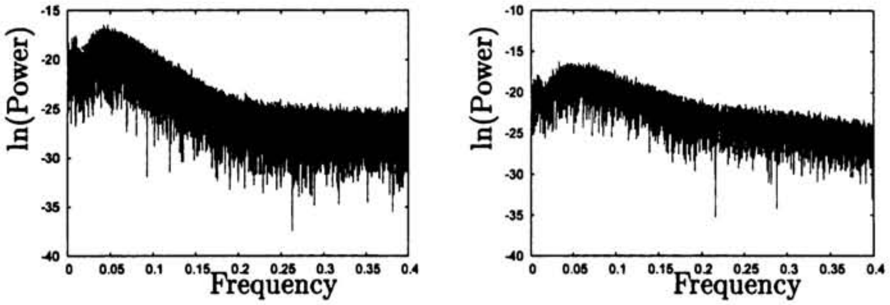

(a) (b)

Figure 5.11: Logarithm of power spectrum versus frequency for shear stress σ_{xy} at ϕ=0.20, (a) actual and (b) predicted

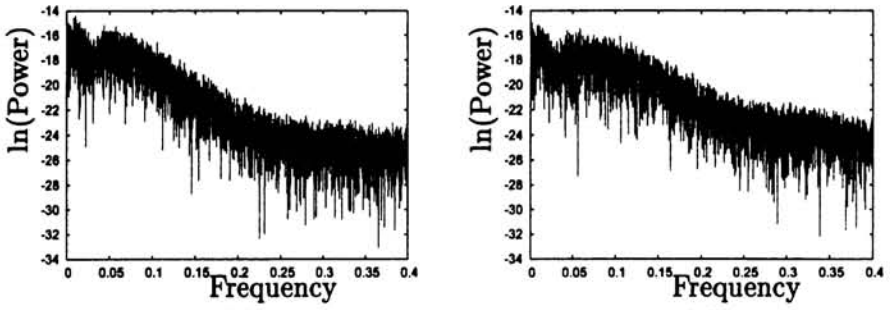

(a) (b)

Figure 5.12: Logarithm of power spectrum versus frequency for shear stress σ_{xy} at ϕ=0.30, (a) actual and (b) predicted

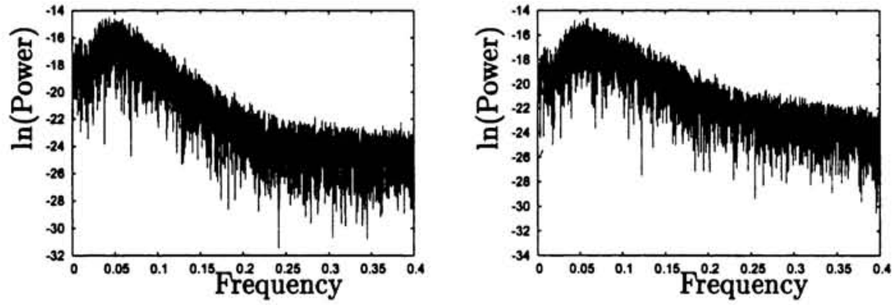

(a) (b)

Figure 5.13: Logarithm of power spectrum versus frequency for normal stress σ_{yy} at ϕ=0.30, (a) actual and (b) predicted

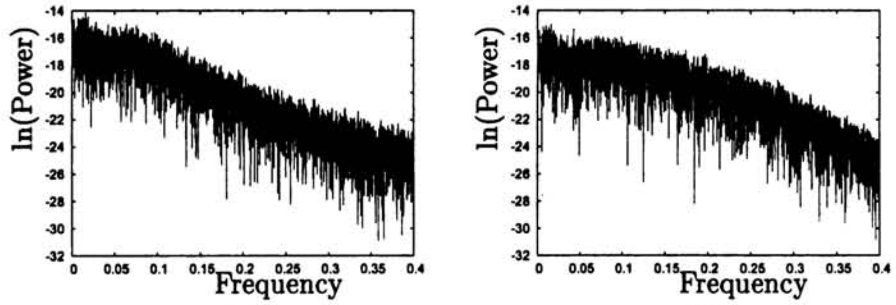

(a) (b)

Figure 5.14: Logarithm of power spectrum versus frequency for shear stress σ_{xy} at ϕ=0.40, (a) actual and (b) predicted

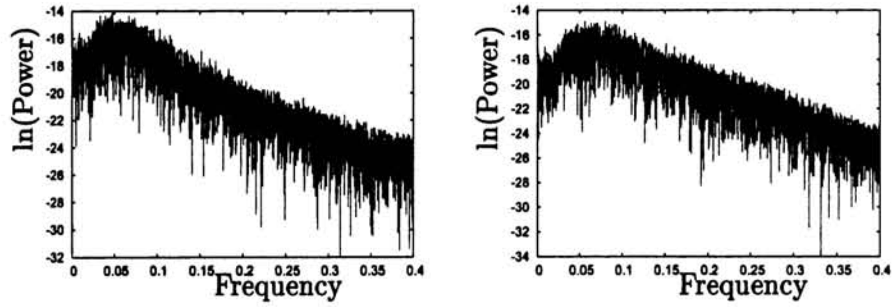

(a) (b)

Figure 5.15: Logarithm of power spectrum versus frequency for normal stress σ_{yy} at ϕ=0.40, (a) actual and (b) predicted

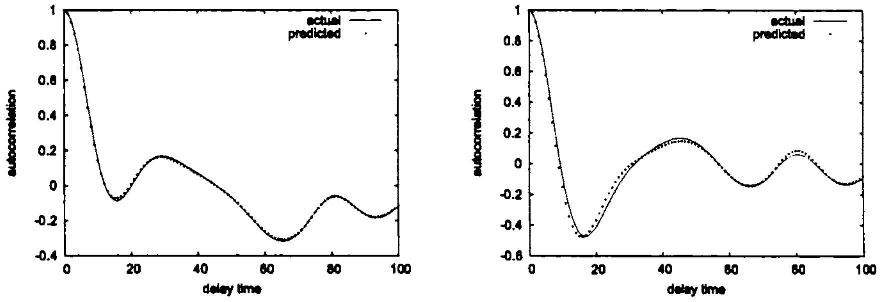

(a) (b)

Figure 5.16: Autocorrelation function for (a) shear stress σ_{xy} and (b) normal stress σ_{yy} at ϕ=0.05.

the autocorrelation function with that of the original stress components. We computed the time delays at which the autocorrelation functions of the model generated stress components attains local minimum. We observe that for fixed area fraction of particles, the autocorrelation function of both the stress components attains the local minimum at the same time delay. There is a high degree of agreement in the qualitative nature of the figures for both stress components at all the area fractions of particles. The figures (5.16) to (5.20) compare the autocorrelation functions of original stress components (continuous line in the figures) and autocorrelation function of the model generated stress components (dots in the figures). Good qualitative agreement is clearly visible. We computed the local minima of autocorrelation functions from these figures and the Table (5.1) compares the quantitative agreement of the local minima attained by the stress components for a range of area fractions of particles. Here, also, we get good agreement.

Next, we computed the average mutual information function for the stress components generated by the model equation for area fraction of particles over the range $0.05 \leq \phi \leq 0.40$. The figures (5.21) to (5.25) compares the average mutual function of the model generated stress (dots in the figures) components with that of the simulated stress components (continuous line in the figures) using Stokesian Dynamics. we get excellent qualitative equivalence of the average mutual information function for the

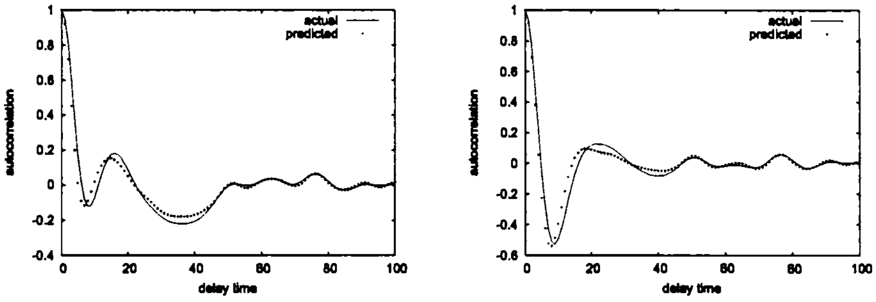

(a) (b)

Figure 5.17: Autocorrelation function for (a) shear stress σ_{xy} and (b) normal stress σ_{yy} at ϕ=0.10.

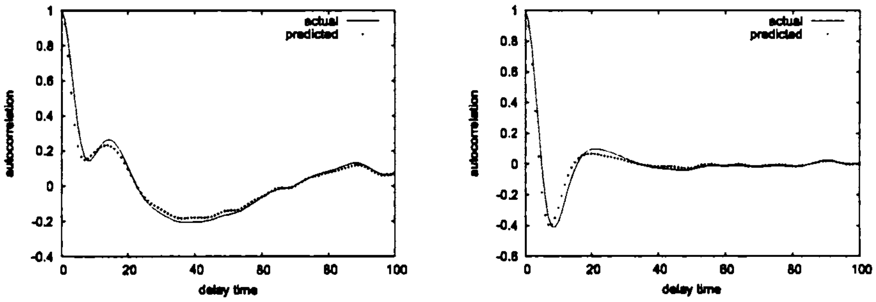

(a) (b)

Figure 5.18: Autocorrelation function for (a) shear stress σ_{xy} and (b) normal stress σ_{yy} at ϕ=0.20.

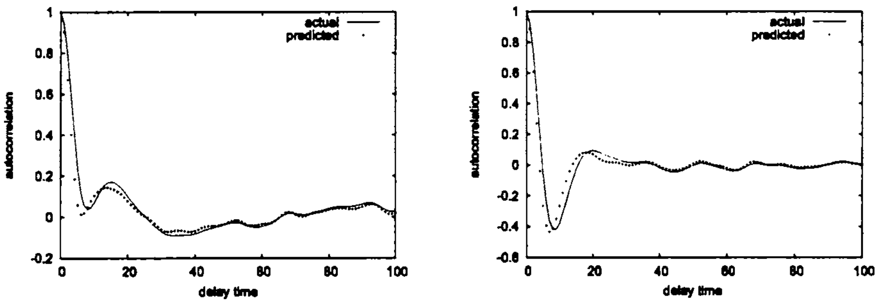

(a) (b)

Figure 5.19: Autocorrelation function for (a) shear stress σ_{xy} and (b) normal stress σ_{yy} at ϕ=0.30.

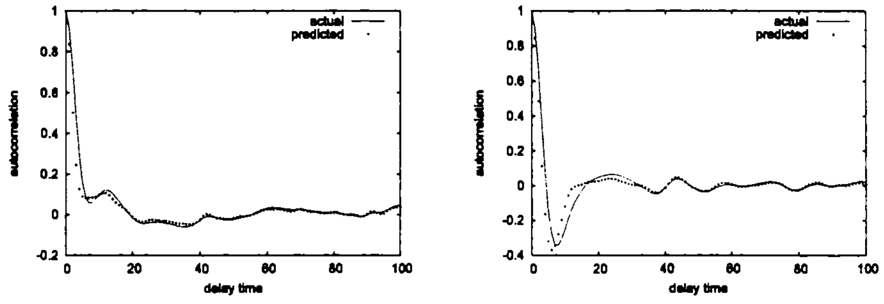

(a) (b)

Figure 5.20: Autocorrelation function for (a) shear stress σ_{xy} and (b) normal stress σ_{yy} at ϕ=0.40.

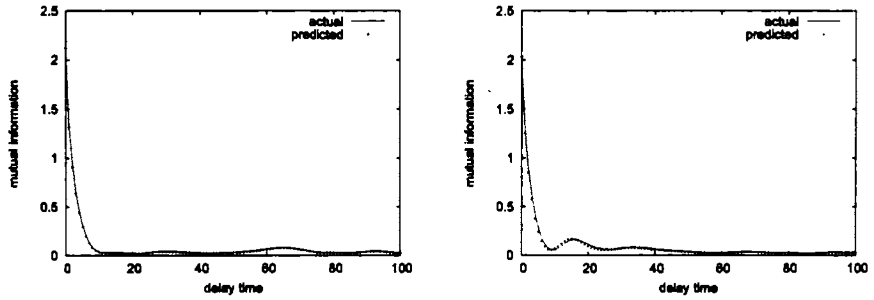

(a) (b)

Figure 5.21: Average mutual information for (a) shear stress σ_{xy} and (b) normal stress σ_{yy} at ϕ=0.05.

model generated stress components and that of the original stress components simulated using Stokesian Dynamics over the above range of particle concentration. The Table (5.2) compares the delay times at which average mutual information function of the actual stress components σ_{xy} and σ_{yy} (continuous line) simulated using Stokesian Dynamics method attains local minima with that of the model generated stress components (dots) as observed from figures (5.21) to (5.25). To a great extent, we obtain good quantitative equivalence of the properties of simulated stress components and model generated stress components. We, also, observe that the accuracy deteriorates with increasing concentration.

We next perform the comparison of space-time separation plots of the model generated

ϕ	0.05	0.10	0.20	0.30	0.40
σ_{xy} or σ_{yy}	15	9	8	8	7

(a)

ϕ	0.05	0.10	0.20	0.30	0.40
σ_{xy} or σ_{yy}	15	8	7	6	6

(b)

Table 5.1: Comparison of the local minima attained by the autocorrelation function of (a) the actual stress components σ_{xy} and σ_{yy} simulated using Stokesian Dynamics with that of the (b) model generated stress components as observed from figures (5.16) to (5.20)

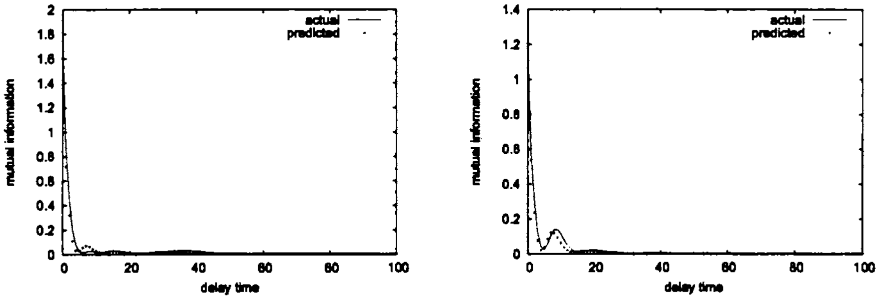

(a) (b)

Figure 5.22: Average mutual information for (a) shear stress σ_{xy} and (b) normal stress σ_{yy} at ϕ=0.10.

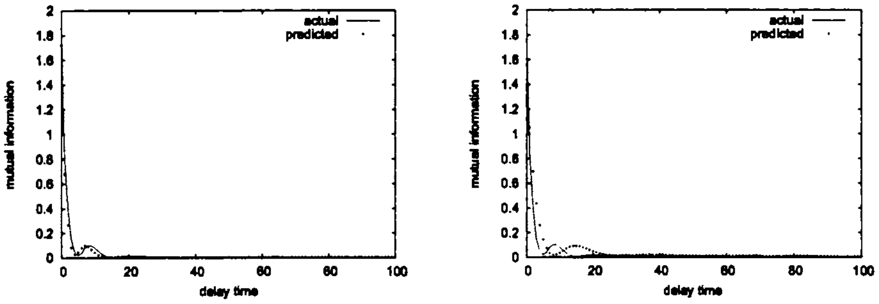

(a) (b)

Figure 5.23: Average mutual information for (a) shear stress σ_{xy} and (b) normal stress σ_{yy} at ϕ=0.20.

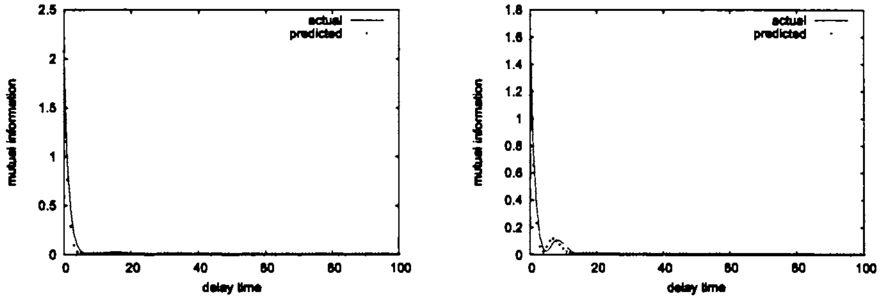

(a) (b)

Figure 5.24: Average mutual information for (a) shear stress σ_{xy} and (b) normal stress σ_{yy} at ϕ=0.30.

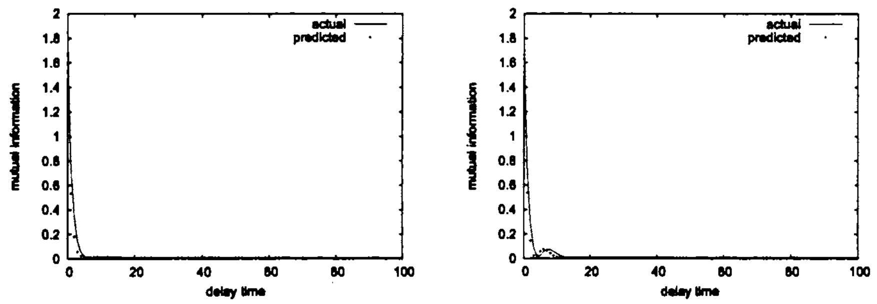

(a) (b)

Figure 5.25: Average mutual information for (a) shear stress σ_{xy} and (b) normal stress σ_{yy} at ϕ=0.40.

ϕ	0.05	0.10	0.20	0.30	0.40
σ_{xy}	10	6	7	6	6
σ_{yy}	9	5	6	5	5

(a)

ϕ	0.05	0.10	0.20	0.30	0.40
σ_{xy}	10	5	6	5	5
σ_{yy}	9	4	8	4	4

(b)

Table 5.2: Comparison of the local minima attained by the average mutual information function of (a) the actual stress components σ_{xy} and σ_{yy} simulated using Stokesian Dynamics with that of (b) the model generated stress components as observed from figures (5.21) to (5.25)

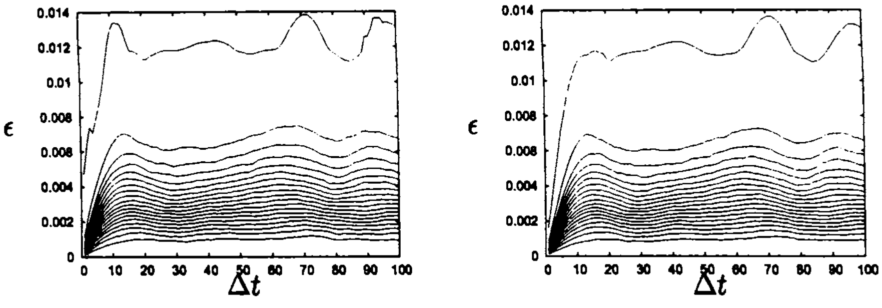

(a) (b)

Figure 5.26: Space-time separation plot of (a) actual and (b) predicted shear stress σ_{xy} at ϕ=0.05.

stress components with that of the simulated stress components, using the Stokesian Dynamics method for the different area fractions of particles over the range $0.05 \leq \phi \leq 0.4$. The figures (5.26) to (5.35) compares the space-time separation plots of the model generated stress components (figure (b) in all figures) with that of the simulated stress components (figure (a) in all figures) for the above range of area fraction of particles. We observe high degree of qualitative equivalence of the properties of space-time separation plots for both the stress components for all the particle concentration considered in this comparison. We estimated the approximate delay time above which the contour lines in the space-time separation plots for the model generated stress components attains saturation. Table (5.3) compares the delay time above the contour lines of space-time separation plots of model generated stress components with that of the simulated stress components. We can observe great deal of agreement between these delays for both shear and normal stress components.

In the preceding discussion, we compared the power spectrum, autocorrelation function, average mutual information function and space-time separation plots of the simulated stress components of Stokesian suspension with that of the model generated stress components for a range of particle concentrations. We observed a high degree of equivalence between both simulated data and model generated data in respect of the qualitative

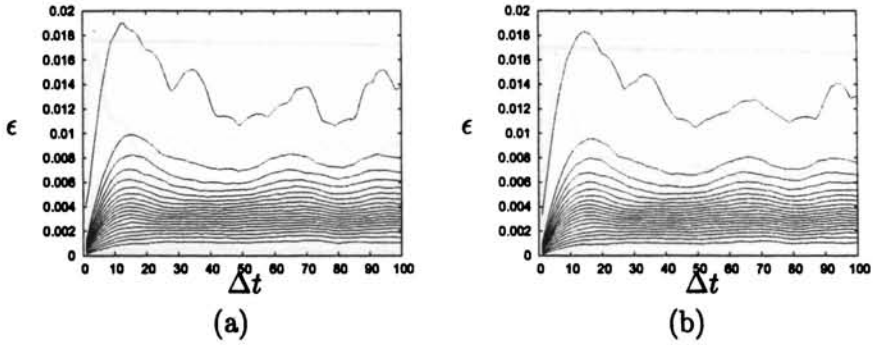

(a) (b)

Figure 5.27: Space-time separation plot of (a) actual and (b) predicted normal stress σ_{yy} at ϕ=0.05.

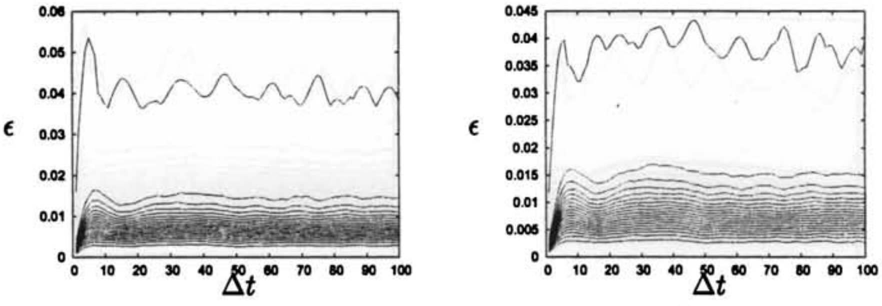

(a) (b)

Figure 5.28: Space-time separation plot of (a) actual and (b) predicted shear stress σ_{xy} at ϕ=0.10.

properties characterized by these methods. We, also, observe a great extent of agreement in quantitative properties.

Next, we check how far our model equations are able to capture the qualitative and quantitative topological (geometrical) and dynamical characteristics of the simulated stress components of Stokesian suspension. We have already estimated the probable optimal delay time using autocorrelation function, average mutual information and space-time separation plots. These values are in close agreement with those of the simulated stress component values. Here also, we take delay time $\tau = 2$ to compute the correlation

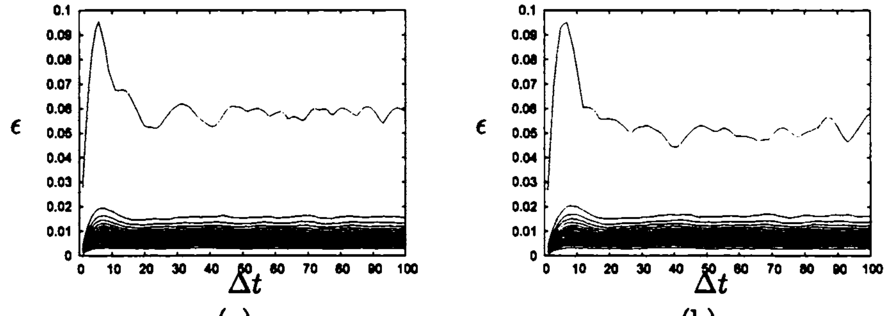

(a) (b)

Figure 5.29: Space-time separation plot of (a) actual and (b) predicted normal stress σ_{yy} at ϕ=0.10.

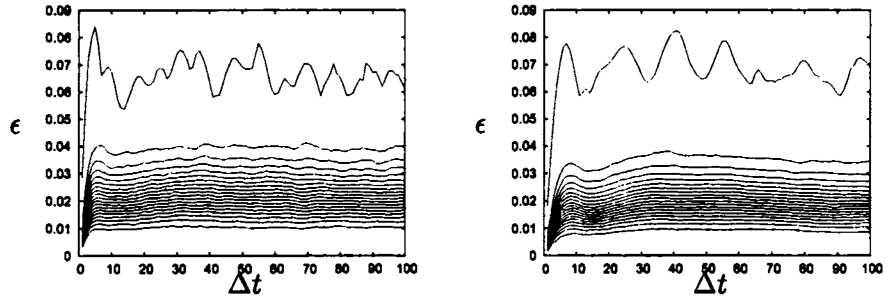

(a) (b)

Figure 5.30: Space-time separation plot of (a) actual and (b) predicted shear stress σ_{xy} at ϕ=0.20.

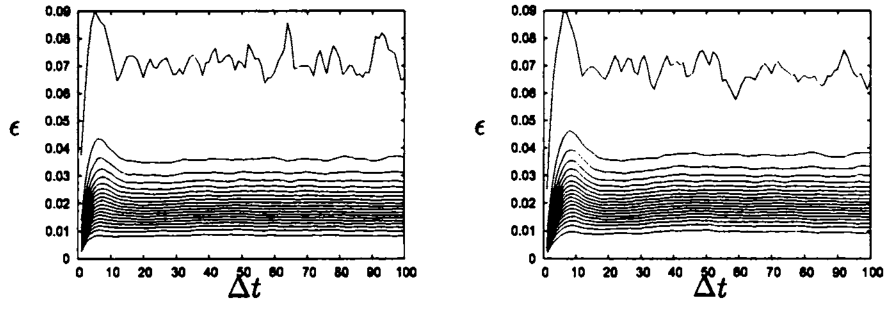

(a) (b)

Figure 5.31: Space-time separation plot of (a) actual and (b) predicted normal stress σ_{yy} at ϕ=0.20.

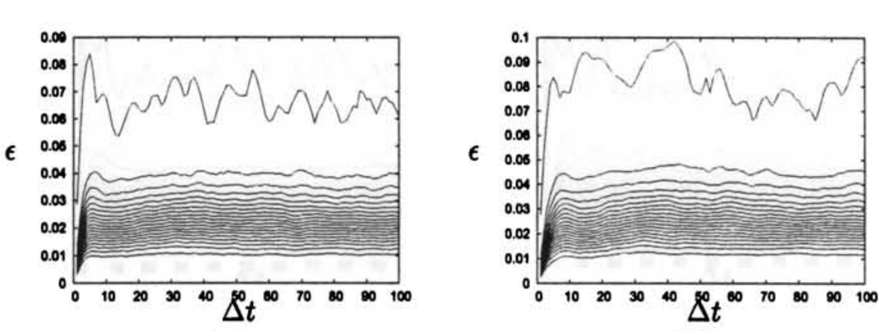

(a) (b)

Figure 5.32: Space-time separation plot of (a) actual and (b) predicted shear stress σ_{xy} at ϕ=0.30.

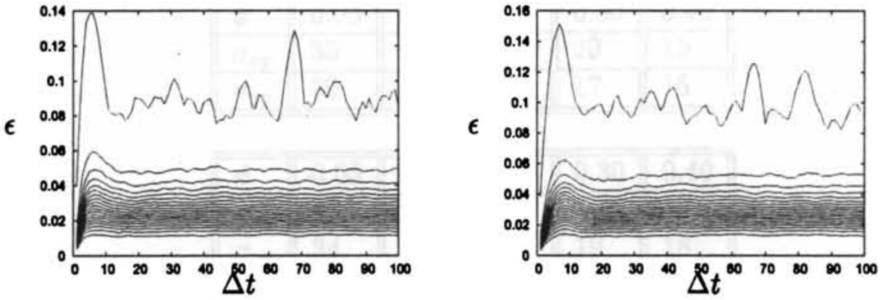

(a) (b)

Figure 5.33: Space-time separation plot of (a) actual and (b) predicted normal stress σ_{yy} at ϕ=0.30.

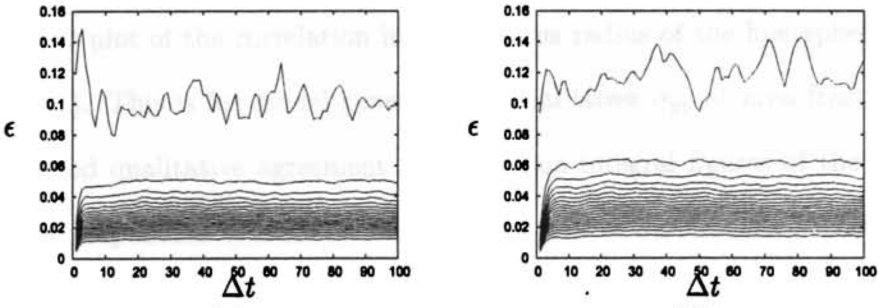

(a) (b)

Figure 5.34: Space-time separation plot of (a) actual and (b) predicted shear stress σ_{xy} at ϕ=0.40.

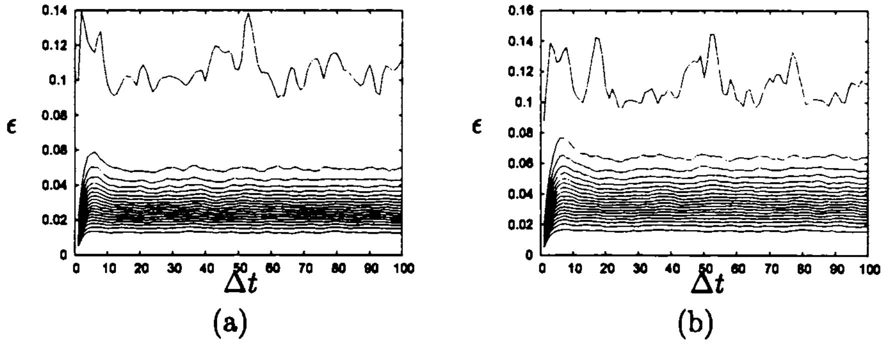

Figure 5.35: Space-time separation plot of (a) actual and (b) predicted normal stress σ_{yy} at ϕ=0.40.

integral estimate from the model generated stress components.

ϕ	0.05	0.10	0.20	0.30	0.40
σ_{xy}	35	25	23	20	15
σ_{yy}	30	17	17	17	15

(a)

ϕ	0.05	0.10	0.20	0.30	0.40
σ_{xy}	33	24	30	19	17
σ_{yy}	34	18	20	19	18

(b)

Table 5.3: Comparison of the approximate delay time at which the contour lines in the space-time separtion plots attains saturation for (a) the simulated stress components σ_{xy} and σ_{yy} using Stokesian Dynamics with that of (b) the model generated stress components for area fraction $0.05 \leq \phi \leq 0.40$ as observed from figures (5.26) to (5.35)

A typical plot of the correlation integral versus radius of the hpersphere is shown in figure(figure). This is for model generated normal stress σ_{yy} at area fraction $\phi = 0.20$. There is good qualitative agreement of correlation integral figures of the model generated stress components with the corresponding figures of the simulated stress components from Stokesian Dynamics simulation method. So we use more or less the same respective dimensions for computing the Lyapunov exponent of the model generated stress components.

Next, we consider the estimation the Lyapunov exponent from the model generated

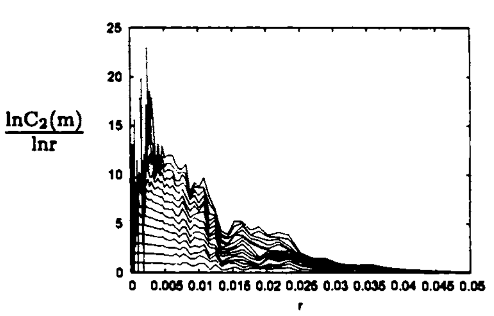

Figure 5.36: A typical figure showing an approximate correlation dimension of the predicted normal stress σ_{yy} at ϕ=0.20.

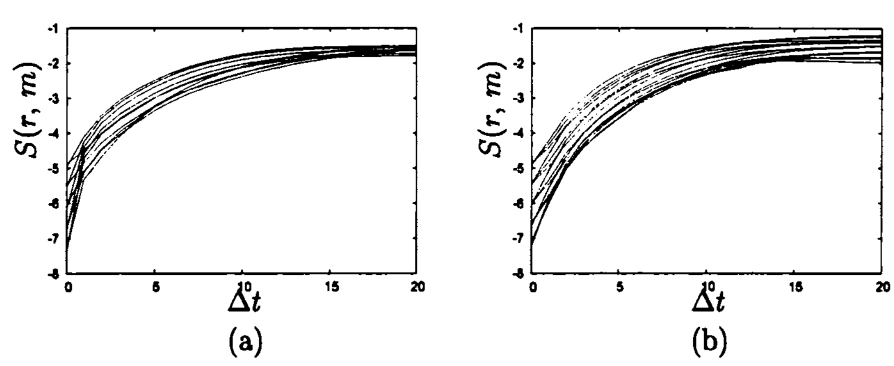

(a) (b)

Figure 5.37: Exponential divergence plot of (a) actual and (b) predicted shear stress σ_{xy} at ϕ=0.05.

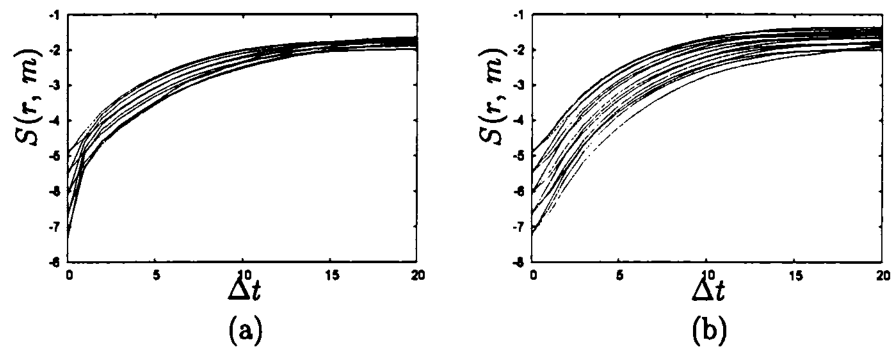

(a) (b)

Figure 5.38: Exponential divergence plot of (a) actual and (b) predicted normal stress σ_{yy} at ϕ=0.05.

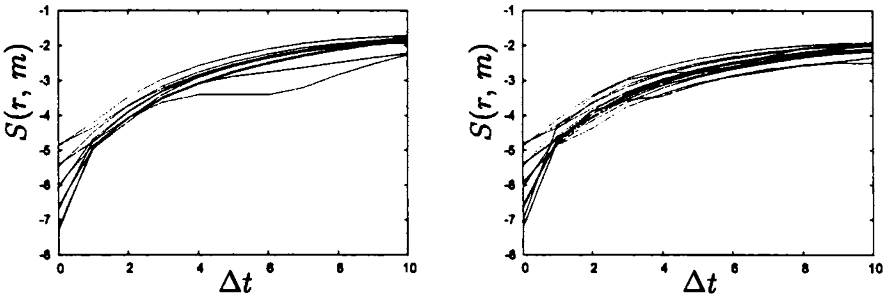

(a) (b)

Figure 5.39: Exponential divergence plot of (a) actual and (b) predicted shear stress σ_{xy} at ϕ=0.10.

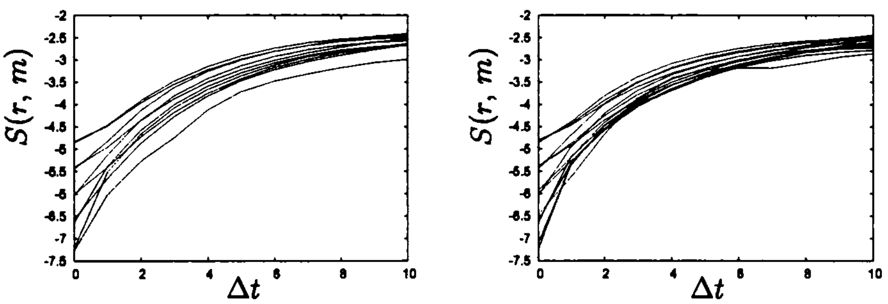

(a) (b)

Figure 5.40: Exponential divergence plot of (a) actual and (b) predicted normal stress σ_{yy} at ϕ=0.10.

stress components for area fraction of particles over the range $0.05 \leq \phi \leq 0.4$. We found good qualitative agreement in figures(5.37) to (5.46) with their corresponding figures of the simulated stress components. We can also observe good quantitative agreement in these figures.

5.5 Discussion

In chapter 4, we analysed the time series of stress fluctuations using the tools of nonlinear time series analysis and chaos theory of the sheared Stokesian suspensions simulated using Stokesian Dynamics Simulation method formulated by [Brady Bossis, 1988] [19] and modified for Couette gaps by [Singh and Prabhu, 2000] [122] , for different area fraction

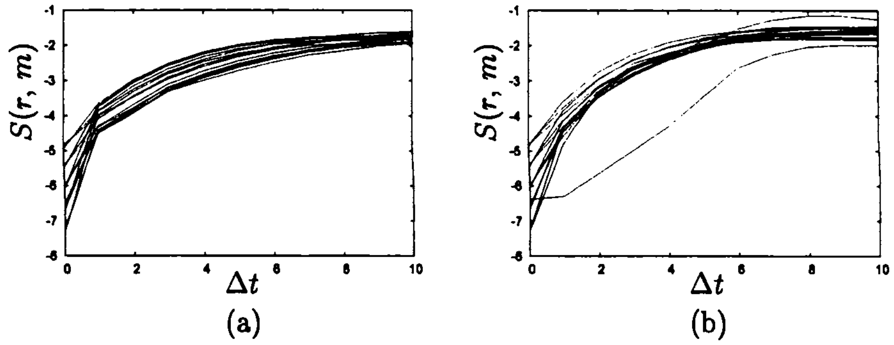

(a) (b)

Figure 5.41: Exponential divergence plot of (a) actual and (b) predicted shear stress σ_{xy} at ϕ=0.20.

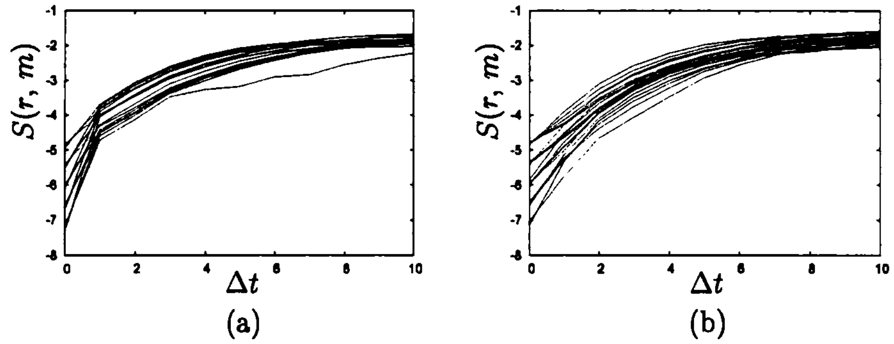

(a) (b)

Figure 5.42: Exponential divergence plot of (a) actual and (b) predicted normal stress σ_{yy} at ϕ=0.20.

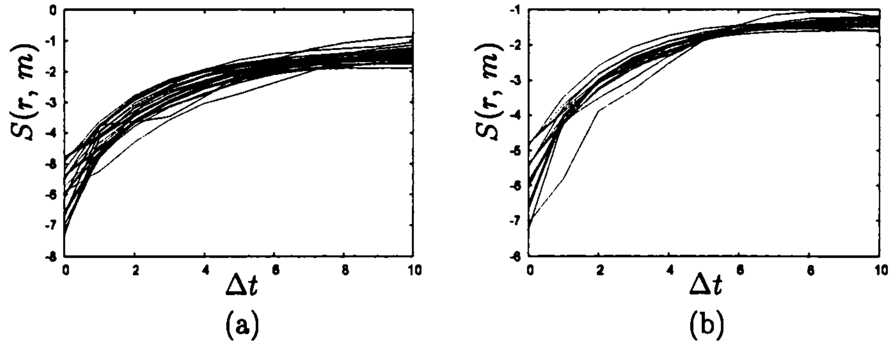

(a) (b)

Figure 5.43: Exponential divergence plot of (a) actual and (b) predicted shear stress σ_{xy} at ϕ=0.30.

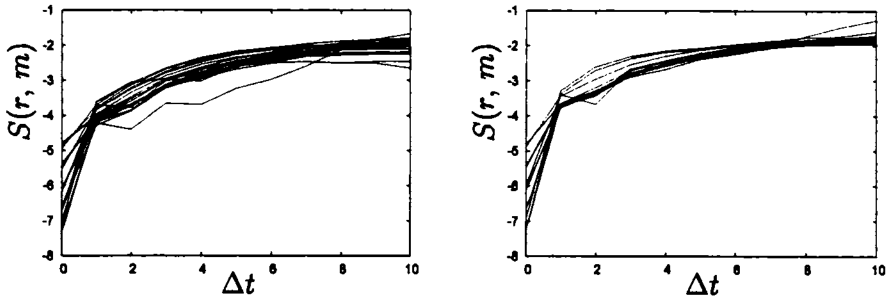

(a) (b)

Figure 5.44: Exponential divergence plot of (a) actual and (b) predicted normal stress σ_{yy} at ϕ=0.30.

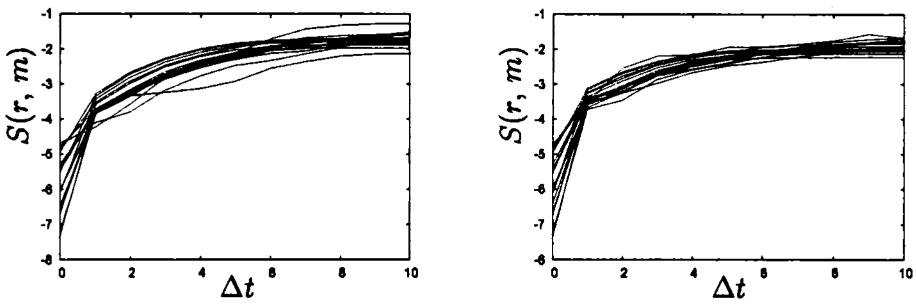

(a) (b)

Figure 5.45: Exponential divergence plot of (a) actual and (b) predicted shear stress σ_{xy} at ϕ=0.40.

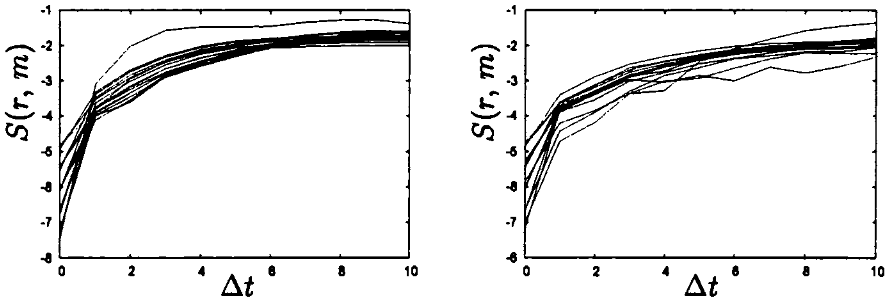

(a) (b)

Figure 5.46: Exponential divergence plot of (a) actual and (b) predicted normal stress σ_{yy} at ϕ=0.40.

of particles over the range $0.05 \leq \phi \leq 0.6$. We provided concrete numerical evidence to establish the fact that the underlying attractor governing stress fluctuations of the sheared Stokesian suspension is low-dimensional, deterministic and chaotic. The chaotic nature of the attractor indicates that accurate short-term predictions can performed. Thus, we performed prediction of future values of times series with considerable success. We, also, performed a cross-prediction of one time series from another time series using the insight obtained from the analysis. In chapter 5, we developed model equations for the stress components over the range of area fractions $0.05 \leq \phi \leq 0.4$ using an evolutionary algorithm called Darwin. The model equations of the simulated stress components at each area fraction of particles generated time series of stress components whose properties are in good agreement with the properties of the simulated stress components both qualitatively and qunatitatively. The close equivalence of both qualitative and to a great extent quantitative properties of simulated and model generated stress fluctuations show the reliability of our analysis. We observed that the number of independent variables in the model equations required to describe the stress fluctuations at each area fraction of particles were the same as the embedding dimension for the reconstruction of the chaotic attractor of simulated stress fluctuations at the respective area fraction of particles.

5.6 Future work

We observed that one stress component can be predicted using another stress component at the same area fraction. This implies a type of synchroniztion of one stress component with another stress component. This finding suggests us to further analysis of the synchronization of stress components with another stress component at the same or different area fraction of particles. The different model equations of stress components for different area fraction of particles hints at the possible existence a general formula for stress fluctuations with area fraction of particle as a parameter. To make a conclusive statement further analysis is required. Also, the existence of such a general formula for stress components will open up more directions for further analysis: for example, control of temporal stress fluctuations by proper manipulation of model parameters, expanding parameter space for bifurcations analysis and also to examine the possible existence of new phenomena or manifestation of existing phenomena.

5.7 Publications

The following publications resulted during the above work.

- * Dasan, J., Ramamohan, T. R., Singh, A. and Nott, P. R., "Stress fluctuations in sheared Stokesian suspensions," Phys. Rev. E, **66** pp.021409:1-14 (2002).
- * Anil Kumar, C. V., Dasan, J. and T. R. Ramamohan "Comparative analysis of a heuristic control of chaos algorithm in some model systems," Int. J. of Bifurcation and Chaos, **10**, 1, pp.237-249 (2000).
- * Radhakrishnan, K., Asokan, K., Dasan, J., Chandrashekara Bhat, C. and T. R. Ramamohan "Numerical evidence for the existence of a low-dimensional attractor and its implications in the rheology of dilute suspensions of periodically forced slender bodies," Phys. Rev. E, **60**(6), pp.6602-6609 (1999).
- * Asokan, K., Anil Kumar, C. V., Dasan, J., Radhakrishnan, K., Satheesh Kumar, K. and T. R. Ramamohan, "Review of chaos in the dynamics and rheology of suspensions of orientable particles in simple shear flow subject to an external periodic force," J. Non-Newtonian Fluid Mech. **129**, pp.128-142 (2005).

Bibliography

[1] Abarbanel, H. D. I., Frison, T. W., and Lev Sh. Tsimring, "Obtaining order in a world of chaos," IEEE Signal Processing Magazine, pp.49-65 (1998).

[2] Abarbanel, H. D. I., *Analysis of observed chaotic data* (Springer, 1996).

[3] Abarbanel, H. D. I., Brown, R., Sidorowich, J. and L. S. Tsimring, "The analysis of observed chaotic data in physical systems," Rev. Mod. Phys. **65**, pp.1331-1392 (1993).

[4] Acrivos, A., Drazer, G., Koplik, J. and Boris Khusid, "Velocity fluctuations in non-Brownian suspensions undergoing simple shear flow," XXI ICTAM, Warsaw, Poland, (August-2004).

[5] Albano, A. M., Muench, J., Schwartz, C., Mees, A. I. and P. E. Rapp, "Singular-value decomposition and the Grassberger-Procaccia algorithm," Phys. Rev. A **38**, pp.3017-3026 (1988).

[6] Alligood, K. T., Sauer, T. D. and James A. Yorke, *Chaos: An introduction to dynamical systems* pp.108 (Springer-Verlag, New York, 1996).

[7] Alvarez, A., Orfila, A. and J. Tintore, "DARWIN: An evolutionary program for nonlinear modeling of chaotic time series", Computer Physics Communications **136**, pp.334-349 (2001).

[8] Anil Kumar, C. V., Dasan, J. and T. R. Ramamohan, "Comparative analysis of a heuristic control of chaos algorithm in some model systems," Int. J. Bifurcation and Chaos **10**(1), pp.237-249 (2000).

[9] Ashkenazy, Y. "The use of generalized information dimension in measuring fractal dimension of time series," Physica A **271**, pp.427-447 (1999).

[10] Asokan, K., Anil Kumar, C. V., Dasan, J., Radhakrishnan, K., Satheesh Kumar, K. and T. R. Ramamohan, "Review of chaos in the dynamics and rheology of suspensions of orientable particles in simple shear flow subject to an external periodic force," J. Non-Newtonian Fluid Mech. **129**, pp.128-142 (2005).

[11] Ataei, M., Lohmann, B., Khaki-Sedigh, A. and C. Lucas, "Model based method for determining the minimum embedding dimension from chaotic time series - univariate and multivariate cases," Nonlinear Phenomena in Complex Systems **6**, pp.842-851 (2003).

[12] Bamford, C. and Curran, P., *Data strunctures, Files and Databases* (McMillan Education, London, 1991).

[13] Barahona, M. and C.-S. Poon, "Detection of nonlienar dynamics in short noisy time series," Nature **381**, pp.215-217 (1996).

[14] Batchelor, G. K., " The stress system in a suspension of force-free particles," J. Fluid Mech. **41**, pp.545-570 (1970).

[15] Batcheler, G. K. and J. T. Green, "The hydrodynamic interaction of two small freely-moving spheres in a linear flow field," J. Fluid Mech. **56**, pp.375-400 (1972).

[16] Bianchi, M. M., Arizmendi, C. M. and J. R. Sanchez "Detection of chaos: new approach to atmospheric pollen time-series analysis," Int. J. Biom. **36**(1), pp.172-175 (1992).

[17] Birkoff, G. D., *Dynamical Systems*, Colloq. Publ. IX, 2nd edn. AMS, (Providence, RI, 1960).

[18] Brady, J. F. and J. F. Morris, "Microstructure of strongly sheared suspensions and its impact on rheology and diffusion," J. Fluid Mech. **348**, pp.103-139 (1997).

[19] Brady, J. F. and G. Bossis, "Stokesian Dynamics," Ann. Rev. Fluid Mech. **20**, pp.111-157 (1988).

[20] Brady, J. F., Phillips, R. J., Lester, J. C. and G. Bossis, "Dynamic simulation of hydrodynamically interacting suspensions," J. Fluid Mech. **195**, pp.257-280 (1988).

[21] Brady, J. F. and G. Bossis, "The rheology of concentrated suspensions of spheres in simple shear flow by numerical simulation," J. Fluid Mech. **155**, pp.105-129 (1985).

[22] Brenner, H. and O'Neill, M. E., "On the Stokes resistance of multiparticle system in a linear shear field," Chem. Engg. Sci. **27**, pp.1421-1439 (1972).

[23] Broomhead, D. and G. P. King, "Extracting qualitative dynamics from experimental data," Physica D **20**, pp.217-236 (1986).

[24] Bunimovich, L. and M. Jiang, "Dynamics of spatial averages," Chaos **7**(1), pp.21-26 (1997).

[25] Carr, T. W. and I. B. Schwartz, "On measures of disorder in globally coupled oscillators," Physica D **115**, pp.321-340 (1998).

[26] Casdagli, M., "Nonlinear prediction of chaotic time series," Phys. D **35**, pp.335-356 (1989)

[27] Casdagli, M., Des Jardins, D., Eubank, S., Farmer, J. D., Gibson, J., Theiler, J., and N. Hunter, *Nonlinear modelling of chaotic time series: Theory and applications*, in J.H. Kim, J. Stringer(Eds.), pp.335-381, (Applied Chaos, John Wiley and Sons, Inc., 1992).

[28] Cellucci, C. J., Albano, A. M. and P. E. Rapp, "Comparative study of embedding methods," Phys. Rev. E **67**, pp.066210:1-13 (2003).

[29] Christini, D. J., Collins, J. J., and P. S. Linsay , "Experimental control of high-dimensional chaos: the driven double pendulum," Phys. Rev. E **54**(5), pp.4824-4827 (1996).

[30] Ciofini, M., Meuci, R. and F. T. Arecchi "Experimental control of chaos in a laser," Phys. Rev. E **52**(1), pp.94-97 (1995).

[31] Correa, M. V., Aguirre, L. A. and E. M. A. M. Mendes, "Modeling chaotic dynamics with discrete nonlinear rational models," Int. J. Bifurcation and Chaos **10**(5), pp.1019-1032 (2000).

[32] Dasan, J., Ramamohan, T. R., Singh, A. and P. R. Nott, "Stress fluctuations in sheared Stokesian suspensions," Physical Rev. E **66** pp.021409:1-14 (2002).

[33] Ding, M., Grebogi, C., Ott, E., Sauer, T. and J. A. York, "Estimating correlation dimension from a chaotic time series: when does a plateau onset occur?," Physica D **69**, pp.404-424 (1993).

[34] Dratler, D., I. and W. R. Schowalter, "Dynamic simulation of suspensions of non-Brownian hard spheres," J. Fluid Mech. **325**, pp.53-77 (1996).

[35] Drazer. G, Koplik, J., Khusid, B. and A. Acrivos, "Deterministic and stochastic behavior of non-Brownian spheres in sheared suspensions," J. Fluid Mech. **460** pp.307-335 (2002).

[36] Drazer. G, Koplik, J., Khusid, B. and A. Acrivos, "Microstructure and velocity fluctuations in sheared suspensions," J. Fluid Mech. **511**, pp.237-263 (2004).

[37] Durlofsky, L., Brady, J. F. and G. Bossis, "Dynamic simulation of hydrodynamically interacting particles," J. Fluid Mech. **180**, pp.21-49 (1987).

[38] Durlofsky, L. and Brady, J. F., "Dynamics simulation of bounded suspensions of hydrodynamically interacting particles," J. Fluid Mech. **200**, pp.39-67 (1989).

[39] Eiben, A. E., Smith, J. E. and J. D. Smith, *Introduction to Evolutionary Computing* (Springer-Verlag, 2003).

[40] Einstein, A. "Eine neue Bestimmung der Molekuldimension," Annalen Phys. **19**, pp.298-306 (1906).

[41] Eckmann, J. P., Oliffson Kamphorst, S., Ruelle, D. and S. Ciliberto "Lyapunov exponents from a time series," Phys. Rev. A **34**, pp.4971-4976 (1986).

[42] Eckmann, J. P. and D. Ruelle, "Ergodic theory of chaos and strange attractors," Rev. Mod. Phys. **57**, pp.617-656 (1985).

[43] Eykholt, R. and Umberger, D. ,"Characterization of fat fractals in nonlinear dynamical systems," Phys. Rev. Letts. **57**, pp.2333-2336 (1986).

[44] Ewald, P. P., "Die Berechnung optischer und elektrostatischer Gitterpotentiate," Ann. Phys. **64**, pp.253-287 (1921).

[45] Farmer, J., "Chaotic attractors of an infinite dimensional dynamical system," Physica 4D, pp.366-393(1982).

[46] Freistetter, F. "Fractal dimensions as chaos indicators," Celestial Mechanics and Dynamical Astronomy **78**, pp.211-225 (2000).

[47] Ganatos, P., Weinhaus, S. and Pfeffer, R., "A strong interaction theory for the creeping motion of a sphere between plane parallel boundaries. Part 2. Paralle motion," J. Fluid Mech. **99**, pp.739-753 (1980).

[48] Gadala-Maria, F. A., *The rheology of concentrated suspension.*, Ph. D. Thesis (Standford University, 1979)

[49] Galka, A. and G. Pfiser, "Dynamical correlations on reconstructed invariant densities and their effect on correlation dimension estimation," Int. J. Bifurcation and Chaos **23**, pp.723-732 (2003).

[50] Gaspard, P., Briggs, M. E., Francis, M. K., Sengers, J. V., Gammon, R. W., Dorfman, J. R. and R. V. Calabrese, "Experimental evidence for microscopic chaos," Nature **394**, pp.865-868 (1998).

[51] Gosztonyi, A., *Der Raum*, pp.1088 (Verlag Karl Alber Freiburg, 1976)

[52] Gouesbet, G. "Reconstruction of the vector fields of continuous dynamical systems from numerical scalar time sereis," Phys. Rev. A **43**(10), pp.5321-5331 (1991).

[53] Gouesbet, G., "Reconstruction of standard and inverse vector fields equivalent to a Rossler system," Phys. Rev. A **44**(10), pp.6264-6280 (1991).

[54] Graf, K. E. and T. Elbert, "Dimensional analysis of the waking EEG," Biol. Psychol. **31** pp.173-191 (1990)

[55] Grassberger, P., Schreiber, T. and C. Schaffrath, "Nonlinear time sequence analysis," Int. J. Bifurcation and Chaos **1**, pp.521- 547(1991).

[56] Grassberger, P. "Generalized dimensions of strange attractors," Phys. Lett. A **97**, pp.227-230 (1983).

[57] Grassberger, P. and I. Procaccia, "Measuring the strangeness of strange attractors," Physica D **9** pp.189-208 (1983).

[58] Happel, J. and Brenner, H., *Low Reynolds number Hydrodynamics,* 4th ed., (Nijhoff, Dordresht, 1986).

[59] Hartman, P., *Ordinary Differential Equations* (John Wiley & Sons, New York, 1964)

[60] Hegger, R., Kantz, H. and T. Schreiber, "Practical implimentaion of nonlinear time series methods: The TISEAN package," Chaos **9**(2), pp.413-435 (1999).

[61] Heitor, F., Pereira-Pinto, I., Ferreira, A. M. and M. A. Savi, "Chaos control in a nonlinear pendulum using a semicontinous method," Chaos, Solitons and Fractals **22**, pp.653-668 (2004).

[62] Hentschel, H. and Procaccia, I., "The infinite number of generalized dimensions of fractals and strange attractors," Physica 8D, pp.435-444 (1983).

[63] Holzfuss, J. and G. Mayer-Kress, "An approach to error dimension algorithms," in G. Mayer-Kress ed., *Dimensions and Entropies in chaotic system. Quantification of complex behavior*, Springer series in Synergetic **32**, pp.114-122 (1986).

[64] Ikeguchi, T. and K. Ahara, "Time series production: Forcasting the future and understanding the past," Phys. Rev. E **55**, pp.2530-2345 (1997).

[65] Janneke Kromkamp, Dirk van der Ende, Drona Kandhai, Ruud van der Sman and Remko Boom, "Lattice Boltzman simulation of 2D and 3D non-Brownian suspensions in Couette flow," Chem. Eng. Sci. **61**, pp.858-873 (2006).

[66] Jánosi, I. M., Tamá Tél, Dietrich E. Wolf and Jason A. C. Gallas, "Chaotic particle dynamics in viscous flow: the three-particle Stokeslet problem," Phys. Rev. E **56** 3, pp.2858-2868 (1997).

[67] Jenkins, J. T. and Mctigue, D. F., "Transport processes in concentrated suspensions: the role of partilce fluatuations," in *Two phase flow and Waves*, D. D. Joseph and D. G. Schaeffer edt. (Springer, 1990).

[68] Judd, K., "Building optimal models of time series," In G. Gousebet, S. Meunier-Guttin-Cluzel, and O. Menard edt., *Chaos and its reconstruction*, chap. 2, pp.179-214 (Nova Science Publishers, New York, 2003).

[69] Kantz, H. and T. Schreiber, *Nonlinear time series analysis* (Cambridge University Press, 1997).

[70] Kantz, H., "A robust method to estimate the maximal Lypaunov exponent of a time series," Phys. Lett. A **185**, pp.77-87 (1994).

[71] Kaplan, J. and J. Yorke, "Chaotic behavior of multidimensional difference equations," in Peitgen, H. O. and H. O. Walter, edt., *Functional differential equations and approximation of fixed points*, (Springer, Heidelberg, New York, 1987).

[72] Kennel, M. B., Brown, R. and H. D. I. Abarbanel, "Determining minimum embedding dimension using a geometrical cosntruction," Phys. Rev. A **45**, pp.3403-3411 (1992).

[73] Kim, S. and Karrila, S. J., *Microhydrodynamics: Principles and selected applications* (Butterworth Heinemann, Boston , 1991).

[74] Kiss, I. Z., Gáspár, V., Nyikos, L. and P. Parmananda "Controlling electrochemical chaos in the copper-phosphoric acid system," J. Phys. Chem. A **101**(46), pp.8662-8674 (1997).

[75] Kononov, E., "Visual Recurrence Analysis," Version 4.0, 1999 (email: eugenek@ ix.netcom.com).

[76] Koza, J.R., *Genetic Programming* (MIT Press, Cambridge, 1992)

[77] Kugiumtzis, D., "On the reliability of the surrogate data test for nonlineariry in the analysis of noisy time series," Int. J. Bifurcation and Chaos **11**(7), pp.1881-1896 (2001).

[78] Landau, L. D. and E. Lifschitz, *Fluid Mechanics* (Pergamon, New York, 1959).

[79] Letellier, C., Le Sceller, L., Maréchal, M., Dutertre, P., Maheu, B. and G. Gouesbet, "Global vector field reconstruction from a chaotic experimental signal in copper electrodissolution," Phys. Rev. E **51**(5), pp.4262-4266 (1995).

[80] Letellier, C., Le Sceller, L., Gousebet, G., Lusseyran, F., Kemoun, A. and B. Izrar, "Rcovering deterministic behaviour from experimental time series in mixing reactor," AIChE Journal, **43**(9), pp.2194-2202 (1997).

[81] Letellier, C., Maquet, J., Labro, H., Le Sceller, L., Gouesbet, G., Argoul, F. and A. Arnéodo "Analysing chaotic behaviour in a Belousov-Zhabotinskyi reaction by using a global vector field reconstruction," J. Phys. Chem. A. **102**, pp.10265-10273 (1998).

[82] Lorenz, E. N., "Deterministic nonperiodic flow," J. Atmos. Sci. **20**, pp.130-141 (1963).

[83] Lyapunov, A. M., "Probléme général de la stabilité du mouvement," Ann. Math. Study **17** (1947).

[84] Mahmoud, G. M. and A. A. M. Farghaly "Chaos control of chaotic limit cycles of real and complex van der Pol oscillators," Chaos, Solitons and Fractals **21**, pp.915-924 (2004).

[85] Mandelbrot, B. B., "Les objets fractals: forme, hasard et dimension," (Flammarion, Paris, 1975).

[86] Mandelbrot, B., *The fractal geometry of nature* (Freeman, New York, 1977).

[87] May, R. M., "Simple mathematical models with very complicated dyanamics," Nature **261**, pp.959-969 (1976).

[88] Meucci, R., Cinotti, D., Allaria, E., Billings, L., Triandaf, I., Morgan, D. and I. B. Schwartz, "Global manifold control in a driven laser sustaining chaos and regular dynamics," Physica D **189**, pp.70-80 (2004).

[89] Morris, J. F. and Boulay, F., "Curvilinear flows of non-colloidal suspensions: the role of normal stresse," J. Rheol. **43**(5), pp.1213- (1999).

[90] Morris, J. F. and Brady, J. F, "Self-diffusion in sheared suspensions," J. Fluid Mech. **312**, pp.223-252 (1996).

[91] Moukam Kakmeni, F. M., Bowong, S., Tchawoua, C. and E. Kaptouom "Chaos control and synchronization of a Φ^6 - Van der Pol oscillator," Physics Lett. A **322** pp.305-323 (2004).

[92] Nakamura, T., Judd, K. and A. Mees, "Refinements to model selection for nonlinear time series," Int. J. Bifurcation and Chaos **13**(5), pp.1263-1274 (2003).

[93] Nakamura, T., Judd, K. and A. Mees, "A comparative study of model selection methods for nonlinear time series," Int. J. Bifurcation and Chaos **14**(3), pp.1129-1146 (2004).

[94] Nott, P. R. and Brady, J. F., "Pressure-driven flow of suspensions: simulation and theory," J. Fluid Mech. **275**, pp.157-199 (1994).

[95] Ott, E., Sauer, T. and James A. Yorke, *Coping with Chaos* (Wiley Series, 1994).

[96] Ott, E., *Chaos in Dynamical Systems* (Cambridge University Press, 1993).

[97] Ottino, J. M., *The kinematics of mixing: stretching, chaos, and transport* (Cambridge University Press, 1989).

[98] Pavlos, G. P., Athanasiu, M. A., Diamantidis, D., Rigas A. G. and E. T. Sarris, "Nonlinear analysis of magnetospheric data Part I. Geometric characteristics of the AE index time series and comparison with nonlinear surrogate data," Nonlinear Processes in Geophysics **6**, pp.51-65 (1999a).

[99] Pavlos, G. P., Athanasiu, M. A., Diamantidis, D., Rigas, A. G. and E. T. Sarris, "Nonlinear analysis of magnetospheric data Part II. Dynamical characteristics of the AE index time series and comparison with nonlinear surrogate data," Nonlinear Processes in Geophysics **6**, pp.79-98 (1999b).

[100] Pavlos, G. P., Athanasiu, M. A., Diamantidis, D., Rigas A. G. and E. T. Sarris, "Comments and new results about the magnetospheric chaos hypothesis," Nonlinear Processes in Geophysics **6**, pp.99-127 (1999c).

[101] Pawelzik, K. and H. G. Schuster,"Generalized dimensions and entropies," Phys. Rev. A 35, pp.481-484 (1987a).

[102] Pawelzik, K. and H. G. Schuster,"Erratum: Generalized dimensions and entropies," Phys. Rev. A 36, pp.4529-4531 (1987b).

[103] Peacock, J. A, "Two-dimensional goodness-of-fit testing in astronomy," Monthly Not. of the R. Astron. Soc., **202**, pp.615-627 (1983).

[104] Phung, T. N., Brady, J. F. and G. Bossis, "Stokesian dynamics simulation of Brownian suspensions", J. Fluid Mech. **313**, pp.181-207 (1996).

[105] Poincaré, H., *Les methodes nouvelles de la mechanique celeste* (Gauthier-Villars, Paris, 1899).

[106] Poincaré, H., "Sus les équations de la dynamique et probléme de trois corps," Acta Math. **13**, pp.1-270 (1890).

[107] Poincaré, H., *Mémoire sur les courbes définies par les équations différentielles I-VI* (Oeuvre I. Gauthier-Villars, Paris, 1880).

[108] Prich, D. and J. Theiler, "Generating surrogate data for time series with several simultaneously measured variables," Phys. Rev. Letts. **73** pp. 951-954 (1994).

[109] Provenzale, A., Smith, L. A., Vio, R. and G. Murante, "Distinguishing between low-dimensional dynamics and randomness in measured time series," Physica D **58**, pp.31-49 (1992).

[110] Radhakrishnan, K., Asokan, K., Dasan, J., Chandrashekara Bhat, C. and T. R. Ramamohan, "Numerical evidence for the existence of a low-dimensional attractor and its implications in the rheology of dilute suspensions of periodically forced slender bodies," Phys. Rev. E, **60**(6), pp.6602-6609 (1999).

[111] Ricardo Femat and José Alvarez-Ramírez, "Synchronization of a class of striclty different chaotic oscillators," Phys. Lett. A **236**, pp307-313 (1997)

[112] Rosenstein, M. T., Collins, J. J. and C. J. De Luca, "A practical method for calculating largest Lyapunov exponents from small data sets," Physica D, **65**, pp.117-134 (1993).

[113] Roy, M. and R. E. Amritkar, "Effect of noise on coupled chaotic systems," Pramana **48**(1), pp.271-285 (1997).

[114] Rubin, D. M.,"Use of forcasting signatures to help distinguish periodicity, randomness and chaos in ripples and other spatial pattersn," Chaos **2**, pp.525-529 (1992).

[115] Ruelle, D. and Takens, F., "On nature of turbulence," Commun. Math. Phys. **20**, pp.167-192 (1971).

[116] Sano, M. and Y. Sawada, "Measurement of the Lyapunov spectrum from a chaotic time series," Phys. Rev. Letts., **55**, pp.1082-1085 (1985).

[117] Sauer, T. and J. Yorke, "Are the dimensions of a set and its image equal under typical smooth functions?," Ergodic Th. Dyn. Syst. **17**, pp.941-956 (1997).

[118] Sauer, T. and J. Yorke, "How many delay coordinates do you need?," Int. J. Bifurcation of Chaos **3**, pp.737-744 (1993).

[119] Schreiber, T., "Interdisciplinary application of nonlinear time series methods," Phys. Rep. 308, pp.1-64 (1999).

[120] Schuster, H., *Determininstic Chaos*, 2nd ed. (Physik-Verlag, Weinheim, Germany, 1988).

[121] Shunguang Wu and Kaifen He Zuqia Huang "Controlling spatio-temporal chaos via small external forces," Phys. Letts. A, **260** pp.345-351 (1999).

[122] Singh, A. and P. R. Nott, "Normal stresses and microstructure in bounded shear of suspensions via Stokesian dynamics simulations," J. Fluid Mech. **412**, pp.279-3021 (2000).

[123] Singh, A., *Rheology of non-colloidal suspensions* Ph. D. Thesis (Dept. of Chemical Engineering, Indian Institute of Science, Banglaore, 2000)

[124] Singh, A. and P. R. Nott, "Experimental measurements of the normal stresses in sheared Stokesian suspensions" J. Fluid Mech. **490**, pp.293-320 (2003).

[125] Sinha, S., "Noisy uncoupled chaotic map ensembles violate the law of large numbrs," Phys. Rev. Lett. **69**(23), pp.3306-3309 (1992).

[126] Sivaprakasam, S. and K. A. Shore, "Demonstration of optical synchronization of chaotic external-cavity laser diodes," Optics Lett. **24**(7), pp.466-468 (1999).

[127] Smale, S., "Differential Dynamical Systems," Bull. Am. Math. Soci. **73**, pp.747-817 (1967).

[128] Strybulevych, A. L., Leary, D. M. and J. H. Page, "Shear-induced structure and velocity fluctuations in particulate suspensions probed by untrasonic correlation spectroscopy and rheology," edited by M. Tokuyama and I. Oppenhiem in *Slow dynamics in complex systems: 3rd International Symposium*, pp.444-445 (American Institutue of Physics, 2004).

[129] Small, M., *Applied Nonlinear Time Series Analysis: applications in Physics, Physiology and Finance*(World Scientific Publishing, Singapore, 2005).

[130] Sugihara, G. and R. M. May, "Nonlinear forcasting as a way of distinguishing chaos from measurement error in time series," Nature **344**, pp.734-741 (1990).

[131] Szpiro, G.G., "Forcasting chaotic time series with genetic algorithms", Phys. Rev. E **55**, pp.2557-2568 (1997)

[132] Takens, F. "Detecting strange attractor in turbulence," in Vol. 898 of Lectures Notes in Mathematics, edited by D. A. Rand and L. S. Young, pp.366-381. (Spinger Verlag, Berlin, 1981).

[133] Theiler, J., "Estimating fractal dimension," J. Opt. Soc. Amer. A **7**, pp.1055-1073 (1990).

[134] Theiler, J. "On the evidence for low-dimensional chaos in an epileptic electroencephalogram," Physics Lett. **196** pp.335-341 (1995).

[135] Tsonis, A., *Chaos: From Theory to Application* (Plenum, New York, 1992).

[136] Veronig, A., Messerotti, M. and A. Hanslmeier, "Determination of fractal dimensions of solar radio bursts," Astronomy and Astrophysics **357**, pp.337-350 (2000).

[137] Viktor Muller, Werner Lutzenberger Friedemann Pulvermuller and Bettina Mohr Niels Birbaummer, "Investiagtion of brain dynamics in Parkinson's disease by methods derived from nonlinear dynamics," Exp. Brain Res. **137**, pp.103-110 (2001).

[138] Wolf, A., Swift, J. B., Swinney, H. L. and J. A. Vastano, "Determining Lyapunov exponent from a time series," Physica D **16**, pp.285-317 (1985)

[139] Xiaofeng, G. and C. H. Lai, "Improvement of the local prediction of chaotic time series," Phys. Rev. E **60**(5), pp.5463-5463 (1999).

[140] Zarraga, I. E., Hill, D. A. and D. T. Leighton, "The characterization of the total stress of concentrated suspesnions of noncolloidal spheres in Newtonain fluids," J. Rheol. **44**(2), pp.185-220 (2000).

[141] Zeitler, H., Neidhardt, W, *Graktale und Chaos* (Wissenschaftliche Buchgesellschaft, 1993).

[142] Zumbrunnen, D. A., Miles, K. C. and Y. H. Liu, "Auto-processing of very fine-scale composite materials by chaotic mixing of melts," Composites Part A **27A** (1), pp.37-47 (1996).